



**HAL**  
open science

# Numerical and Experimental Studies of Pristine and Cluster containing Silane-Hydrogen Capacitively Coupled Plasmas Used for Silicon Epitaxial Growth

Tinghui Zhang

► **To cite this version:**

Tinghui Zhang. Numerical and Experimental Studies of Pristine and Cluster containing Silane-Hydrogen Capacitively Coupled Plasmas Used for Silicon Epitaxial Growth. Physics [physics]. Institut Polytechnique de Paris, 2021. English. NNT : 2021IPPAX079 . tel-03500344

**HAL Id: tel-03500344**

**<https://theses.hal.science/tel-03500344>**

Submitted on 22 Dec 2021

**HAL** is a multi-disciplinary open access archive for the deposit and dissemination of scientific research documents, whether they are published or not. The documents may come from teaching and research institutions in France or abroad, or from public or private research centers.

L'archive ouverte pluridisciplinaire **HAL**, est destinée au dépôt et à la diffusion de documents scientifiques de niveau recherche, publiés ou non, émanant des établissements d'enseignement et de recherche français ou étrangers, des laboratoires publics ou privés.

# Numerical and Experimental Studies of Pristine and Cluster containing Silane-Hydrogen Capacitively Coupled Plasmas Used for Silicon Epitaxial Growth

Thèse de doctorat de l'Institut Polytechnique de Paris  
préparée à l'École polytechnique

École doctorale n°626 École Doctorale de l'Institut Polytechnique de  
Paris (ED IP Paris)

Spécialité de doctorat: Physique

Thèse présentée et soutenue à Palaiseau, le 13 Octobre 2021, par

**Tinghui Zhang**

Composition du Jury :

Laurent Thomas Professor, PROMES (– Université de Perpignan)	Président
Olivier Leroy Chargé de recherche, LPGP (– Université Paris-Saclay)	Rapporteur
Steven Girshick Professor, Department of Mechanical Engineering (– University of Minnesota)	Rapporteur
Armelle Michau Ingénieure de recherche, LSPM (– Université Paris 13)	Examinatrice
Tatiana Novikova Ingénieure de recherche, LPICM (– École polytechnique)	Directrice de thèse
Pere Roca i Cabarrocas Directeur de recherche, LPICM (– École polytechnique)	Co-Directeur de thèse
Vincent Giovangigli Directeur de recherche, CMAP (– École polytechnique)	Invité
Jean-Maxime Orlac'h Ingénieur de recherche, Département aérodynamique (– ONERA)	Invité



*à mes chers parents*

献给我亲爱的父亲母亲

# Acknowledgments

Time is a great storyteller. These three years would definitely be a precious period in my life, but writing the acknowledgments implies the end of the story. Taking this opportunity, I would like to thank all those who have been along with me for this period.

First and foremost, I would like to thank my supervisors, Tatiana Novikova and Pere Roca i Cabarrocas. I want to express my sincere appreciation to Tatiana Novikova, my supervisor, for proposing this PhD research subject to me, and also thanks for her continuous encourage and support during this three years' work. I am grateful to Tatiana Novikova for organizing Ph.D. monthly meetings to follow my research progress, to give me lots of chance to discuss with other professionals and present myself. Thank her for teaching me about plasma and numerical algorithms with great patience. I also thank her husband Pavel Bulkin for treating me with delicious food and all kinds of wine on every Christmas Eve, which make me feel warm in a foreign country.

I also would like to thank Pere Roca i Cabarrocas, my co-supervisor, for his always availability throughout my thesis, regardless of his many responsibilities as a former director of the LPICM and scientific director of IPVF now. He was able to transmit me part of his immense scientific knowledge and experimental skills, which is the sum of the knowledge accumulated at the LPICM during its young history. I also greatly appreciate his teaching about the ARCAM reactor and ellipsometry. His passion during scientific discussion and the never-failing enthusiasm inspires me a lot.

In addition, I am grateful to my supervisors for providing me the opportunity to participate in variety of international conferences. It was extremely valuable experience that let me learn the latest cutting-edge research results in plasma physics and plasma modelling and to communicate with the best researchers around the world.

Then, I would like to express my sincere gratitude to Vincent Giovangigli, my mentor, for giving me lots of advices and ideas about plasma modelling from both physical and algorithmic perspectives. Vincent has always shown to me very high standards in his work and extreme intellectual rigor. His great ease in the theoretical

and numerical analysis of mathematical models goes hand in hand with a very rich imagination and a deep knowledge of the underlying physics.

I would specially thank Jean-Maxime Orlac'h, my mentor, for teaching me to understand and improve the plasma model for one and half of year during my Ph.D. It was an unforgettable memory when we had many great discussions, sometimes we discussed it so late that we forgot to have a dinner. He set a good example with his patience, rigor, and seriousness towards scientific research, that drive me to complete my research with passion and confidence. I would also like to thank my colleague, Monalisa Ghosh, for her teaching and accompanying me with experimental work. Her kindness and cheerfulness always make working vibe very active.

I spent these three years at LPICM, Ecole Polytechnique, and I owe a lot to this research team. Yvan Bonnassieux, the head of the lab, is always trying his best and then successfully make the LPICM a nice place to work. During the special period of COVID-19, he leads the whole team to keep our lab a safe, heartwarming place as usual. I would like to acknowledge the work of Laurence Corbel, Fabienne Pandolf, Gabriele Medina for their cheerfulness and their efficiency in solving all administrative problems. I thank the entire team of the BEER for helping fixing and improving the ARCAM reactor of the lab and helping us to print posters for the conferences. Also, I thank Frederic Liege for teaching me Linux and cluster calculation and thank Eric Paillassa for the IT support. I thank my colleagues, Ghewa Akiki, Hee-Ryung Lee, Anatole Desthieux, Khaoula Jemli, Hae-Yeon Jun, Hindia Nasiri, Eric Ngo, Junha Park, Junkang Wang, Letian Dai for helping me and making my life colorful. I thank all these people for contributing to LPICM that is indeed a great place to work!

I would like to thank my dear friend Shiwei Ren for his companionship during these three years. I thank him for all valuable time we spent together. In the face of friendship, people, like stars, do not hinder each other, but shine on each other. Also, I thank my friend Qiqiao Lin for sharing his opinions about life and work, treating us with delicious food and accompanying me to look for a new landscape in Palaiseau, thanks to Guili Zhao, for delicious food, taking me to vacation and bringing me to new

friends. I thank Can Wang for our precious friendship. In addition, I express my appreciation to my roommates in my 1<sup>st</sup> year of Ph.D., Kun Wang and Zhuzhi Fan for sharing their visions and watching football games with me, Mufei Luo and Zhizhong Zhang for all outdoor activities. Also, I would like to thank Chuang Yu for teaching me to fish and saved me from falling into the water. Last, thanks to Qi Fan, my girlfriend, for the precious moments we have been through together. I love you from the day we met until the end of my days. Thanks to all other people who once helped me, if I forget to mention you here, please don't mind. Thank you for being involved in my life and helping me stay away from loneliness.

I thank my family and my friends in China who supported and helped me solving the loneliness and problems in life I have had in France alone. Thanks to my family members for always backing on me with endless help and love, which are gentle and powerful.

I thank the funding of the China Scholarship Council (CSC) to grant my three years PhD in France. I will treasure this experience and memory forever.

Peace & Love.

Thank you all

Merci à tous

Tinghui

# Résumé

Sur la base d'un modèle fluide développé dans notre groupe, un modèle fluide 1D de plasmas silane/hydrogène dans des décharges RF à couplage capacitif comprenant une chimie détaillée du plasma ainsi que des réactions de surface pour tenir compte des processus de dépôt et de gravure a été développé et testé par rapport aux résultats expérimentaux. Ce modèle comprend les propriétés électriques, la vitesse de convection, le mécanisme chimique dans la décharge, le dépôt et l'analyse de la vitesse de gravure. L'équation de Poisson est utilisée pour le potentiel électrique et l'équation pour la température électronique est incorporée. Les expressions des flux de transport ont été simplifiées en utilisant l'approximation de Hirschfelder-Curtiss. Un mécanisme chimique complet comprend : i) des réactions de collision électronique qui dépendent de la température électronique ; ii) les réactions des espèces lourdes qui dépendent de la température des espèces lourdes ; iii) mécanismes de chimie de surface. En particulier, la chimie de surface, y compris les réactions de recombinaison, de gravure et de dépôt, est couplée au modèle de fluide via un ensemble de probabilités de réaction.

Dans des conditions de procédé typiques, le modèle de fluide 1-D est réalisé pour étudier les propriétés du plasma silane-hydrogène. Après environ 40 000 cycles RF, une solution à l'état stable est obtenue. Pour les propriétés électriques, le potentiel électrique est plus grand au centre de la décharge (plasma bulk) qu'au voisinage des électrodes (gainés de plasma). De plus, le potentiel électrique est presque constant dans la masse, tandis qu'une chute de potentiel se produit dans les gainés. Le champ électrique n'apparaît que dans les gainés de plasma, et il est presque nul dans la masse du plasma. La température des électrons dans les régions des gainés augmente lorsque les gainés se dilatent, alors qu'elle reste autour de 5 eV dans la masse du plasma. Les électrons sont principalement contraints dans la masse du plasma et les électrons secondaires sont émis avec une énergie élevée lorsque la gaine se dilate en raison du champ électrique.

Les ions positifs les plus dominants sont  $H_3^+$ , qui sont principalement produits

par la réaction " $\text{H}_2 + \text{H}_2^+ \rightarrow \text{H}_3^+ + \text{H}$ ".  $\text{SiH}_3^-$  et  $\text{SiH}_2^-$  sont les ions négatifs dominants. Ils sont principalement produits à partir de réactions d'attachement dissociatives. Pour les espèces neutres, les radicaux  $\text{SiH}_3$  sont les espèces contenant du Si les plus abondantes, c'est le principal précurseur du dépôt de couches minces de silicium.

Enfin, la vitesse de convection est modélisée. Le mélange gazeux est introduit du côté de l'électrode alimentée par RF avec une vitesse fixe. La vitesse normale diminue le long de l'axe Z dans le réacteur, et la vitesse tangentielle atteint son maximum dans la majeure partie de la décharge.

Des études numériques et expérimentales sur les effets de la pression du gaz (1 à 3,5 Torr) et de la concentration de silane (2 à 10 %) sur la vitesse de dépôt de films minces de silicium ont démontré que la vitesse de dépôt déterminé à partir de la modélisation des mesures de la fonction diélectrique par ellipsométrie dans le domaine UV-visible concorde bien avec les résultats de la modélisation. Le taux de dépôt total calculé augmente linéairement avec la concentration de silane et les radicaux  $\text{SiH}_3$  sont les principaux précurseurs du dépôt de couche mince dans la plage de pression de 1 à 3,5 Torr et pour des concentrations de silane de 2 à 10 %. La vitesse de dépôt net montre un bon accord avec les valeurs expérimentales après prise en compte de la vitesse de gravure. De plus, la modélisation montre que les ions  $\text{H}_3^+$  sont les principales espèces contribuant au processus de gravure et que leur effet diminue avec l'augmentation de la concentration en silane. Des résultats similaires ont été obtenus pour l'étude de l'effet de la pression du gaz sur la vitesse de dépôt, à savoir que la vitesse de dépôt est dominée par la contribution des radicaux  $\text{SiH}_3$ , tandis que les ions  $\text{H}_3^+$  sont responsables de la vitesse de gravure. A 2,5 Torr, la vitesse de gravure par  $\text{H}_3^+$  s'élève à 1 /s, soit environ 40 % du dépôt induit par les radicaux (2,6 Å/s), ce qui donne une vitesse de dépôt nette de 1,6 Å/s. Après avoir inclus la vitesse de gravure dans les calculs de la vitesse de dépôt net, les valeurs de cette dernière se rapprochent des valeurs expérimentales. En bref, les radicaux  $\text{SiH}_3$  s'avèrent être le principal contributeur aux taux de dépôt calculés, tandis que les ions  $\text{H}_3^+$  jouent le rôle principal dans le processus de gravure.

Le modèle fluide 1-D a également été couplé à un modèle sectionnel et à des

équations de transport pour tenir compte de la formation de nanoparticules dans le plasma et de l'évolution des distributions de taille et de charge des nanoparticules. Le modèle contient un mécanisme chimique complet de nucléation des nanoparticules, l'effet de l'augmentation de charge sur la coagulation et le transport des nanoparticules. De plus, l'effet des nanoparticules sur les densités d'espèces plasmatiques, le potentiel électrique et la température électronique est pris en compte. Le modèle a été utilisé pour étudier les premières étapes de la formation de nanoparticules dans des conditions typiques pour le dépôt de couches minces de silicium, où le rayon des particules reste inférieur à 10 nm. Pour rendre le modèle fluide-sectionnel couplé 1-D efficace du point de vue informatique (réduire le temps de calcul), une méthode de fractionnement du temps a été utilisée. Deux groupes de variables (rapides et lentes) ont été définis en fonction de l'échelle de temps caractéristique de leur dynamique par rapport à la période des oscillations du champ RF (74 ns). Les équations régissant les deux groupes ont été résolues de façon itérative en gardant les variables d'un autre groupe comme « figées » et en utilisant un pas de temps plus petit pour le groupe de variables rapides par rapport au pas de temps pour le groupe de variables lentes. Les valeurs moyennes dans le temps des variables rapides (par exemple le potentiel électrique, la température électronique, la densités d'espèces gazeuses, le flux d'espèces sur les particules, le taux de nucléation, ou la force de traînée ionique) ont été utilisées comme valeurs d'entrée pour le bloc d'équations de variables lentes. Les tests paramétriques ont été effectués pour trouver les conditions optimales de répartition dans le temps (pas de temps rapides et lents, nombre de cycles RF pour le bloc variable rapide). L'approche de fractionnement du temps a été validée avec le code entièrement couplé en utilisant le même pas de temps pour les variables rapides et lentes. De plus, le temps de calcul est considérablement réduit par rapport au code entièrement couplé. Par exemple, le temps de calcul est d'environ 3 mois pour un résultat de 4 ms. À pression constante, la densité des nanoparticules diminue à mesure que la taille des nanoparticules augmente. Pour une taille donnée, la densité de particules négatives est beaucoup plus importante que les particules positives et neutres. Aussi, à taille donnée, la densité des nanoparticules

augmente avec la pression du gaz. Nous pouvons voir que les nanoparticules de plus grande taille ( $> 5$  nm) se forment à une pression plus élevée (3 ou 3,5 Torr) au temps = 4 ms. Ceci est raisonnable car une pression plus élevée provoquera plus de collisions entre les particules ou les particules avec des espèces gazeuses, ce qui favorise la croissance des particules. Enfin, nous concluons que la contribution des nanoparticules sur la vitesse de dépôt des films minces de silicium est négligeable au stade précoce de la formation des nanoparticules.

Le modèle fluide 1-D peut être utilisé pour étudier les propriétés complexes du plasma silane/hydrogène dans différentes conditions de procédé, et prédire ainsi le comportement des espèces réactives et des nanoparticules, ce qui n'est pas facilement accessible avec des techniques de mesure caractérisation in situ.

Plusieurs perspectives de recherche peuvent être dégagées. Premièrement, d'un point de vue théorique, un modèle de gaine de plasma et une distribution d'énergie ionique devraient être implémentés dans le modèle de fluide 1-D pour étudier plus avant le comportement des ions dans le plasma silane-hydrogène. Les résultats de ce modèle doivent être validés par rapport à un modèle cinétique, par exemple, le modèle particule dans la cellule. Deuxièmement, les résultats du modèle fluide 1-D doivent être comparés aux données expérimentales. Le potentiel électrique du plasma, l'énergie des électrons, les densités d'espèces gazeuses et les flux d'ions doivent être comparés aux données expérimentales. Troisièmement, l'effet des formes d'onde de tension adaptées sur les flux d'ions et les énergies dans la décharge sera étudié expérimentalement et numériquement. Quatrièmement, la force de thermophorèse pourrait être implémentée dans le modèle fluide-sectionnel 1-D pour étudier son effet sur les propriétés de transport des nanoparticules et son effet sur le dépôt de nanoparticules. Enfin, le modèle fluide-sectionnel 1-D en utilisant la méthode de fractionnement du temps peut être amélioré pour être plus rapide. Le modèle actuel n'est pas assez rapide, bien qu'il puisse faire gagner beaucoup de temps par rapport au modèle couplé.

Dans l'annexe, nous avons appliqué le modèle fluide pour étudier l'effet d'asymétrie électrique dans les plasmas silane/hydrogène lors de l'application des formes d'onde de

tension adaptées (TVW). Les formes d'onde en dents de scie et les formes d'onde de vallées sont utilisées pour étudier les effets d'asymétrie de pente et d'asymétrie d'amplitude. Pour les formes d'onde de vallée, les valeurs de l'auto-polarisation DC sont négatives lorsque des harmoniques sont ajoutées à la forme d'onde. De plus, l'auto-polarisation continue augmente lorsque le nombre d'harmoniques augmente. De plus, les flux ioniques à l'électrode alimentée sont plus importants que ceux à l'électrode mise à la terre lorsque le nombre d'harmoniques augmente, et le rapport des flux augmente jusqu'à saturation lorsque le nombre d'harmoniques est égal à 4. Pour les formes d'onde en dents de scie, le courant continu auto- la polarisation augmente considérablement jusqu'à 30 V lorsque N est égal à 2, puis elle atteint la saturation, cela est probablement dû à la puissance constante appliquée. De plus, le rapport de flux augmente et atteint la saturation lorsque N augmente. De plus, les flux d'ions  $H_3^+$  sont beaucoup plus élevés à l'électrode alimentée qu'à l'électrode mise à la terre après l'ajout d'harmoniques, ce qui joue un rôle principal dans le processus de gravure lors du dépôt de couches minces de silicium. Pour les perspectives, les résultats de la modélisation doivent être comparés aux expériences en l'avenir.

**Mots clé:** Modèle fluide 1D, décharges silane-hydrogène, modèle sectionnel, nanoparticules, vitesse de dépôt, vitesse de gravure, méthode de découplage temporel



# Contents

<b>Chapter 1 Introduction</b> .....	1
<b>1.1 Overview of plasma and silicon photovoltaics</b> .....	2
1.1.1 Classifications of plasmas .....	2
1.1.2 Silicon photovoltaics.....	5
<b>1.2 Plasma modelling</b> .....	8
1.2.1 Kinetic models .....	9
1.2.2 Fluid models.....	11
<b>1.3 Outline of the thesis</b> .....	12
References .....	14
<b>Chapter 2 1-D Fluid model of SiH<sub>4</sub>/H<sub>2</sub> plasmas</b> .....	17
2.1 Introduction.....	18
2.2 Radio-Frequency Reactor .....	20
2.3 Strained Flow .....	21
2.4 Conservation equations .....	23
2.5 Thermodynamic properties.....	25
2.6 Transport fluxes .....	26
2.7 Transport coefficients.....	27
2.8 SiH <sub>4</sub> -H <sub>2</sub> plasma chemistry .....	29
2.9 Energy exchange term .....	32
2.10 Boundary conditions.....	33
2.11 Numerical implementation.....	38
2.12 Results and discussion .....	38
2.13 Conclusions.....	43
References .....	44
<b>Chapter 3 Role of SiH<sub>x</sub> radicals and H<sub>3</sub><sup>+</sup> ions in deposition and etching of silicon thin films from SiH<sub>4</sub>/H<sub>2</sub> discharges</b> 55	
3.1 Introduction .....	50
3.2 Experimental setup and parameters.....	53
3.3 Silicon thin film characterization techniques .....	54
3.4 Results and discussions .....	57
3.5 Conclusions .....	67
References .....	68
<b>Chapter 4 Nanoparticle formation in SiH<sub>4</sub>-H<sub>2</sub> discharges</b> .....	73
4.1 Introduction .....	74
4.2 An overview of nanoparticle formation.....	75

4.3 Sectional model .....	79
4.4 Coupled 1-D fluid-sectional model.....	89
4.5 Numerical implementation .....	90
4.6 Results and discussion .....	94
4.7 Conclusions .....	104
4.8 References .....	105
<b>Chapter 5 Conclusions and Perspectives .....</b>	<b>111</b>
<b>ANNEX I. Electron collision reactions included in the fluid model.....</b>	<b>113</b>
<b>ANNEX II. Heavy species reactions included in the plasma model.....</b>	<b>115</b>
<b>ANNEX III. Net average electron energy loss in reactive collisions .....</b>	<b>117</b>
<b>ANNEX IV. List of surface reactions. ....</b>	<b>119</b>
<b>ANNEX V: The effect of tailored voltage waveforms on silane-hydrogen plasmas</b> <b>.....</b>	<b>121</b>
<b>Introduction .....</b>	<b>122</b>
<b>Simulation method .....</b>	<b>122</b>
<b>Results and Discussions.....</b>	<b>124</b>
<i>The effect of Valleys waveforms on silane/hydrogen plasmas .....</i>	<i>124</i>
<i>The effect of Sawtooth-like waveforms on silane/hydrogen plasmas .....</i>	<i>126</i>
<b>Conclusions and Perspectives.....</b>	<b>129</b>
<b>References.....</b>	<b>130</b>

# Chapter 1 Introduction

## Contents

<b>Chapter 1 Introduction .....</b>	<b>1</b>
<b>1.1 Overview of plasma and silicon photovoltaics .....</b>	<b>2</b>
<b>1.1.1 Classifications of plasmas .....</b>	<b>2</b>
<b>1.1.2 Silicon photovoltaics .....</b>	<b>5</b>
<b>1.2 Plasma modelling .....</b>	<b>8</b>
<b>1.2.1 Kinetic models .....</b>	<b>9</b>
<b>1.2.2 Fluid models .....</b>	<b>11</b>
<b>1.3 Outline of the thesis.....</b>	<b>12</b>
<b>References .....</b>	<b>14</b>

# 1.1 Overview of plasma and silicon photovoltaics

## 1.1.1 Classifications of plasmas

In the universe, plasmas constitute most of visible matter. They are considered as the fourth state of matter. In principle, plasmas are composed of positive and negative ions, electrons, neutral particles. When one applies sufficient energy to solid (the first state of matter), the relative motion of atoms increases, which results first in a transformation to a liquid (the second state of matter), then to a gas phase (the third state of matter), finally to a plasma. This transition is showed in Fig 1.1<sup>1</sup>.

Based on the ionization degree, thermodynamic equilibrium, density, and so on, plasmas can be classified in different ways. The ionization degree is defined as  $I = n_i/(n_i + n_n)$ , where  $n_n$  is the number density of neutrals and  $n_i$  is the number density of ions. The parameter  $I$  determines the response of any plasma to a magnetic or electric field. When the ionization degree  $I \approx 1$ , the plasma is called completely ionized plasma, or referred to as ‘hot’ plasma. Hot plasmas are conventional for the thermonuclear plasma systems: tokomaks<sup>2</sup>, stellarators<sup>3</sup>, solar wind and stellar interiors<sup>4</sup>. Plasmas with  $10^{-6} < I < 10^{-1}$  are called weakly ionized plasmas. Because the ionization degree is determined by the plasma electron temperature, weakly ionized plasmas are also called low-temperature plasmas<sup>1</sup>. In most plasma-based technologies, the degree of ionization is less than  $10^{-4}$ . For inductively coupled plasmas (ICP) and electron cyclotron resonance (ECR) plasmas, the ionization degree can reach  $10^{-2}$ . Low-temperature plasmas are the scope of the present thesis.

Based on the plasma temperature, plasmas are normally divided into thermal and non-thermal plasmas. The average energies of plasma species (both neutral and charged) and the related degrees of freedom (rotational, translational, vibrational and so on) determine the temperature of plasma. Therefore, plasmas may be characterized

---

<sup>1</sup> Paul K. Chu et al., *Low Temperature Plasma Technology: Methods and Applications*. CRC Press, 2013.

<sup>2</sup> A. Pironti et al., *IEEE Control Syst.*, **25**(5): 30–43, 2005.

<sup>3</sup> P. Helander et al., *Plasma Phys. Control. Fusion* **54**(12): 124009, 2012.

<sup>4</sup> J. L. Phillips et al., *Science* **268**(5213): 1030–33, 1995.

by multiple temperatures, when different groups of species are at equilibrium within the group, but not at equilibrium with other groups of species. In general, the difference in temperature between the heavy particles and the electrons is proportional to  $\sqrt{\frac{E}{p}}$ , where  $E$  and  $p$  denote the electric field and the pressure, respectively. The temperature of electrons and heavy species are similar in the case of small values of  $\sqrt{\frac{E}{p}}$  only. Therefore, this is a kind of criteria for local thermodynamic equilibrium (LTE) in plasma. In common electric discharges, the energy transfer mechanism is following: at first the electric field accelerates the electrons, because an electron possesses much smaller mass compared to the heavy species. The electrons gain energy between the collisions, then part of energy is transferred from the electrons to the heavy species during the collisions. Thus, the electron temperature is usually much higher than the temperature of heavy species in a weakly ionized plasma. Subsequently, the Joule heating mechanism (collisions between electrons and heavy species) can balance the temperature between the electrons and the heavy species, except that there is not sufficient time and energy (energy of the external electric field) to balance and there is cooling mechanism (such as in wall-cooled low-pressure discharges) preventing the heating of entire gas. In thermal plasmas, because of the high collision frequency between electrons and ions/neutrals, the temperature of electrons ( $T_e$ ), temperature of ions ( $T_i$ ) and temperature of neutrals ( $T_n$ ) are the same. For example, this type of plasma can be found in thermo-nuclear fusion and solar corona. In non-thermal plasmas, the power dissipated in the discharge is mostly absorbed by the electrons, whereas the momentum transfer between the electrons and the heavy species is inefficient. Thus, electron temperature is much higher than the temperature of ions and neutrals, namely,  $T_e \gg T_i, T_n$ . Ionization and chemical processes in such plasmas are determined by the electron temperature. The methods to generate this type of plasma include glow discharge, corona discharge, arc discharge, wave heated plasma, capacitively coupled discharge, inductively coupled discharge, and so many others. Applications of nonthermal plasmas cover a large number of fields, which include photovoltaics<sup>5</sup>,

---

<sup>5</sup> Mario Moreno et al., *Phys. Status Solidi c* 7, 3–4: 1112–15, 2010.

semiconductor chip fabrication, aerospace engineering, biomedicine<sup>6,7</sup>, plasma coating by plasma chemical and physical vapor deposition<sup>8</sup>, *etc.* This thesis focuses on numerical and experimental studies of nonthermal plasmas for photovoltaics.

Also, plasmas can be classified into pristine plasmas and dusty plasmas (or complex plasmas) according to the presence of nanoparticles in plasma. The dusty plasmas are often generated in the electronegative gas discharges at high pressure regime (within Torr range). In dusty plasmas, the electron attachment reactions that mainly contribute to the formation of nanoparticles are dominant. The pristine plasmas are often generated in electropositive gas discharges or in the electronegative gas discharges at low-pressure regime. In pristine plasmas, the electron ionization and dissociation reactions are the dominant ones.

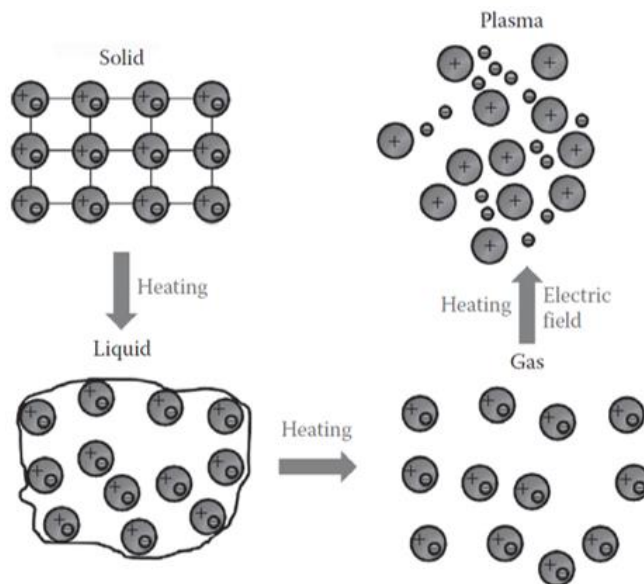


Fig 1.1 The transition of states of matter on application of heat<sup>1</sup>.

Figure 1.2 shows the natural and man-made plasmas depending on typical parameters<sup>9</sup>. In this thesis, we are interested in nonthermal (weakly ionized) plasmas, usually generated at high pressure (few Torr regime). When the gas pressure is high enough, the formation of nanoparticles occurs. The transition from the pristine plasma to dusty plasma is also considered in this thesis, as will be detailed below.

<sup>6</sup> David B. Graves, *Phys. Plasmas*, **21**(8): 080901, 2014.  
<sup>7</sup> Natalia Yu. Babaeva et al., *Trends Biotechnol.*, **36**(6): 603–14, 2018.  
<sup>8</sup> Thermal Chemical Vapor Deposition, an Overview |ScienceDirect Topics.  
<sup>9</sup> Alexander Fridman, *Plasma Chemistry*, Cambridge University Press, 2008.

## 1.1.2 Silicon photovoltaics

Non-thermal low temperature plasmas are used for photovoltaics, semiconductor processing, plasma treatment in aerospace, automotive, biomedical, or waste management industries<sup>10</sup>. In this thesis, silicon photovoltaics is the application we are interested in.

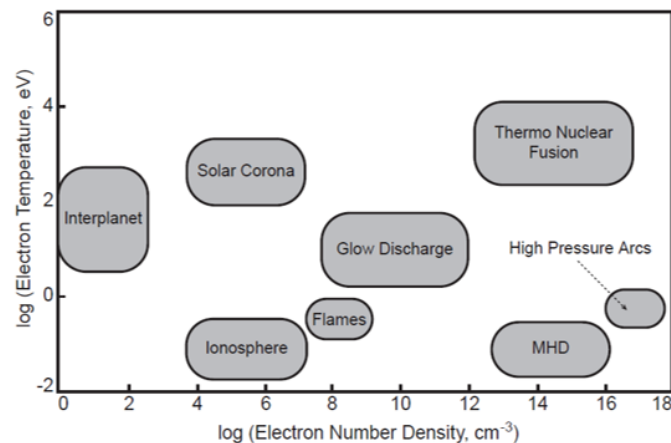


Fig 1.2 Typical range of the electron temperature and electron density for different types of plasma discharges. The capacitively coupled plasmas and inductively coupled plasmas belong to glow discharges<sup>9</sup>.

Cumulative global production of solar photovoltaic (PV) technology increased from 1.4 GW in 2000 to 512 GW in 2018. Currently, photovoltaics produces nearly 3% of global electricity, with crystalline silicon (c-Si) modules (also known as panels) constituting more than 90% of the global PV market<sup>11</sup>. As shown in Fig 1.3, a solar module is made up of connecting single solar cells, and combination of solar modules is called solar panel. A solar cell is the semiconductor device which converts photon energy to electrical energy. The voltage generated by a solar cell depends on the light intensity incident on it. The photovoltaic effect (discovered by Edmond Becquerel) is the basis of light-to-electricity conversion for solar cells. Fig 1.4 shows the typical structure of a p-n junction silicon solar cell. The working principles of solar cells are

<sup>10</sup> Favia P. et al, Advanced plasma technology, Weinheim: Wiley-VCH, 2008.

<sup>11</sup> Garvin A. Heath et al., *Nat. Energy*, 5(7): 502–10, 2020.

detailed in many books<sup>12,13</sup>.

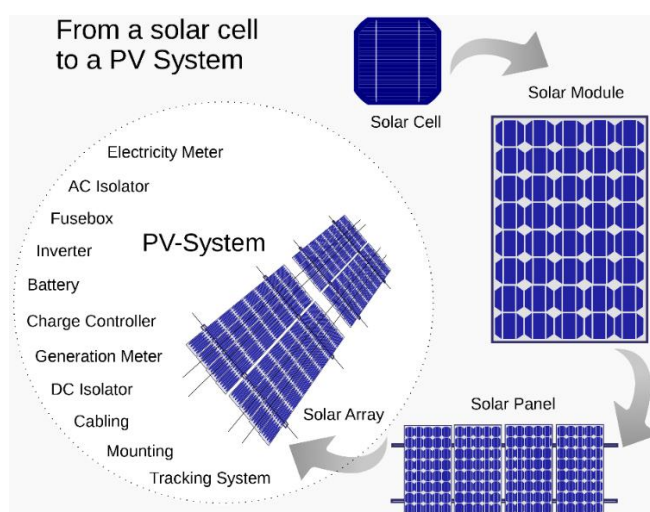


Fig 1.3 From a solar cell to a PV system<sup>14</sup>.

Plasma-enhanced chemical vapor deposition (PECVD) is a process that is often used for the production of silicon thin film solar cells. Compared with the conventional CVD methods, PECVD has the advantages of low deposition temperature, high purity, good step coverage (especially for amorphous silicon) and easy control of reaction parameters<sup>15</sup>. Gas chemistry for the deposition of silicon thin films can be based on using gas mixtures of  $\text{SiH}_4/\text{H}_2$ ,  $\text{SiH}_4/\text{Ar}$ ,  $\text{SiF}_4/\text{H}_2$ , and so on. The  $\text{SiH}_4/\text{H}_2$  chemistry is studied in this thesis. The plasma is created by radio frequency (RF) or direct current (DC) discharge between two electrodes. We focus on the numerical and experimental studies of the RF capacitively coupled plasmas (CCP). When RF CCP discharge is ignited, the complex chain of chemical reactions results in the production of radicals, neutrals, positive and negative ions, nanoparticles and dust. These species and nanoparticles contribute to the film deposition onto the substrates, whereas dust is probably pumped away from the reactor. In fact, nanoparticles' formation can be adjusted by varying the parameters of gas discharge - gas pressure, temperature, power, gas flow rates, *etc.* As shown in Fig 1.5, at low pressure the deposited films are microcrystalline ( $\mu\text{-Si:H}$ ), which is formed by pristine plasma where radicals and ion

<sup>12</sup> Francesco E. et al, *Solar Cells and Light Management: Materials, Strategies and Sustainability*, Elsevier, 2019.

<sup>13</sup> Alan F. et al, *Fundamentals of Solar Cells: Photovoltaic Solar Energy Conversion*, Elsevier, 2012.

<sup>14</sup> Solar Panel, *Wikipedia*.

<sup>15</sup> Masahiko M. et al, *Thin Solid Films*, **489**(1): 320–24, 2005.

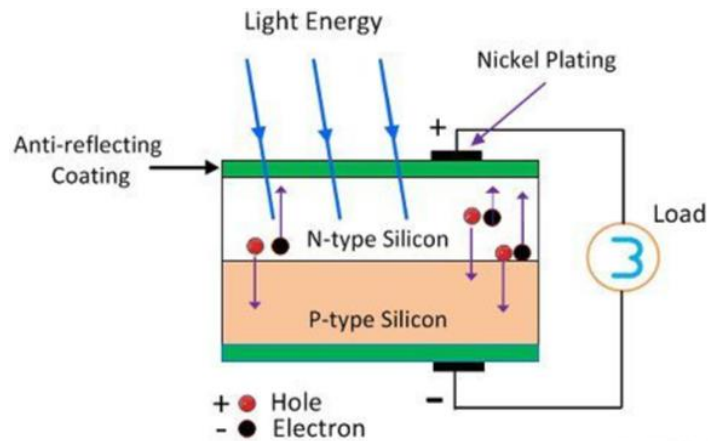


**Fig 1.4** Cross section representation of a silicon solar cell<sup>16</sup>.

species mainly contribute to the film growth. With pressure increase, the nanoparticles start to form and contribute to the film deposition. These nanoparticles can be amorphous (a-Si:H) or crystalline silicon (c-Si). If their bombardment energy is too high, they will result in an amorphous film. When pressure increases above 1500mTorr, a sharp increase in deposition rate occurs, that is normally called  $\alpha - \gamma$  transition<sup>17</sup>. Agglomerates can become very large with further pressure increase, and result in the formation of powders. Large powder particles will get negatively charged and trapped in the bulk of discharge, and finally exhausted from the reactor, in which case they can damage thin films. As a consequence, the deposition rate decreases. Silicon clusters with nanometer size can contribute to the deposition onto the substrate and result in the growth of polymorphous silicon films on glass substrates or epitaxial growth on c-Si. In our study, we pay special attention to the transition from the pristine plasma conditions, where radicals and ions contribute to the deposition of  $\mu\text{c-Si:H}$  or a-Si:H films, to the nanoparticle formation conditions, where nanoparticles lead to an increase in deposition rate. Thus, capacitively coupled plasmas are complex systems where the optimization of the process parameters (gas flow rates, RF power, total pressure, and substrate temperature) to produce high quality silicon thin films is based on carrying out many sets of experiments. Therefore, the plasma modelling, together with the experimental studies, is imperative to investigate the silane/hydrogen plasma dynamics

<sup>16</sup> What Is Photovoltaic or Solar Cell? - Definition, Construction, Working & Installation, *Circuit Globe*.

<sup>17</sup> J. Perrin et al., *Plasma Sources Sci. Technol.* 3(3): 252–61, 1994.

and to optimize the process parameters for obtaining high quality silicon thin films.

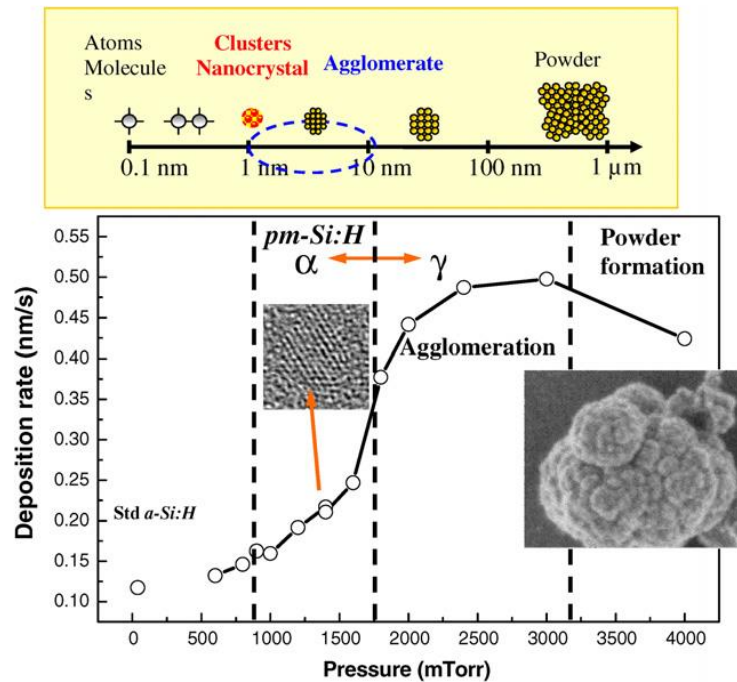


**Fig. 1.5** Deposition rate as a function of pressure for a 3% silane in hydrogen mixture at 250 °C at RF power of 22W<sup>18</sup>.

## 1.2 Plasma modelling

Plasma modeling is an essential activity in low temperature plasma (LTP) science and engineering that supports the plasma diagnostics. The use of plasma modeling may help<sup>19,20,21</sup>: (a) to predict the values of plasma parameters that are not easily accessible during the experiments, such as gas species densities, electrical potential and so on; (b) to explain experimental data and to guide optimization of the experiments; (c) to design of novel plasma reactors for etching and deposition processes.

Two main types of approaches are used for plasma simulation, namely, fluid and kinetic ones. The hybrid models are derived by combining fluid and kinetic models. The criteria of choosing between the kinetic or fluid model are based on the typical values of Knudsen number  $K_n$  for the studied process. In general,  $K_n = \lambda/L$ . Here,  $\lambda$  is a mean free path of the species, and  $L$  is a characteristic length of the reactor, for

<sup>18</sup> P. Roca i Cabarrocas et al., *J. Phys. D:Appl. Phys.* **40**(8): 2258–66, 2007.

<sup>19</sup> H. C. Kim et al., *J. Phys. D: Appl. Phys.* **38**(19): R283–301, 2005.

<sup>20</sup> D. J. Economou, *Thin Solid Films*, **365**(2): 348–67, 2000.

<sup>21</sup> G. G. Lister, *J. Phys. D: Appl. Phys.*, **25**(12): 1649–80, 1992.

example, the inter-electrode distance in 1-D model. Kinetic models are generally applicable when the values of  $K_n > 0.1$ . Kinetic models are considered more accurate than fluid models, especially at low pressures. But they are also computationally expensive compared to the fluid model. The kinetic models include Particle-In-Cell, and Monte Carlo algorithm, as well as the direct solution of the Boltzmann equation. When  $K_n < 0.1$ , the fluid models are used and they produce reliable results. In a fluid model, the continuity equations for species density, momentum, and energy are solved. The most important advantage of the fluid models is faster calculation time compared to the corresponding kinetic models. It allows modelling of more complex discharge chemistry with more species and reactions taken into account. Consequently, the parametric studies can be conducted to investigate the impact of reactor design and operating conditions on the discharge characteristics and process outcomes, such as species densities, deposition rate, etc.

### 1.2.1 Kinetic models

The most common kinetic model is based on the particle-in-cell (PIC) approach. PIC simulation models the collective behavior of the set of charged particles in plasma to simulate the dynamics of various species by modelling a reduced number of computer particles (also called super-particles)<sup>22,23,24</sup>. In general, one super-particle represents up to  $10^{5-7}$  real particles in one-dimensional simulations. In PIC model, the Newton–Lorentz equation is solved for the motion of charged particles, coupled with the Maxwell equations for the self-consistent calculation of the electric and magnetic fields. Therefore, without making any assumption on their velocity distribution, the super-particles are traced by the solution of these fundamental equations, the dynamics of each species is simulated with few approximations. It is assumed that the neutral particles in the background are uniformly distributed in space. By solving the Kirchhoff circuit equation and the Maxwell equation simultaneously, the boundary conditions

---

<sup>22</sup> C. K. Birdsall et al, Plasma Physics via Computer Simulation, *CRC Press*,2004.

<sup>23</sup> T. Tajima, Computational Plasma Physics: With Applications To Fusion And Astrophysics, *CRC Press*, 2018.

<sup>24</sup> R. W. Hockney et al, Computer Simulation Using Particles, *CRC Press*, 2021.

imposed by the external circuit can be considered in a self-consistent manner<sup>25</sup>, which is also the case in fluid models.

The general flow chart of a PIC simulation is presented in Fig. 1.6<sup>26</sup>. Initially, the particles are distributed within the simulation domain and velocity space, and then a system of Maxwell's equations is solved to self-consistently determine the electric and magnetic fields. At each time step, the positions and velocities of the particles are updated by solving the Newton-Lorentz equations. After the particles advance, the collisions are merged into the simulation by applying a Monte Carlo Collision (MCC) scheme. The MCC module determines statistically the particles that collide and their velocities. Also, the interplay between the surface and particles is simulated at this time by calculating the absorption, reflection, and emission of the particles at the boundaries. Poisson's equation (in electrostatic approximation) or Maxwell's equations are then solved to identify the self-consistent fields. This step is completed after the charge density is determined by weighting the particle densities onto the grid where the fields are calculated. After the fields are calculated, time will advance and the next iteration will start.

The PIC simulations have their strengths and limitations. The major limitation is the computation time, which is proportional to the number of super-particles. Thus, it is better to keep the number of super-particles as low as possible. When choosing the number of super-particles, one should consider (1) sufficient statistical representation of the energetic particles; (2) noise; (3) Numerical heating<sup>27</sup>. Because of these limitations on the number of super-particles, PIC models are computationally more demanding than fluid models. The large number of particles required to simulate each species limits the number of species that can be included in the model. Therefore, PIC models are generally not used for the modelling of low-temperature plasmas with complex chemical reactions involving many species. However, since the solution of the basic equations requires only a few assumptions, the dynamics of the species can be accurately simulated, including local and non-local effects. Thus, PIC models are

---

<sup>25</sup> J. P. Verboncoeur et al., *J. Comput. Phys.*, **104**(2): 321–28, 1993.

<sup>26</sup> Kim et al., *J. Phys. D: Appl. Phys.*, **38**(19): R283, 2005.

generally used to model low particle density discharges where the non-local effects are essential and the MCC scheme can be solved quickly.

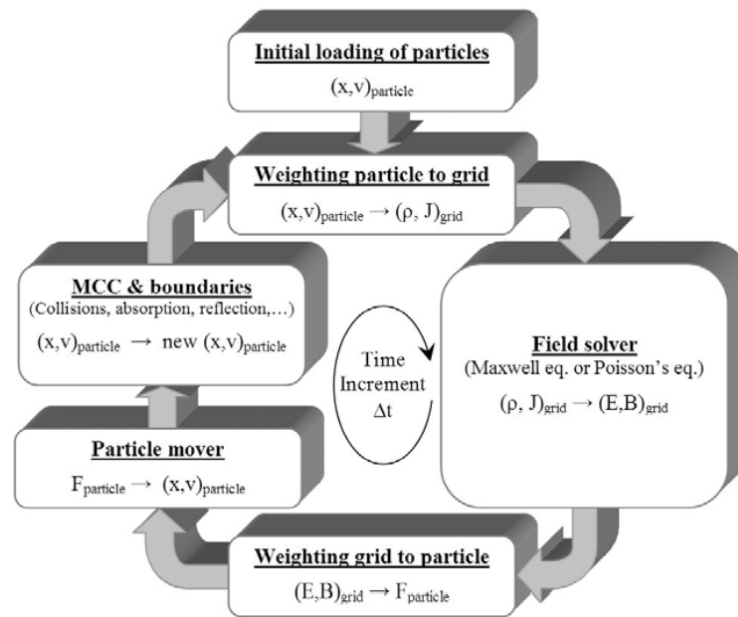


**Fig. 1.6** Flow chart of a PIC-MCC model<sup>27</sup>.

## 1.2.2 Fluid models

The fluid plasma models are employed when the Knudsen number  $K_n < 0.1$ . In general, fluid models solve the continuity equations for gas species density, momentum, and energy, that are derived from the Boltzmann equations<sup>27</sup>. The Poisson equation (in electrostatic approximation) or Maxwell equations are coupled with the fluid equations to obtain self-consistent electric/magnetic fields. Instead of using flux balance equation, the drift–diffusion approximation can be applied if the momentum transfer collisional frequency is larger than the radio frequency (RF) driving frequency. However, in order to achieve the ‘closure’ of the continuity equations, an assumption is necessary regarding the species velocity distribution function. Maxwellian distribution is the most common assumption.

The main approximation in the fluid model is based on the assumption of a specific

<sup>27</sup> T. Makabe, *Appl. Surf. Sci.*, **192**, 2002.

velocity distribution for the local values of the electric field. There are two particular cases when fluid models are not applicable. First, when the ratio of the electric field over the pressure  $E/p$  is ‘too high’, the electron distribution function departs strongly from a Maxwellian distribution. Second, when the collision frequency is comparable with the electric field frequency, the species distribution function may also depart from the Maxwellian distribution. Thus, fluid simulations are better suited for the high-pressure discharges. However, if the electric field is large, the nonlocal phenomena may occur even in high-pressure discharges<sup>28</sup>, (e.g. cathode drop zones and the micro-discharges). Despite this limitation, the fluid models are widely employed due to their advantages in terms of the computational speed. 2-D and 3D fluid models can be run in a fairly short period of time. In addition, a large number of species can be modeled, allowing the study of complex chemistry with multiple reactions. These problems are more difficult to solve using PIC models. In the thesis, we apply a fluid model to conduct the study of silane-hydrogen discharge in a RF capacitively coupled plasma reactor. The detailed description of the fluid model will be provided in the next chapter.

### 1.3 Outline of the thesis

In this thesis, a fluid model developed from the Ph.D. work of J. M. Orlac’h<sup>29</sup> is used to study the silane-hydrogen plasmas at relatively high pressure range (1 – 4Torr), that corresponds to transition from pristine plasma to dusty plasma. The outline of the thesis is described below:

In the second chapter, a self-consistent two-temperature fluid model is presented in details. The model includes the continuity equations for the gas species and electron energy, Poisson’s equation for the electrical potential and the conservation equations for both tangential and normal velocity. Also, a detailed gas phase chemistry and surface chemistry is discussed. Specifically, a complete surface chemistry module was developed. The surface chemistry including recombination, etching, and deposition

---

<sup>28</sup> F. Iza et al., *J. Appl. Phys.*, **98**(4): 043302, 2005.

<sup>29</sup> Jean-Maxime Orlac’h, Modeling of a Silane-Hydrogen Plasma Discharge Including Nanoparticle Dynamics for Photovoltaic Applications, These de doctorat, Université Paris-Saclay, 2017.

reactions is coupled to the fluid model via a set of reaction probabilities. In addition, the numerical algorithms to solve these equations are also described.

In the third chapter, the deposition process in silane-hydrogen plasmas is investigated with fluid model simulations. Many researchers have studied the role of the gas species, especially the radicals, that are considered to be the main precursors for the deposition of silicon thin films. However, the role of ions in deposition or etching of the silicon thin films has not been studied yet by modelling. Thus, the impact of ions on the deposition rate, and in particular the role of  $H_3^+$  ions on the etching, was studied using our fluid model, and the results are compared with experiments.

In the fourth chapter, a sectional model used to describe nanoparticle's formation is coupled with the fluid model. Particle nucleation, coagulation, surface growth, charge fluctuation and transport are taken into account. However, the fluid – sectional coupled model is very time-consuming and inefficient, thus, a time-splitting method is employed in order to make the model computationally efficient. This method is based on exploring the different time scales of charged species, particles and neutrals. This time-splitting model is validated with the fully coupled code using the same process conditions for both simulations. Then, the effect of gas pressure on the density of nanoparticles is studied. The contribution of nanoparticles on silicon thin films is estimated and compared with the experiments.

Finally, the summary of the thesis is presented and the perspectives are drawn for future work.

## References

- <sup>1</sup> K. C. Paul and X. Lu. *Low Temperature Plasma Technology: Methods and Applications*. CRC Press, 2013.
- <sup>2</sup>A. Pironti and M. Walker. Fusion, Tokamaks, and Plasma Control: An Introduction and Tutorial, *IEEE Control.Syst.*,**25**(5):30–43, 2005, <https://doi.org/10.1109/MCS.2005.1512794>.
- <sup>3</sup>P. Helander, C. D. Beidler, T. M. Bird, M. Drevlak, Y. Feng, R. Hatzky, F. Jenko, R. Kleiber, J. H. E. Proll, Yu. Turkin and P. Xanthopoulos. Stellarator and Tokamak Plasmas: A Comparison, *Plasma Phys. Control. Fusion*. **54**(12):124009, 2012, <https://doi.org/10.1088/0741-3335/54/12/124009>.
- <sup>4</sup>J. L. Phillips, S. J. Bame, W. C. Feldman, J. T. Gosling, C. M. Hammond, D. J. McComas, B. E. Goldstein, M. Neugebauer, E. E. Scime, S. T. Suess. Ulysses Solar Wind Plasma Observations at High Southerly Latitudes, *Science*. **268**(5213):1030-1033, 1995, <https://doi.org/10.1126/science>.
- <sup>5</sup>M. Moreno, D. Daineka, and P. Roca i Cabarrocas, Plasmas for Texturing, Cleaning, and Deposition: Towards a One Pump down Process for Heterojunction Solar Cells, *Phys. Status Solidi c* 7, no. 3–4:1112–15, 2010, <https://doi.org/10.1002/pssc.200982704>.
- <sup>6</sup>D. B. Graves, Low Temperature Plasma Biomedicine: A Tutorial Review, *Phys. Plasmas* **21** (8): 080901, 2014, <https://doi.org/10.1063/1.4892534>.
- <sup>7</sup>Natalia Yu. Babaeva and George V. Naidis, Modeling of Plasmas for Biomedicine, *Trends Biotechnol.*, **36**(6): 603–14, 2018, <https://doi.org/10.1016/j.tibtech.2017.06.017>.
- <sup>8</sup>Thermal Chemical Vapor Deposition an Overview in ScienceDirect Topics, <https://www.sciencedirect.com/topics/chemistry/thermal-chemical-vapor-deposition>.
- <sup>9</sup>A. Fridman, Plasma Chemistry, *Cambridge University Press*, 2008, <https://doi.org/10.1017/CBO9780511546075>.
- <sup>10</sup> R. d'Agostino, P. Favia, Y. Kawai, H. Ikegami, N. Sato, F. Arefi-Khonsari, Advanced Plasma Technology, *Wiley*, 2008.
- <sup>11</sup> G. A. Heath, T. J. Silverman, M. Kempe, M. Deceglie, D. Ravikumar, T. Remo, H. Cui, P. Sinha, C. Libby, S. Shaw, K. Komoto, K. Wambach, E. Butle

r, T. Barnes and A. Wade, Research and Development Priorities for Silicon Photovoltaic Module Recycling to Support a Circular Economy, *Nat. Energy*, **5**(7): 502–10, 2020, <https://doi.org/10.1038/s41560-020-0645-2>.

<sup>12</sup> F. Enrichi and G. Righini, Solar Cells and Light Management: Materials, Strategies and Sustainability, *Elsevier*, 2019.

<sup>13</sup> A. Fahrenbruch and R. Bube, Fundamentals Of Solar Cells: Photovoltaic Solar Energy Conversion, *Elsevier*, 2012.

<sup>14</sup> Solar Panel, in *Wikipedia*, [https://en.wikipedia.org/w/index.php?title=Solar\\_panel&oldid=1011699762](https://en.wikipedia.org/w/index.php?title=Solar_panel&oldid=1011699762).

<sup>15</sup> M. Maeda and T. Watanabe, Evaluation of Photocatalytic Properties of Titanium Oxide Films Prepared by Plasma-Enhanced Chemical Vapor Deposition, *Thin Solid Films*, **489**(1): 320–24, 2005 <https://doi.org/10.1016/j.tsf.2005.05.007>.

<sup>16</sup> What Is Photovoltaic or Solar Cell? - Definition, Construction, Working & Installation, *Circuit Globe* (blog), 2018, <https://circuitglobe.com/photovoltaic-or-solar-cell.html>.

<sup>17</sup> J. Perrin, C. Bohm, R. Etemadi and A. Lloret, Possible Routes for Cluster Growth and Particle Formation in RF Silane Discharges, *Plasma Sources Sci. Technol.* **3**(3): 252–61, 1994, <https://doi.org/10.1088/0963-0252/3/3/003>.

<sup>18</sup> P. Roca i Cabarrocas, Th Nguyen-Tran, Y. Djeridane, A. Abramov, E. Johnson and G. Patriarche, Synthesis of Silicon Nanocrystals in Silane Plasmas for Nanoelectronics and Large Area Electronic Devices, *J. Phys. D.: Appl. Phys.* **40**(8): 2258–66, 2007, <https://doi.org/10.1088/0022-3727/40/8/S04>.

<sup>19</sup> H. C. Kim, F. Iza, S. S. Yang, M. Radmilović-Radjenović and J. K. Lee, Particle and Fluid Simulations of Low-Temperature Plasma Discharges: Benchmarks and Kinetic Effects, *J. Phys. D.: Appl. Phys.* **38**(19): R283–301, 2005, <https://doi.org/10.1088/0022-3727/38/19/R01>.

<sup>20</sup> D. J. Economou, Modeling and Simulation of Plasma Etching Reactors for Microelectronics, *Thin Solid Films* **365**(2): 348–67, 2000, [https://doi.org/10.1016/S0040-6090\(99\)01056-1](https://doi.org/10.1016/S0040-6090(99)01056-1).

- <sup>21</sup> G. G. Lister, Low-Pressure Gas Discharge Modelling, *J. Phys. D.: Appl. Phys.* **25**(12): 1649–80, 1992, <https://doi.org/10.1088/0022-3727/25/12/001>.
- <sup>22</sup> C. K. Birdsall, A.B Langdon, Plasma Physics via Computer Simulation, *CRC Press*, 2004.
- <sup>23</sup> T. Tajima, Computational Plasma Physics: With Applications To Fusion And Astrophysics, *CRC Press*, 2018.
- <sup>24</sup> R. W. Hockney and J.W Eastwood, Computer Simulation Using Particles, *CRC Press*, 2021.
- <sup>25</sup> J. P. Verboncoeur, M.V.Alves, V.Vahedi, C.K.Birdsall, Simultaneous potential and circuit solution for 1D bounded plasma particle simulation codes, *J. Comput. Phys.* **104**(2): 321–28, 1993, <https://doi.org/10.1006/jcph.1993.1034>.
- <sup>26</sup> H. C. Kim, F. Iza, S. S. Yang, M. Radmilović-Radjenović and J. K. Lee, Particle and fluid simulations of low-temperature plasma discharges: benchmarks and kinetic effects, *J. Phys. D: Appl. Phys.*, **38**(19): R283, 2005, <https://doi.org/10.1088/0022-3727/38/19/R01>.
- <sup>27</sup> T. Makabe, Advances in low temperature rf plasmas: Basis for process design, *Appl. Surf. Sci.* **192**, 2002, <http://pascal-francis.inist.fr/vibad/index.php?action=getRecordDetail&idt=13354418>.
- <sup>28</sup> F. Iza, S. S. Yang, H. C. Kim, and J. K. Lee, The mechanism of striation formation in plasma display panels, *J. Appl. Phys.*, **98**(4): 043302, 2005, <https://doi.org/10.1063/1.2007851>.
- <sup>29</sup> Jean-Maxime Orlac'h, Modeling of a Silane-Hydrogen Plasma Discharge Including Nanoparticle Dynamics for Photovoltaic Applications, These de doctorat, Université Paris-Saclay, 2017, <http://www.theses.fr/2017SACLX023>.

# Chapter 2 1-D Fluid model of SiH<sub>4</sub>/H<sub>2</sub> plasmas

## Contents

Chapter 2 .....	17
1-D Fluid model of SiH <sub>4</sub> /H <sub>2</sub> plasmas .....	17
2.1 Introduction.....	18
2.2 Radio-Frequency Reactor .....	20
2.3 Strained Flow .....	21
2.4 Conservation equations .....	23
2.5 Thermodynamic properties .....	25
2.6 Transport fluxes .....	26
2.7 Transport coefficients .....	27
2.8 SiH <sub>4</sub> -H <sub>2</sub> plasma chemistry .....	29
2.9 Energy exchange term.....	32
2.10 Boundary conditions.....	33
2.11 Numerical implementation.....	38
2.12 Results and discussion .....	38
2.13 Conclusions.....	43
References .....	44

## 2.1 Introduction

Self-consistent modelling of radio-frequency (RF) plasma discharges is crucial for the understanding and optimization of PECVD processes widely used in the fabrication of electronic and photovoltaic devices. In our study, a 1D fluid model is employed to describe silane/hydrogen radio frequency plasma discharges, which is based on previous Ph.D. student's work (J.M. Orlac'h)<sup>1,2</sup>. This model is enriched with a detailed chemistry for silane-hydrogen discharge as well as the surface reactions to account for deposition and etching processes of silicon thin films. First, fluid models<sup>3</sup> are more time-efficient than kinetic models, such as Particle-in-cell and Monte Carlo models. Fluid model<sup>4</sup> allows more complex chemistries to be included and parametric investigations to be conducted to assure the effect of operating parameters on discharge characteristics and process outcomes (e.g., growth rate). Besides, industrial reactors for flat panel display and photovoltaic applications have large area electrodes (up to 10 m<sup>2</sup>) and small inter-electrode distance (~1 cm), therefore the 1-D model is valid.

Silane/hydrogen plasma discharges have been widely studied numerically and experimentally. The group of D. Mataras<sup>5</sup> studied the effect of radio frequency (13.56-50 MHz) under conditions of constant power dissipation on the properties of highly diluted SiH<sub>4</sub> in H<sub>2</sub> discharges used for the deposition of  $\mu\text{c-Si:H}$  thin films through optical measurements coupled with a model of plasma physics and a mass transfer model. They found that the increase of frequency induces a decrease of electrical field in the sheath and sheath width and an increase of electron density and power absorbed by electrons. This leads to the enhancement of SiH<sub>4</sub> electron impact dissociation due to the increase of electron density. Moreover, increase of hydrogen dissociation results in higher hydrogen flux towards the surface that favors the growth of  $\mu\text{c-Si:H}$  films. Also, their works<sup>6,7,8</sup> combined experimental measurements with modeling, presenting a set

---

<sup>1</sup> J. M. Orlac'h et al., *Plasma Sources Sci. Technol.*, 28(5): 055003,2019.

<sup>2</sup> J. M. Orlac'h et al., *Physica A*, 494: 503–46,2018.

<sup>3</sup> D. B. Graves et al., *IEEE T. Plasma. Sci.*, 14(2): 78–91,1986.

<sup>4</sup> D. J. Economou, *Plasma Processes Polym.*, 14(1–2): 1600152,2017.

<sup>5</sup> E. Amanatides et al, *J. Appl. Phys.*, 90(11): 5799–5807,2001.

<sup>6</sup> E. Amanatides et al, *Le Journal de Physique IV*, 11(PR3): Pr3-Pr3-722,2001.

<sup>7</sup> E. Amanatides et al, *J. Appl. Phys.*, 90(11): 5786–98, 2001.

<sup>8</sup> E. Amanatides et al, *J. Appl. Phys.*, 97(7):073303, 2005.

of reliable analysis starting from the electrical plasma properties and plasma chemistry to the film growth rate and film properties, and found that the increase of RF power favors the flux of hydrogen atoms relative to all other radicals, independent of the total pressure and the SiH<sub>4</sub> fraction in the gas mixture. The production of SiH<sub>3</sub> radicals was found to be favored relative to all other silicon radicals by the increase of power, especially at higher SiH<sub>4</sub> fractions, however, this radical always had a limited role in the film growth. The group of A.Matsuda<sup>9</sup> studied the relation of deposition rate and crystallinity with process parameters, such as gas pressure, dilution ratio and input RF power. By combining process conditions of high pressure and silane depletion, they found that low-defect-density and high-crystallinity  $\mu\text{c-Si:H}$  can be obtained at a high deposition rate of 9.3 Å/s using a conventional RF-PECVD method.

In this chapter, a 1-D fluid model is presented to study SiH<sub>4</sub>/H<sub>2</sub> plasmas. The model has been previously validated for H<sub>2</sub> plasma discharges<sup>1</sup>. This model consists of coupling the Poisson equation for the electric potential with a set of drift-diffusion and transport equations for charged and neutral species, respectively. The electron temperature is modeled self-consistently by solving electron energy equation. The model accounts for plasma thermal non-equilibrium, two temperature chemistry (electron temperature is much higher than ions and neutrals temperature, namely,  $T_e \gg T_i, T_n$ ) including electron collision reactions and heavy-species reactions, and coupling between charged species dynamics and electric potential. It is worth to mention that we integrate deposition and etching in 1-D fluid model by using a set of surface chemical reactions. For each species, there are three probabilities to react with substrate (sticking, recombination and etching). The content of this chapter is as follows: (1) Introduction. The fluid model is validated and a brief review about the study of silane/hydrogen plasmas is given. (2) Setup of the radio-frequency reactor. (3) Model description. The formulations in the fluid model are reviewed, including conservation equations, thermodynamic properties, transport fluxes, chemical reactions, boundary conditions and external circuit. (4) Results and discussion. We will discuss the effect of silane

---

<sup>9</sup> A. Matsuda, Thin Solid Films, 337(1): 1–6,1999.

dilution and gas pressure in silane/ hydrogen discharges on plasma parameters, such as electron temperature, important chemical reactions, species densities, and the deposition rate and etching rate which are compared with experimental results. (5) Conclusions.

## 2.2 Radio-Frequency Reactor

A capacitively coupled parallel plate (CCPP) reactor, having a base vacuum of  $10^{-7}$  mbar, was used for silicon thin film deposition<sup>10</sup>. Fig. 2.1 shows a schematic representation of one of the chambers of the reactor. The plasma chamber is axisymmetric around the  $e_z$  axis, with corresponding polar coordinates  $e_r$  and  $e_\theta$ . The silane-hydrogen gas mixture is injected from the 15 cm diameter RF electrode side as shown in the figure. The upper electrode carrying the substrates is grounded and the gases are pumped via a slit between the substrate holder and a plasma box confining the discharge between the two electrodes. A steady flow is generally established in the reactor with a prescribed gas temperature and uniform pressure before turning the plasma on. After the plasma is ignited, plasma sheaths near the electrodes and plasma bulk in the central region of the discharge are formed. In the sheaths, secondary electrons are accelerated and collide with neutral species, which induces ionization, excitation, dissociation, and attachment to the carrier gas. The gas mixture is weakly ionized; radicals and positive ions produced by these reactions may deposit or etch onto the substrates or on the reactor walls.

---

<sup>10</sup> P. Roca. i Cabarrocas et al , *J. Vac. Sci. Technol. A*, 9(4): 2331–41, 1991.

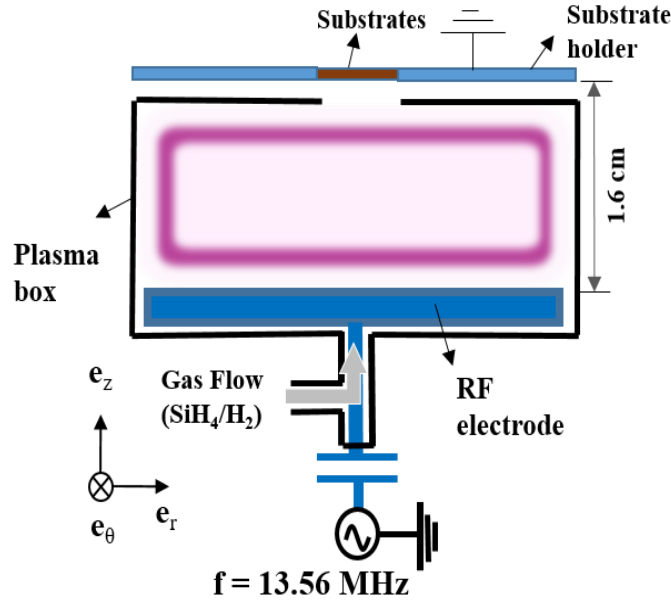


**Figure 2.1** Schematic representation of the axisymmetric radio-frequency reactor.

## 2.3 Strained Flow

### 2.3.1 Low Mach Number Flow

The Mach number  $\xi$  is the ratio of a characteristic macroscopic velocity  $v^*$  over a characteristic sound speed  $v^s$ , which is a measure of the compressibility characteristics of fluid flow. In the PECVD process, the Mach number is much small compared to one

$$\xi = \frac{v^*}{v^s} \ll 1 \quad (2.3.1)$$

the sound speed is not constant. For an ideal gas mixture, a characteristic sound speed is considered as:

$$v^s = \sqrt{\frac{p^*}{\rho^*}} \quad (2.3.2)$$

where  $p^*$  represents a characteristic pressure and  $\rho^*$  is a characteristic mass density of the fluid.

### 2.3.2 Flow model

Under the scaling listed above, the total mass conservation equation and momentum conservation equation<sup>11</sup> are listed as follows:

<sup>11</sup> Vincent Giovangigli, Multicomponent Flow Modeling, Birkhäuser Basel, 1999.

$$\partial_t \rho + \partial_x \cdot (\rho \vec{v}) = 0 \quad (2.3.3)$$

$$\partial_t (\rho \vec{v}) + \partial_x \cdot (\rho \vec{v} \otimes \vec{v}) + \partial_x p + \partial_x \cdot \vec{\Pi} = \rho \vec{g} \quad (2.3.4)$$

where  $\rho$  is the density of the mixture,  $\vec{v}$  is the mass-averaged velocity,  $\vec{\Pi}$  is the viscous tensor,  $\vec{g}$  is the gravity vector, where  $(\vec{v} \otimes \vec{v}) = \vec{v}\vec{v}$ .

Under plasma enhanced chemical vapor deposition, the process flow is considered as strained flow. The cylindrical coordinates  $(r, \theta, z)$ , with corresponding unit vectors  $\mathbf{e}_r$ ,  $\mathbf{e}_\theta$  and  $\mathbf{e}_z$ . Here,  $\vec{v} = (u, 0, w)$ ,  $\vec{g} = (0, 0, g)$ . Under this coordinates, the dependence of variables mentioned are as follows:

$$\begin{aligned} \rho &= \rho(t, z) \\ u &= r\hat{u}(t, z) \\ w &= w(t, z) \\ p &= -J(t)\frac{r^2}{2} + \hat{p}(t, z) \\ T &= T(t, z) \end{aligned} \quad (2.3.5)$$

Where  $J(t)$  represents the pressure curvature in the tangential direction. After substituting the Eq. (2.3.5) into the Eq. (2.3.3) and Eq. (2.3.4), we can achieve the equations as follows:

$$\partial_t \rho + 2\rho\hat{u} + \partial_z(\rho w) = 0 \quad (2.3.6)$$

$$\rho \partial_t \hat{u} + \rho \hat{u}^2 + \rho w \partial_z \hat{u} = J + \partial_z(\eta \partial_z \hat{u}) \quad (2.3.7)$$

$$\begin{aligned} \rho \partial_t w + \rho w \partial_z w &= -\partial_z \hat{p} + 2\eta \partial_z \hat{u} + 2\partial_z \left( \left( \kappa - \frac{2}{3}\eta \right) \hat{u} \right) + \partial_z \left( \left( \kappa + \frac{4}{3}\eta \right) \partial_z w \right) + \\ &\rho g \end{aligned} \quad (2.3.8)$$

Where  $\kappa$  denotes the volume viscosity,  $\eta$  is the shear viscosity. Eq. (2.3.6) is the conservation equation for fluid density, Eq. (2.3.7) and Eq. (2.3.8) are the conservation equations for the tangential and normal velocity components,  $\hat{u}$  and  $w$  respectively. The normal momentum equation (Eq. (2.3.8)) is decoupled from the remaining governing equations and is usually discarded, although it can be used to determine the pressure correction  $\hat{p}$ . Eq. (2.3.6) and Eq. (2.3.7) determine the normal velocity and tangential velocity respectively.

To simplify these equations, a set of auxiliary variables are used. The pressure curvature  $J$  is independent of time and can be specified through the strain rate:

$$\alpha = \sqrt{\frac{J}{\rho^{\text{in}}}} \quad (2.3.9)$$

where  $\rho^{\text{in}}$  is injected mixture density, which can be written as

$$\rho^{\text{in}} = \frac{p^{\text{in}} \bar{W}^{\text{in}}}{RT^{\text{in}}} \quad (2.3.10)$$

where  $p^{\text{in}}, \bar{W}^{\text{in}}$  and  $T^{\text{in}}$  are the gas pressure, molar mass and gas temperature of injected mixture, the values of these parameters are as same as that in the discharge.  $1/\bar{W}^{\text{in}} = \sum_{k \in C} Y_k^{\text{in}}/W_k$ , where the sum of inlet mass fractions of each species must be equal to 1,  $\sum_{k \in C} Y_k^{\text{in}} = 1$ .

Then, we introduce the auxiliary variables:

$$\begin{aligned} \tilde{u} &= \frac{\hat{u}}{\alpha} = \frac{u}{\alpha r} \\ \tilde{w} &= \rho w \end{aligned} \quad (2.3.11)$$

Finally, we have the equations for flow model:

$$\partial_t \rho + 2\rho \alpha \tilde{u} + \partial_z \tilde{w} = 0 \quad (2.3.12)$$

$$\rho \partial_t \tilde{u} + \tilde{w} \partial_z \tilde{u} = \alpha(\rho^{\text{in}} - \rho \tilde{u}^2) + \partial_z(\eta \partial_z \tilde{u}) \quad (2.3.13)$$

## 2.4 Conservation equations

Fluid models have been frequently used for low-temperature RF plasma discharges with a low degree of ionization ( $10^{-4} - 10^{-6}$ ) in gas mixtures such as  $\text{H}_2$  and  $\text{SiH}_4$ , and a pressure range from few tens of mTorr to few Torr<sup>12,13,14</sup>. The equations describing spatio-temporal evolution of the species mass fractions and electron temperature are as follows:

$$\partial_t(\rho Y_k) + \partial_z(\rho Y_k w + \rho Y_k V_k) = W_k \dot{\omega}_k, k \in C, \quad (2.4.1)$$

$$\partial_t \rho + 2\rho \alpha \tilde{u} + \partial_z \tilde{w} = 0 \quad (2.4.2)$$

$$\rho \partial_t \tilde{u} + \tilde{w} \partial_z \tilde{u} = \alpha(\rho^{\text{in}} - \rho \tilde{u}^2) + \partial_z(\eta \partial_z \tilde{u}) \quad (2.4.3)$$

$$\partial_t \left( \frac{3}{2} n_e k_B T_e \right) + \partial_z Q_e = n_e q_e V_e E + \dot{E}_{eh}. \quad (2.4.4)$$

$$\partial_z^2 \varphi = -\frac{nq}{\epsilon_0} \quad (2.4.5)$$

<sup>12</sup> D. B. Graves et al, *IEEE T. Plasma. Sci.*, 14(2): 78–91, 1986.

<sup>13</sup> J. P. Boeuf et al, *J. Appl. Phys.*, 71(10): 4751–54, 1992.

<sup>14</sup> K. De Bleecker et al, *IEEE T. Plasma. Sci.*, 32(2): 691–98, 2004.

Eq. (2.4.1) represents the continuity equations for each species. Here,  $\rho$  represents the mass density of the fluid mixture,  $w = \rho\tilde{w}$  is the normal macroscopic fluid velocity,  $u = r\alpha\tilde{u}$  is the tangential velocity,  $\alpha$  is the strain rate,  $\mathcal{C}$  is the set of chemical species considered (electrons, ions, radicals, and molecules),  $Y_k$  denotes the mass fraction of the  $k^{\text{th}}$  species,  $V_k$  denotes the drift-diffusion velocity of the  $k^{\text{th}}$  species.  $W_k$  is its molar mass, and  $\dot{\omega}_k$  is its molar production rate. Eq. (2.4.2) is the conservation equation for the fluid density, which determines the normal velocity  $w$  with units cm/s. Here,  $\alpha$  is the strain rate, which is defined as  $\alpha = \sqrt{\frac{J}{\rho^{in}}}$ , where  $J$  is the pressure curvature in tangential direction, which is a natural parameter of the laminar flow process that is generally independent of time, and  $\rho^{in}$  is the mass density of injected mixture. In our model,  $\alpha$  is a input parameter which one can vary over several simulations so as to obtain the desired inlet normal velocity in our study. Eq. (2.4.3) is the conservation equation for the tangential velocity  $u$  with units cm/s, and  $\tilde{u} = u/(\alpha r)$  where  $r$  is radius of electrodes.  $\eta$  is shear viscosity. Eq. (2.4.2) and Eq. (2.4.3) based on low Mach number scaling are called as flow model, taken from the references<sup>15,16</sup>. Eq. (2.4.4) is the second moment of the Boltzmann equation for the electron probability density function, which describes the energy balance for electrons. Here,  $T_e$  is the electron temperature,  $Q_e$  denotes the electron heat flux,  $n_e q_e V_e$  is the electron conduction current density, and  $\dot{E}_{eh}$  is the energy exchange rate between the electrons and heavy species due to inelastic collisions. Since heavy species temperature is assumed to be constant in the discharge, the equation for their energy is not resolved. The electric potential  $\varphi$  is obtained by solving Poisson's equation in Eq. (2.4.5), where  $n = \sum_{k \in \mathcal{C}} n_k$  is the mixture number density,  $q = \sum_{k \in \mathcal{C}} \frac{q_k n_k}{n}$  is the average charge of the mixture, and  $E = -\partial_z \varphi$  is the electric field. The magnetic field is negligible because the discharge dimensions are too small to allow the generation of magnetic waves. These fluid plasma equations are solved in a one-dimensional approximation to obtain the plasma macroscopic properties along the reactor axis. The thermodynamic

---

<sup>15</sup> J. M. Orlac'h, Modeling of a Silane-Hydrogen Plasma Discharge Including Nanoparticle Dynamics for Photovoltaic Applications. These de doctorat, Université Paris-Saclay, 2017.

<sup>16</sup> V. Giovangigli, *Science China Mathematics*, 55(2): 285–308,2012.

properties for neutral species are taken from the reference <sup>6</sup>.

## 2.5 Thermodynamic properties

In a SiH<sub>4</sub>-H<sub>2</sub> plasma, the perfect gas laws for each species are derived from kinetic theory<sup>2</sup>. For species  $k \in \mathcal{C}$ , it is written as

$$\rho_k = \frac{p_k W_k}{RT_k} \quad (2.5.1)$$

where  $T_k$  is the gas species temperature,  $W_k$  denotes the molar mass for species  $k$ .

For species  $k$ , the enthalpy  $h_k$  per unit mass is written as:

$$\rho_k h_k = \mathcal{E}_k + p_k \quad (2.5.2)$$

where  $\mathcal{E}_k$  is the species energy per unit volume,  $h_k$  denotes the enthalpy of the  $k^{\text{th}}$  species, which is defined as:

$$h_k = h_k^0 + \int_{T^0}^T c_{pk}(\tilde{T}) d\tilde{T}, k \in \mathcal{C}, \quad (2.5.3)$$

where  $h_k^0$  is standard enthalpy of formation for  $k^{\text{th}}$  species,  $T^0 = 273.15 \text{ K}$  is the standard temperature,  $c_{pk}$  is specific heat at constant pressure for the  $k^{\text{th}}$  species, which is written as

$$c_{pk} = c_{vk} + \frac{R}{W_k} \quad (2.5.4)$$

$c_{vk}$  is specific heat at constant volume of species  $k$ .

The specific entropy of the  $k^{\text{th}}$  species:

$$s_k = s_k^0 + \int_{T^0}^T \frac{c_{pk}(\tilde{T})}{\tilde{T}} d\tilde{T} - \frac{R}{W_k} \ln \left( \frac{p_k}{p^0} \right) \quad (2.5.5)$$

where  $s_k^0$  is the standard entropy of formation for  $k^{\text{th}}$  species,  $p^0$  is the standard atmospheric pressure,  $p_k = \rho_k RT / W_k$  is the partial pressure of  $k^{\text{th}}$  species. Eq. (2.5.5) also can be written as:

$$s_k = s_k^{\text{atm}} - \frac{R}{W_k} \ln \left( \frac{p_k}{p^0} \right) \quad (2.5.6)$$

where  $s_k^{\text{atm}}$  is the specific entropy at atmospheric pressure for  $k^{\text{th}}$  species, which is defined as

$$s_k^{\text{atm}} = s_k^0 + \int_{T^0}^T \frac{c_{pk}(\tilde{T})}{\tilde{T}} d\tilde{T} \quad (2.5.7)$$

For species  $k$ , the constant pressure specific heats  $c_{pk}(T)$ , the specific enthalpies

$h_k(T)$ , and the specific entropies at atmospheric pressure  $s_k^{\text{atm}}(T)$  have a following relation with their molar counterparts, written as:

$$C_{pk}(T) = W_k c_{pk}(T), H_k(T) = W_k h_k(T), S_k^{\text{atm}}(T) = W_k s_k^{\text{atm}}(T) \quad (2.5.8)$$

Generally, polynomial approximations are used to evaluate the thermodynamic properties of each species. Correspondingly, the absolute thermochemical data can be found in the NIST-JANAF thermochemical tables<sup>17</sup>. In our study, fourth-order NASA/SANDIA polynomials over two temperature intervals are applied. In this way, the molar species constant pressure specific heats can be written as:

$$\frac{c_{pk}(T)}{R} = \begin{cases} a_{1k} + a_{2k}T + a_{3k}T^2 + a_{4k}T^3 + a_{5k}T^4, & T_k^l \leq T \leq T_k^{\text{mid}} \\ a'_{1k} + a'_{2k}T + a'_{3k}T^2 + a'_{4k}T^3 + a'_{5k}T^4, & T_k^{\text{mid}} \leq T \leq T_k^u \end{cases} \quad (2.5.9)$$

where  $T_k^l$  is the lower bound of  $k^{\text{th}}$  species temperature,  $T_k^u$  is the upper bound of  $k^{\text{th}}$  species temperature, and  $T_k^{\text{mid}}$  is the intermediate temperature of  $k^{\text{th}}$  species. The two ranges of temperature are aimed to have a good precision for  $C_{pk}(T)$ . Correspondingly, the molar specific enthalpies and the molar specific entropies at atmospheric pressure for  $k^{\text{th}}$  species can be written as

$$\frac{H_k(T)}{RT} = \begin{cases} a_{1k} + \frac{a_{2k}T}{2} + \frac{a_{3k}T^2}{3} + \frac{a_{4k}T^3}{4} + \frac{a_{5k}T^4}{5} + \frac{a_{6k}}{T}, & T_k^l \leq T \leq T_k^{\text{mid}} \\ a'_{1k} + \frac{a'_{2k}T}{2} + \frac{a'_{3k}T^2}{3} + \frac{a'_{4k}T^3}{4} + \frac{a'_{5k}T^4}{5} + \frac{a'_{6k}}{T}, & T_k^{\text{mid}} \leq T \leq T_k^p \end{cases} \quad (2.5.10)$$

$$\frac{S_k^{\text{atm}}(T)}{R} = \begin{cases} a_{1k} \ln T + a_{2k}T + \frac{a_{3k}T^2}{2} + \frac{a_{4k}T^3}{3} + \frac{a_{5k}T^4}{4} + a_{7k}, & T_k^l \leq T \leq T_k^{\text{mid}} \\ a'_{1k} \ln T + a'_{2k}T + \frac{a'_{3k}T^2}{2} + \frac{a'_{4k}T^3}{3} + \frac{a'_{5k}T^4}{4} + a'_{7k}, & T_k^{\text{mid}} \leq T \leq T_k^p \end{cases} \quad (2.5.11)$$

where the coefficients  $a_{1k}$ ,  $a'_{1k}$  are correlated to  $H_k^0$ , and  $a_{7k}$ ,  $a'_{7k}$  to  $S_k^0$ . The polynomial expansion coefficients have been taken from the Chemkin Thermodynamic Database<sup>18</sup>.

## 2.6 Transport fluxes

The species drift-diffusion velocities appearing in Eq. (2.4.1) can be written as:

$$V_k = -D_k \frac{\partial_z Y_k}{Y_k} + \mu_k \vec{E} + \vec{V}_C, k \in C, \quad (2.6.1)$$

<sup>17</sup> P. J. Linstrom et al, *J. Chem. Eng. Data*, 46(5): 1059–63,2001.

<sup>18</sup> R. J. Kee et al, *The Chemkin Thermodynamic Data Base*, 1990.

where  $D_k$  is the diffusion coefficient and  $\mu_k$  is the mobility coefficient of the  $k^{\text{th}}$  species. Eq. (2.6.1) is a simplified version of the classical Hirschfelder and Curtiss<sup>19,20</sup> in a neutral gas mixture. For each species, the first term in Eq. (2.6.1) represents the diffusion velocity, and the second term is the drift velocity. For simplicity, we use  $\partial_x Y_k / Y_k$  instead of the term  $\partial_z X_k / X_k$ , where  $X_k = Y_k \bar{W} / W_k$  is the mole fraction of the  $k^{\text{th}}$  species.  $\bar{W}$  is the mean molar mass of gas mixture,  $W_k$  is the molar mass of  $k^{\text{th}}$  species. The spatial derivative of  $\bar{W}$  is neglected since it is small. It is well known that the simplified approximation introduced by Hirschfelder and Curtiss<sup>19,20</sup> can induce mass conservation problems, The solution to this problem is to add a correction velocity  $\vec{V}_c$  which ensures that  $\sum_{k \in C} \rho_k \vec{V}_k = 0$  is satisfied. The mass corrector diffusion velocity reads:  $\vec{V}_c = -\sum_{k \in C} (-D_k \nabla Y_k + \mu_k Y_k \vec{E}) / \sum_{k \in C} Y_k$ , which is referred from Stefan-Maxwell relations<sup>21</sup>.

The electron heat flux reads<sup>15</sup>

$$Q_e = \frac{5}{2} n_e k_B T_e V_e - \lambda_e \partial_x T_e, \quad (2.6.2)$$

where  $\lambda_e$  is the electron thermal conductivity. The first term represents the transport of electron energy through diffusion, the second term is electron heat conduction. The Dufour and Soret effects<sup>22</sup> are negligible in our conditions.

## 2.7 Transport coefficients

The diffusion coefficients  $D_k, k \in C$ , are written as<sup>7,25</sup>:

$$D_k = \frac{p(1-Y_k)}{\sum_{l \in N, l \neq k} p_l / D_{k,l}^{bin}}, k \in C, \quad (2.7.1)$$

where  $p$  is the pressure of the gas mixture,  $p_l$  is the partial pressure of  $l^{\text{th}}$  species.  $D_{k,l}^{bin}$  is the binary diffusion coefficient for the species pair  $(k, l)$ , and  $N \subset C$  denotes the set of neutral species. For neutral species, we use Lennard-Jones potentials to

<sup>19</sup> J. O. Hirschfelder et al, *Symposium on Combustion and Flame, and Explosion Phenomena*, 3(1): 121–27,1948.

<sup>20</sup> E. S. Oran et al, *Prog. Energy Combust. Sci.*, 7(1): 1–72, 1981.

<sup>21</sup> V. Giovangigli, *Comput. Sci. Eng.*, 3(3): 244–76, 1991.

<sup>22</sup> R. G. Mortimer et al, *Proc. Natl. Acad. Sci. U.S.A.*, 77(4):1728–31,1980.

calculate  $D_{k,l}^{bin}$ . EGLIB software<sup>23</sup> is employed to calculate transport coefficients. Collision integrals are computed using the ‘TRANFT’ fitting program<sup>24</sup>.

For charged species, since their densities are much smaller than neutrals (weakly ionized plasma,  $Y_k \ll 1$ ), we consider that the charged species diffuse against  $H_2$  and  $SiH_4$  only. For the electron collisions, we use BOLSIG+ software<sup>25</sup> to obtain  $D_e$  and  $\mu_e$ , using as input cross-sections data of electron-collision reactions listed in relevant literature and process conditions (gas temperature, gas composition, *etc*) used in our study. As the composition (% $SiH_4$ , % $H_2$ ) does not change significantly in the discharge, we could run Bolsig offline before the calculations for a given silane mole fraction, and thus tabulate the values of electrons transport coefficients as a function of electron temperature only. Figure 2.2 shows the electron diffusion coefficient and mobility as a function of electron temperature for different silane concentration. Figure 2.2 (a) shows that electron diffusion coefficient increases with the increase of silane concentration at the range of electron temperature below 6 eV, while the electron diffusion coefficient decreases with increase of silane concentration above 6 eV. Figure 2.2 (b) shows that the electron mobility increases as increasing silane concentration when electron temperature is below 5 eV. The inset of Figure 2.2 (b) shows that electron mobility decreases as increasing silane concentration.

The binary diffusion coefficients of ions against neutral molecules are computed according to Langevin theory<sup>8</sup>:

$$D_{ij}^{bin}p = 5.2 \times 10^{-3} \frac{k_B T_h}{|q_i|} \frac{T}{\sqrt{\delta_j m_{ij}}} \text{ cm}^2 \text{ s}^{-1} \text{ torr} \quad (2.7.2)$$

where  $p$  is the pressure,  $k_B$  is the Boltzmann constant,  $T$  is the gas temperature,  $q_i$  is the charge of the  $i^{\text{th}}$  species,  $m_{ij}$  is the reduced mass in the atomic mass unit ( $m_{ij} = m_i m_j / (m_i + m_j)$ ), and  $\delta_j$  is the polarizability of gas molecule<sup>30</sup>:

$$\delta_{H_2} = 0.805 \text{ \AA}^3, \quad \delta_{SiH_4} = 4.62 \text{ \AA}^3 \quad (2.7.3)$$

<sup>23</sup> V. Giovangigli, EGLIB, 2021.

<sup>24</sup> R. J. Kee et al, A Fortran computer code package for the evaluation of gas-phase multicomponent transport properties, *Sandia National Laboratories Report SAND86-8246, 13*, 80401-1887.

<sup>25</sup> G. J. M. Hagelaar et al, Updates on the Freeware Electron Boltzmann Equation Solver BOLSIG +, 2013.

For the binary mobility coefficients of ions, we use Einstein relation:

$$\mu_{ij} = \frac{q_i D_{ij}}{k_B T} \quad (2.7.4)$$

The mobility of species  $i$  is calculated from the mobility  $\mu_{ij}$  in each gas  $j$  through the expression:

$$\frac{1}{\mu_i} = \sum_j \frac{P_j/P}{\mu_{ij}} \quad (2.7.5)$$

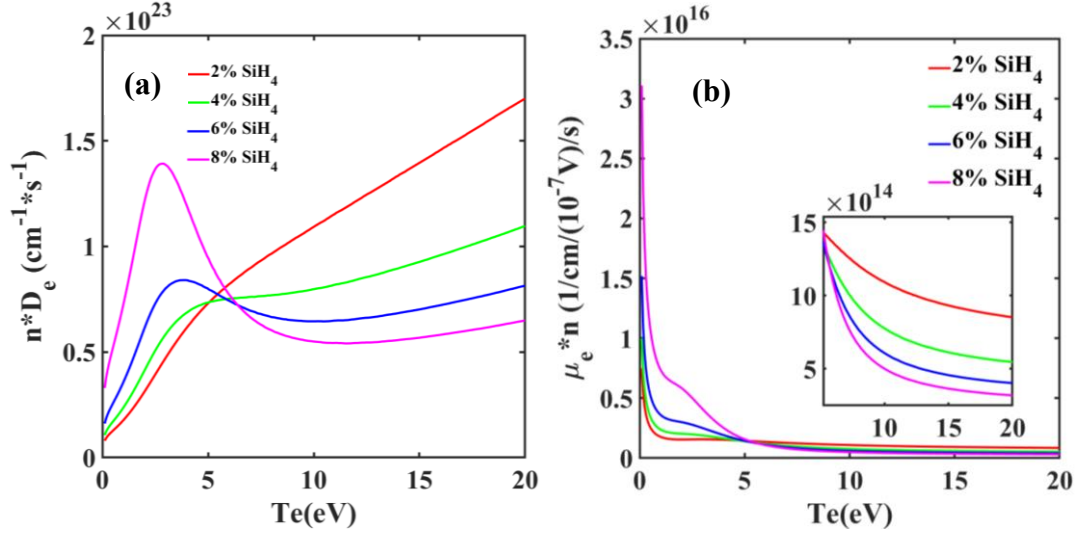


**Figure 2.2** (a) electron diffusion coefficient as a function of electron temperature for the range of silane concentration from 2% to 8%. (b) electron mobility as a function of electron temperature for the range of silane concentration from 2% to 8%.

## 2.8 $\text{SiH}_4$ - $\text{H}_2$ plasma chemistry

Our plasma chemistry model takes into account 19 species listed in Table 1, including species with Si that contain up to 2 silicon atoms since species with the number of silicon more than 2 are taken as nucleation of nanoparticles. The model calculates each species' density and flux along the reactor axis towards the electrodes.

Table 1. Species included in the fluid model

Neutral species	$\text{H}_2$ , $\text{SiH}_4$ , $\text{H}$ , $\text{SiH}_3$ , $\text{SiH}_2$ , $\text{H}_3\text{SiSiH}$ , $\text{Si}_2\text{H}_5$ , $\text{Si}_2\text{H}_6$
Charged species	$\text{SiH}_3^+$ , $\text{SiH}_2^+$ , $\text{Si}_2\text{H}_4^+$ , $\text{H}_3^+$ , $\text{H}_2^+$ , $\text{H}^+$ , $e$ , $\text{SiH}_2^-$ , $\text{SiH}_3^-$ , $\text{Si}_2\text{H}_5^-$ , $\text{H}_3\text{SiSiH}^-$

The gas phase chemistry model includes two types of reactions: the electron

collision reactions and the heavy-species reactions. In our model, we consider 24 electron collision reactions (Annex I) and 19 heavy-species reactions (Annex II). The electron collisions in Annex I include ionization, dissociative attachment, dissociation, detachment and recombination reactions. In the moderate pressure regime (1-2 Torr), the dissociative attachment reactions are important because these reactions form negative ions and then lead to cluster formation. The vibrational excited silane and hydrogen molecules are not considered since the vibrational effects are low in the range of temperatures (about 450 K) applied for the deposition of silicon thin films<sup>26</sup>. The ionization reactions produce positive ions which are accelerated in the plasma sheaths and contribute to deposition or etching. Dissociation reactions are essential in the discharge, radicals produced from these reactions are the main precursors to the silicon thin film deposition. Heavy species reactions in Annex II consist of neutral-neutral reactions, neutralization reactions, hydrogen ions reactions and cluster growth reactions. The cluster growth reactions contribute to the nucleation of nanoparticles; thus, they are very important for the formation of nanoparticles.

The chemistry mechanism consists of a group of  $R$  reactions, in the form



where  $M_k$  represents the chemical symbol of the  $k^{\text{th}}$  species,  $\nu_k^{rf}$  and  $\nu_k^{rb}$  are the forward and backward stoichiometric coefficients of  $k^{\text{th}}$  species in reaction  $r$  respectively. For each species, the molar production rate can be calculated from contributions of each reaction  $r$  in the form:

$$\dot{\omega}_k = \sum_{r \in \mathcal{R}} (\nu_k^{rf} - \nu_k^{rb}) \dot{\tau}_r \quad (2.8.2)$$

in which  $\dot{\tau}_r$  denotes the rate of progress for the  $r^{\text{th}}$  reaction.

The rate of progress  $\dot{\tau}_r$  is written as:

$$\dot{\tau}_r = \mathcal{K}_r^f \prod_{k \in \mathcal{C}} \gamma_k^{\nu_k^{rf}} - \mathcal{K}_r^b \prod_{k \in \mathcal{C}} \gamma_k^{\nu_k^{rb}} \quad (2.8.3)$$

where  $\mathcal{K}_r^f$  and  $\mathcal{K}_r^b$  denote the forward and backward rate constants of the  $r^{\text{th}}$  reaction, respectively, and  $\gamma_k = \rho \frac{Y_k}{m_k}$  is the molar concentration of the  $k^{\text{th}}$  species.

---

<sup>26</sup> K. D. Bleecker et al, *Phys. Rev. E*, 70(5):056407,2004.

In our model, electron collision reactions are irreversible, and depend on electron temperature  $T_e$ . Heavy species reactions consist of irreversible and reversible reactions, which depend on heavy species temperature  $T$ . For heavy species reactions, the relation between  $\mathcal{K}_r^f$  and  $\mathcal{K}_r^b$  is in the form:

$$\mathcal{K}^e(T_h) = \frac{\mathcal{K}_r^f(T)}{\mathcal{K}_r^b(T)} \quad (2.8.4)$$

where  $\mathcal{K}_r^e$  is the equilibrium constants of the  $r^{\text{th}}$  reaction in the form<sup>27</sup>:

$$\ln \mathcal{K}_{rh}^e(T_h) = - \sum_{k \in C} \frac{v_k^r m_k}{RT_h} \left( g_k^{\text{atm}}(T) - \frac{RT_h}{m_k} \ln \left( \frac{p^{\text{atm}}}{RT} \right) \right) \quad (2.8.5)$$

where  $g_k^{\text{atm}}$  is the specific Gibbs free energy function at atmospheric pressure for the  $k^{\text{th}}$  species, which is written as:

$$g_k^{\text{atm}}(T) = h_k(T) - T_h s_k^{\text{atm}}(T), k \in \mathcal{S} \quad (2.8.6)$$

For electron collisions, the equilibrium constant  $\mathcal{K}_{re}^e$  is non-defined, since  $T \neq T_e$ . Whereas, in some cases, the equilibrium constant might depend on either the electron temperature  $T_e$  or heavy species temperature  $T$  based on the form of the reaction considered. For example, an electron impact ionization has the form



where  $M_e$ ,  $M_n$ , and  $M_i$  represent the chemical symbols of electron, neutral species and positive ions respectively. The equilibrium constant is referred to as the ‘Saha’ equation<sup>28</sup>, and reads:

$$\mathcal{K}_{re}^e = \left( \frac{m_i}{m_n} \right)^{\frac{3}{2}} \left( \frac{2\pi m_e k_B T_e}{h_p^2} \right)^{\frac{3}{2}} \exp \left( - \frac{\Delta \mathcal{E}_{\text{ioniz}}}{k_B T_e} \right) \quad (2.8.8)$$

where  $\Delta \mathcal{E}_{\text{ioniz}}$  is the ionization energy of reaction (2.8.7). In Eq. (2.8.8), the first two factors correspond to the translational partition functions, and the term in the exponential factor is the ionization energy divided by the electron temperature. In fact, the electrons as reactant provide the required energy for the ionization<sup>32</sup>. The Eq. (2.8.8) can also be deduced from non-equilibrium thermodynamics<sup>29,30</sup>.

<sup>27</sup> Tolman, The Principles of Statistical Mechanics, Dover Publications, 2021.

<sup>28</sup> B. Graille et al, Modeling of Reactive Plasmas for Atmospheric Entry Flows Based on Kinetic Theory, Proceedings of the Summer Program, 2008.

<sup>29</sup> M. C. M. van de Sanden et al, Phys. Rev. A, 40(9): 5273–76, 1989.

<sup>30</sup> D. Giordano et al, Phys. Rev. E, 65(1):016401, 2001.

In general, the forward rate constant of all reactions listed in Annex I and II are in a generalized Arrhenius empirical relation, of the form,

$$K_r^f(T_r) = A_r T_r^{\beta_r} \exp\left(-\frac{\mathfrak{E}_r}{RT_r}\right) \quad (2.8.9)$$

where  $T_r$  is the temperature of the  $r^{\text{th}}$  reaction, namely  $T_r = T$  for heavy-species reactions and  $T_r = T_e$  for electron collision reactions,  $A_r$  is the pre-exponential factor,  $\beta_r$  is the exponent of temperature and  $\mathfrak{E}_r > 0$  is the activation energy of the  $r^{\text{th}}$  reaction. In the model, electron collision reactions are assumed irreversible. For heavy species reactions, the backward rate constant is derived from the forward rate constant and the equilibrium constant, namely the Eq. (2.8.4) and Eq. (2.8.5).

## 2.9 Energy exchange term

In general, the energy exchange occurs during elastic scattering of electrons against heavy species and reactive electron collisions. The energy exchange term  $\dot{E}_{eh} = -\dot{E}_{he}$  can be expressed as<sup>2</sup>:

$$\dot{E}_{eh} = \dot{E}_{eh}^{el} + \dot{E}_{eh}^{chem} \quad (2.9.1)$$

where  $\dot{E}_{eh}^{el}$  represents the energy exchange term because of elastic collisions of electrons against heavy species, and  $\dot{E}_{eh}^{chem}$  represents the reactive electron collisions.

In general, the elastic term is often written in the form<sup>31</sup>

$$\dot{E}_{eh}^{el} = \dot{E}_{eh}^{0,el} = -\frac{3}{2} n_h k_B (T_e - T) \frac{1}{\tau^{el}} \quad (2.9.2)$$

where  $\tau^{el}$  represents the characteristic time of electron collisions. The energy loss to electron collisions is negligible<sup>32</sup>. The energy exchange term due to electron collisions can be written as:

$$\dot{E}_{eh}^{chem} = \sum_{r \in \mathcal{R}_e} \Delta \mathcal{E}_{er} \dot{\tau}_r \quad (2.9.3)$$

where  $\Delta \mathcal{E}_{er}$  represents the net average energy gained by electrons in the  $r^{\text{th}}$  electron collision reaction.  $\mathcal{R}_e$  is the set of electron collision reactions,  $\dot{\tau}_r$  is the rate of progress for the  $r^{\text{th}}$  electron collision. For each electron collision reaction in Annex I,  $\Delta \mathcal{E}_{er}$  is listed in the Annex III.

<sup>31</sup> D. P. Lymberopoulos et al, *J. Res. Natl. Inst. Stand. Technol.*,100(4):473–94,1995.

<sup>32</sup> D. P. Lymberopoulos et al, *J. Appl. Phys.*,73(8):3668–79,1993.

## 2.10 Boundary conditions

The electrical potential is set to zero at the grounded electrode, while a sine waveform is applied at the powered electrode. It has been checked that, for the process conditions studied in this work, the experimental value of the DC self-bias at the powered electrode has negligible effects on the deposition rate in the model. Therefore, we have applied a sine waveform to the powered electrode without DC self-bias in the model. The dissipated power  $P$  in the discharge is calculated as follows:

$$P = \frac{1}{T} \int_t^{T+t} I_{RF}(t) \cdot \varphi_L(t) dt \quad (2.10.1)$$

Here  $\varphi_L(t)$  is the potential at the driven electrode,  $I_{RF}(t)$  is the electric current, and  $T$  is a period of the RF cycle. The detailed solution for  $\varphi_L(t)$  and  $I_{RF}(t)$  is described in the reference<sup>1</sup>. In this case, one can adjust applied voltage to get the selected value of dissipated power. The boundary conditions for the electron temperature and the electron energy flux are also taken from reference<sup>1</sup>.

The boundary condition for normal velocity  $\tilde{w}$  and tangential velocity  $\tilde{u}$  are written as<sup>11,15</sup>:

$$(\rho\tilde{w})|_{t,z=0} = 0, \quad (\rho\tilde{w})|_{t,z=L} = \rho\tilde{w}^{in} \quad (2.10.2)$$

$$\tilde{u}|_{t,z=0} = 0, \quad \tilde{u}|_{t,z=L} = 0 \quad (2.10.3)$$

Here one can adjust the strain rate  $\alpha$  to obtain the desired inlet normal velocity  $\tilde{w}^{in}$ . Since negative ions are trapped in the plasma, their densities are set to zero at both boundaries. On the contrary, positive ions are accelerated through the plasma sheaths, eventually contributing to surface processes. Neutral species also contribute to surface processes. Finally, the boundary conditions for neutrals, ions and electrons are detailed below.

The outward mass flux for each species (electron, neutral, or positive ion) is computed as:

$$F_k|_{out} = \rho Y_k \max[\vec{V}_k^{drift} \cdot \vec{n}, V_{k+}], \quad k \in P \cup N \cup \{e\}, \quad (2.10.4)$$

where  $\vec{V}_k^{drift}$  is the drift velocity of the  $k$ th species, which reads (note that the mobilities of neutral species are simply equal to zero):

$$\vec{V}_k^{drift} = \mu_k \vec{E}, \quad k \in C, \quad (2.10.5)$$

and  $V_{k+}$  is the average thermal velocity of  $k^{\text{th}}$  species towards electrodes computed as that of a Maxwellian distribution function, that is<sup>21</sup>

$$V_{k+} = \frac{1}{2} v_k^{th} = \left( \frac{8RT_k}{\pi W_k} \right)^{\frac{1}{2}}, \quad k \in C \quad (2.10.6)$$

The physical meaning behind Eq. (2.10.4) is: when the outwards drift velocity  $\vec{V}_k^{drift}$  is larger than the thermal velocity  $v_k^{th}$ , the outward flux at the boundary is merely equal to the drift flux, however, when the drift velocity is smaller or oriented inwards, the diffusion velocity at the electrode is merely equal to the thermal velocity. Eq. (2.10.4) guarantees that the flux of positive ions is always pointing outwards the reactor. Note that for neutral species the outward flux is simply the thermal flux.

### 2.10.1 Boundary conditions for nonnegative species

We first detail the boundary conditions for nonnegative species (i.e. ions and neutral). For all nonnegative species, the boundary conditions at both electrodes are written as:

$$(\rho Y_k (\vec{V}_k + w) \cdot \vec{n})|_{t,z=0,L} = W_k \dot{\omega}_k, \quad k \in N \cup P, \quad (2.10.7)$$

where  $P$  represents the set of positive ions,  $N$  represents the set of neutral species,  $\vec{n}$  is the unit vector normal to the electrodes pointing outwards from the reactor,  $\dot{\omega}_k$  is the net molar surface loss rate of the  $k^{\text{th}}$  species, which is calculated from the surface reaction rates of progress  $\dot{\tau}_r$ ,  $r \in \hat{R}$ , as:

$$\dot{\omega}_k = \sum_{r \in \hat{R}} (v_k^{rf} - v_k^{rb}) \dot{\tau}_r, \quad k \in N \cup P. \quad (2.10.8)$$

where  $\hat{R}$  denotes the set of surface species reactions, and  $v_k^{rf}$  and  $v_k^{rb}$  denote the forward and backward stoichiometric coefficients of the  $k^{\text{th}}$  species in the  $r^{\text{th}}$  surface reaction, respectively. Each surface reaction  $r \in \hat{R}$  is associated with a unique gas-phase impinging species  $k(r)$ , which may be an ion, a neutral species or an electron. For example, to compute the net molar surface loss rate of  $\text{SiH}_3$ , one should consider the reactions RS7, RS8 and RS9 in the Annex IV. Each of these reaction rates of progress  $\dot{\tau}_r$  should be calculated, the detailed formula for  $\dot{\tau}_r$  will be discussed below.

Also it is clearly shown that the forward and backward stoichiometric coefficients ( $v_{SiH_3}^{rf}$  and  $v_{SiH_3}^{rb}$ ) for  $SiH_3$  in RS7, RS8 and RS9 are 1 and 0, respectively.

The reaction rate of progress  $\dot{\tau}_r$  is computed from the outward mass flux  $F_{k(r)}|_{out}$  of species  $k(r)$  as follows:

$$\dot{\tau}_r = \frac{p_r}{1 - \frac{l_{k(r)}}{2}} \cdot \frac{F_{k(r)}|_{out}}{W_{k(r)} v_{k(r)}^{rf}}, r \in \hat{R} \quad (2.10.9)$$

where  $p_r$  is the probability of reaction  $r$ .  $l_k$  is the loss probability of the  $k^{\text{th}}$  impinging species: in particular  $l_k = 0$  if the impinging species is specularly reflected at the wall, and  $l_k = 1$  if the impinging species is completely lost due to either sticking, recombination or etching reaction. The description of these two parameters ( $p_r$  and  $l_k$ ) will be detailed below.

For silane/hydrogen plasma discharges, the surface processes consist of reflection, sticking, recombination, and etching reactions, as shown in Figure 2.3. When a species reaches the substrate, there is a certain probability for each type of surface reaction to occur.

For each species  $k \in N \cup P$  impinging on the surface, three kinds of reactions may occur, namely sticking, recombination or etching. For sticking, it means that the gaseous species  $SiH_x$  (g) sticks to the surface and contributes to the film growth. The etching reactions take Si atoms away from surface, resulting in the formation of

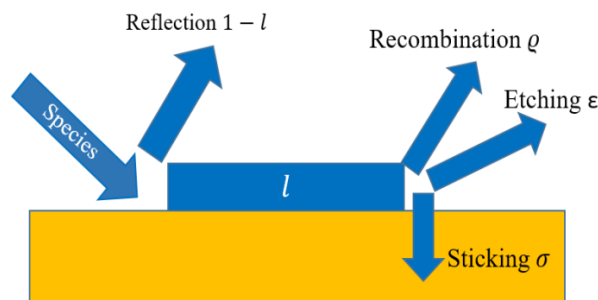


**Figure 2.3** Schematic representation of the surface processes in silane/hydrogen plasma.

$SiH_x$  (g), while recombination reactions do not take silicon atoms from surface, it means gas species recombines and go back to the discharge, for example,  $H + wall = 0.5H_2$  (g) is a recombination reaction. For a given impinging species  $k$ , the sum of the

probabilities of all reactions is always equal to the loss probability  $l_k$ , the remainder of the molecules being specularly reflected with probability  $1 - l_k$ . In other words:

$$0 \leq l_k = \sigma_k + \varrho_k + \varepsilon_k \leq 1 \quad (2.10.10)$$

where  $l_k$  is the loss probability, and where  $\sigma_k$ ,  $\varrho_k$  and  $\varepsilon_k$  are the sticking, recombination and etching probabilities, respectively.

The rate of progress of reaction  $r \in \hat{R}$  (which is either a sticking, a recombination or an etching reaction) is rewritten as:

$$\dot{t}_r = \frac{p_r}{1 - \frac{l_k}{2}} \cdot \frac{F_k l_{out}}{W_k v_k^{TF}}, r \in \hat{R} \quad (2.10.11)$$

where  $p_r$  is the probability of reaction  $r$ , that is  $p_r = \sigma_k$  if  $r$  is a sticking reaction,  $p_r = \varrho_k$  if  $r$  is a recombination reaction, and  $p_r = \varepsilon_k$  if  $r$  is an etching reaction. The denominator  $1 - \frac{l_k}{2}$  is here to ensure validity in the limit  $l_k \rightarrow 1$ , where nearly all the molecules of species  $k$  are lost at the wall and no molecules are secularly reflected, in which case the distribution function of the  $k^{\text{th}}$  species close to the wall is strongly anisotropic<sup>33,34,35</sup>. It is worth mentioning that for positive ions the loss probability is always 1.0 in our model.

### Examples:

In order to explain how the surface processes are modelled, we take SiH<sub>4</sub> as an example. SiH<sub>4</sub> can stick to the substrate as a reactant and can be a product coming back to the gas discharge. SiH<sub>4</sub> molecules as reactant species stick to the surface and contribute to deposition, SiH<sub>4</sub>(g)+wall=Si(s)+2H<sub>2</sub>(g), see RS10 in Annex IV. SiH<sub>4</sub> molecules as product species come back to the discharge, for example, 4H + Si-wall = SiH<sub>4</sub>(g), see RS2 in Annex IV. In our model,  $p_r = \sigma_{\text{SiH}_4}$  in Eq. (2.10.10) when calculating the rate of progress for RS10 in Annex IV, correspondingly  $l_{\text{SiH}_4} = \sigma_{\text{SiH}_4}$  because there are no etching and recombination reactions considered for SiH<sub>4</sub>. For 4H + Si-wall = SiH<sub>4</sub>(g) (RS2 in Annex IV),  $p_r = \varepsilon_H$  and  $l_H = \varrho_H + \varepsilon_H$  are considered in order to calculate the rate of progress. When computing net molar surface loss rate for

<sup>33</sup> C. R. Kleijn, *Thin Solid Films*, 365(2): 294–306, 2000.

<sup>34</sup> R. J. Kee et al, *Chemically Reacting Flow: Theory and Practice*, John Wiley & Sons, 2005.

<sup>35</sup> H. Motz et al, *J. Chem. Phys.*, 32(6):1893–94, 1960.

SiH<sub>4</sub> ( $\dot{\omega}_{SiH_4}$ ) in Eq.(2.10.8) ( $\dot{\omega}_k = \sum_{r \in \hat{R}} (v_k^{rf} - v_k^{rb}) \dot{t}_r$ ,  $k \in N \cup P$ .), one should consider all of surface reactions related to SiH<sub>4</sub>. In this case, RS2-RS5, RS9, RS10 in Annex IV should be taken into account. For the sake of clarity, we only take RS2 and RS10 in Annex IV as an example to calculate  $\dot{\omega}_{SiH_4}$ , which is sum of the rate of progress  $\dot{t}_r$  multiplied by stoichiometric coefficients for both reactions. In detail, for RS10 in Annex IV,  $v_{SiH_4}^{rf} = 1$  and  $v_{SiH_4}^{rb} = 0$ ; for RS2 in Annex IV,  $v_{SiH_4}^{rf} = 0$  and  $v_{SiH_4}^{rb} = 1$ . Then one can understand how all surface reactions are calculated in our model.

### 2.10.2 Boundary conditions for electrons

The secondary electron emission induced by positive ions bombardment under PECVD conditions in silane/hydrogen discharge is considered. The coefficient is taken as  $\gamma_e = 0.1$ <sup>36</sup>. The boundary conditions for electrons thus read:

$$(\rho Y_e (\vec{V}_e + \vec{w}) \cdot \vec{n})|_{t,z=0,L} = F_e|_{out} - W_e \sum_{k \in P} \gamma_e \frac{F_k|_{out}}{W_k} \quad (2.10.12)$$

where  $\gamma_e$  is the secondary electron emission coefficient.

### 2.10.3 Boundary conditions for electron temperature

$$(Q_e \cdot \vec{n})|_{t,z=0,L} = h_e F_e|_{out} - n_e \mathcal{E}^{sem} \sum_{k \in P} \gamma_e \frac{F_k|_{out}}{W_k} \quad (2.10.13)$$

where  $h_e$  is specific enthalpy  $\mathcal{E}^{sem}$  is the specific energy of secondary electrons, which can be expressed in terms of the ionization energy  $\mathcal{E}^{ioniz}$  and the work function of the electrode  $\mathcal{W}$ :  $\mathcal{E}^{sem} = \mathcal{E}^{ioniz} - 2\mathcal{W}$

### 2.10.4 Deposition rate

The deposition rate of silicon thin film associated with each surface reaction  $r$  then follows

$$v_{Si(s)}^r = V_m^{Si} v_{Si(s)}^{rb} \dot{t}_r > 0, \quad (2.10.14)$$

where  $v_{Si(s)}^{rb}$  is the backward stoichiometric coefficient of Si(s) in the  $r^{\text{th}}$  surface reaction, and  $V_m^{Si}$  is the molar volume of crystalline silicon

<sup>36</sup> P. Diomedee et al., *J. Phys. D: Appl. Phys.*, 45(17): 175204, 2012.

$$V_m^{\text{Si}} \cong 12.06 \text{ cm}^3 \cdot \text{mol}^{-1} ,$$

The etching rate of silicon thin film associated with each surface reaction  $r$  reads similarly

$$v_{\text{Si}(s)}^r = -V_m^{\text{Si}} \nu_{\text{Si}(s)}^{rf} \dot{\tau}_r < 0,$$

and, consequently, the net deposition rate of silicon thin film reads

$$v_{\text{Si}(s)} = \sum_{r \in \hat{R}} v_{\text{Si}(s)}^r. \quad (2.10.15)$$

The list of surface reactions and the corresponding probabilities are given in the Annex IV.

## 2.11 Numerical implementation

The spatial discretization of the Equations (2.4.1)-(2.4.5) is obtained by applying a three-point finite difference scheme. The drift-diffusion equations for species mass fractions and electron temperature are dealt with Scharfetter-Gummel discretization scheme<sup>37,38</sup>. The time derivatives of Equations (2.4.1) and (2.4.4) are discretized in a fully implicit manner and solved by Newton method using a Euler predictor<sup>39</sup>.

In our simulations, the RF frequency is 13.56 MHz. Reaching the steady-state for silane/hydrogen plasmas requires the calculation of about 40000 RF cycles, and each RF cycle is resolved with a time step of  $2.5 \times 10^{-10}$  s. Typical calculation time for 40000 RF cycles is about two weeks on our PC (Intel(R) Xeon(R) Silver 4214 CPU @ 2.2GHz, RAM: 64GB). The criterion of convergence for the deposition rate in the model is indicated by

$$\left| \frac{v_{\text{Si}(s)}^{\text{ncyc}+100} - v_{\text{Si}(s)}^{\text{ncyc}}}{100} \right| \ll 1 \times 10^{-5} \quad (2.11.1)$$

where ncyc is the number of RF cycles.

## 2.12 Results and discussion

The schematic diagram of RF CCP reactor is presented in the Figure 2.1. The

<sup>37</sup> A. Haji-Sheikh et al, Series in Computational Methods and Physical Processes in Mechanics and Thermal Sciences, *CRC Press*,2021.

<sup>38</sup> E. Süli, An Introduction to Numerical Analysis, *Wiley*,2021.

<sup>39</sup> D. L. Scharfetter et al, *IEEE T. Electron Dev.*16(1):64–77,1969.

reactor is generally composed of two electrodes, one electrode is grounded and the other is driven by RF a voltage signal with frequency of 13.56 MHz, which is supplied by a generator. A matchbox is required to make sure the coupling of power between generator and reactor, but the diagram does not show for simplicity. The power dissipated to the reactor is used to ionize, dissociate or excite the gas, thus the plasma is ignited. In the mid of reactor, the plasma potential is nearly constant, while close to the walls there is a region called plasma sheath where the potential drop accelerates positive ions. Figure 2.4 shows the picture of ARCAM reactor which is used in LPICM for many years<sup>10</sup>. This reactor is geometrically asymmetric because the driven electrode is smaller than grounded electrode, which causes the asymmetric current flow in the discharge and turns out the negative DC bias at the powered electrode.



**Figure 2.4** Picture of the ARCAM reactor locate at LPICM<sup>10</sup>.

The following process conditions are used to study silane-hydrogen plasma: gas/substrate temperature is fixed at 448K, the gas pressure is 1 Torr, the applied potential is 200 V, the inter-electrode distance is 1.6 cm, the silane mass concentration is  $(\text{SiH}_4/(\text{SiH}_4+\text{H}_2))$  1.4%. For all of figures,  $Z=0$  cm points to grounded substrate, while  $Z=1.6$  cm corresponds to the electrically driven electrode. The steady state electrical potential, electric field, electron temperature and electron density along the reactor in a RF cycle are presented in Figure 2.5. In particular, Figure 2.5(a) shows the

spatiotemporal evolution of the electric potential between the powered electrode and the grounded electrode, and the time axis spans one RF cycle. As the figure shows, at the powered electrode, the electric potential evolution follows a sinusoid since this is imposed by the RF generator. Also, at the grounded electrode, the potential equal to zero. In the plasma bulk, the potential is always larger than the potential at the both electrodes.

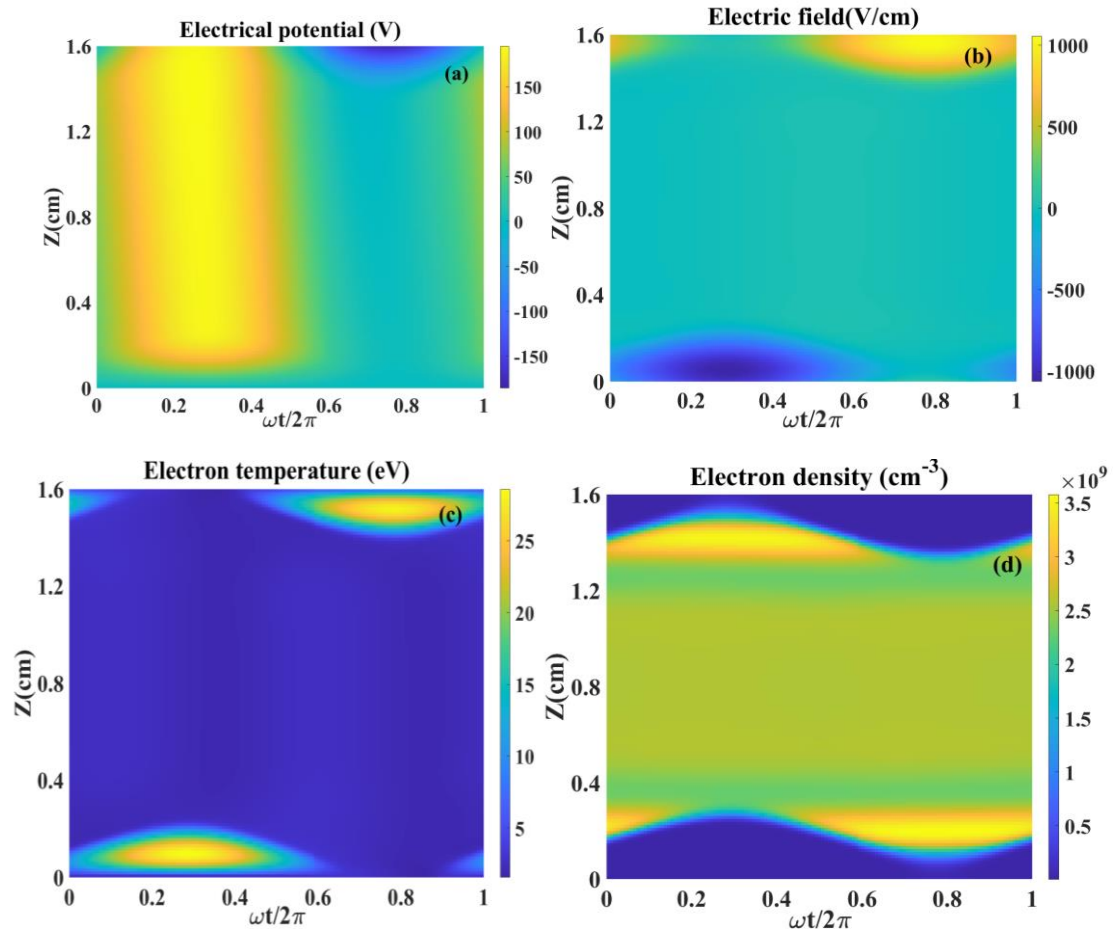


**Figure 2.5** Steady-state electric potential (a), electric field (b), electron temperature (c) and electron density (d) profile between the two electrodes during one RF cycle. The horizontal axis represents the time during one RF cycle, and the normal axis indicates the location along the reactor where  $Z = 0$  cm points to grounded electrode and  $Z = 1.6$  cm points to driven electrode. The gas pressure is fixed at 1Torr, gas temperature is 448 K, the applied potential at RF electrode is 200 V, silane mass concentration is 1.4%, and hydrogen mass concentration is at 98.6%.

Under specific conditions<sup>40,41</sup>, field reversal may occur if the potential in the plasma bulk is lower than the potential of one electrode, and electrons would be attracted and

<sup>40</sup> O. Leroy et al, *J. Phys. D: Appl. Phys.*, 28(3): 500,1995.

<sup>41</sup> A. Salabas et al, *J. Appl. Phys.*,95(9):4605–20,2004.

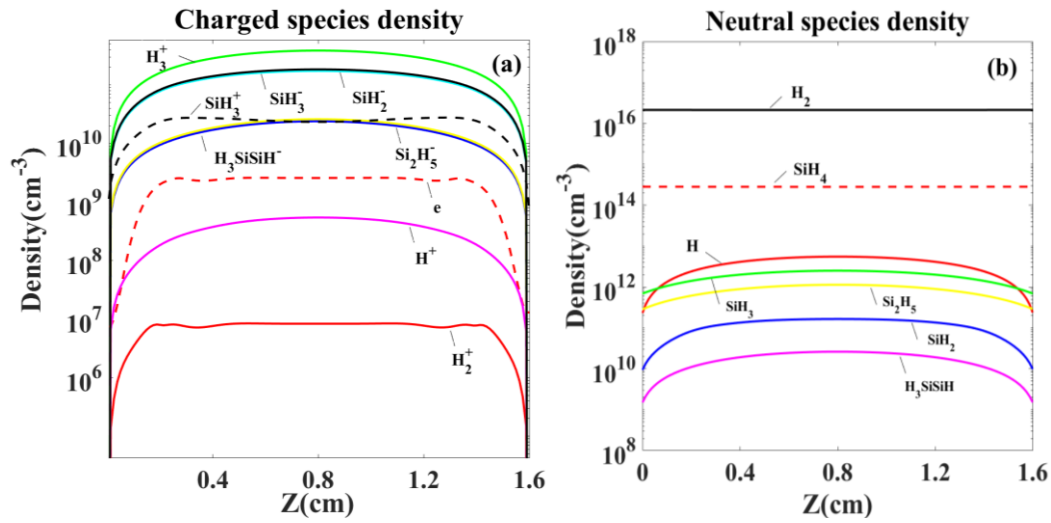
lost to the wall very rapidly. Figure 2.5(b) shows the time evolution of electric field over one RF period in the reactor. As one can see, in the plasma bulk the electric field is nearly zero due to the nearly constant electric potential. In the sheath regions, the electric field oscillates as a sinusoid. Figure 2.5(c) shows the evolution of electron temperature across the discharge. As one can see, the electron temperature is not larger than 5 eV in the plasma bulk. For the sheath regions, the electron temperature can be larger than 20 eV when the sheaths expand, while the electron temperature is about 5 eV when the sheath width reaches its minimum. The reason why the electron temperature is increased at large sheath width is that the positive ions bombard the electrode with large fluxes, which induces secondary electrons accelerating in the sheaths. As Figure 2.5(d) shows, the electron density has a magnitude of  $10^9$ , which is relatively low compared to electropositive gas discharge. This is because negative ions are formed from electron dissociative attachment reactions in silane discharges. Also, most electrons are constrained in the plasma bulk. In particular, one can see that the electron density is larger at the time when the sheaths contract since electrons are accumulated near the sheath.

Figure 2.6 shows the steady-state species density profiles averaged over an RF cycle for charged species and neutral species respectively. As Figure 2.6 (a) shows,  $H_3^+$  ions are dominant over the discharge. It is mainly produced from reaction RH16 in Annex II. For negative ions,  $SiH_3^-$  and  $SiH_2^-$  are one order larger than other negative ions. They are mainly produced from dissociative attachment reactions (RE11-RE13 in Annex I). The electron density is of the order of  $10^9 \text{ cm}^{-3}$ , smaller than other negative species. Figure 2.6 (b) shows the neutral species across the discharge averaged over one RF cycle. As one can see,  $H_2$  and  $SiH_4$  as inlet gas species are dominant and remain nearly constant over the reactor. For Si-containing species,  $SiH_3$  is the dominant one, and  $SiH_3$  radicals are the main precursors for deposition of the silicon thin film, as reported by J. Perrin<sup>5</sup>, Mataras<sup>42</sup>, *et al.* Figure 2.7 (a) shows the normal velocity profile along the Z axis in the reactor. The normal velocity describes the fluid velocity of gas

---

<sup>42</sup> D. G. Tsalikis et al, *J. Chem. Phys.*,139(20):204706,2013.

mixture along the Z axis. The gas mixture is injected from the powered electrode and



**Figure 2.6** Species density profile between the electrodes averaged over one RF cycle (a) charged species density; (b) neutral species density.  $Z = 0$  cm points to grounded electrode and  $Z = 1.6$  cm points to driven electrode. The gas pressure is fixed at 1 Torr, gas temperature is 448 K, the applied potential at RF electrode is 200 V, silane mass concentration is 1.4%, and hydrogen mass concentration is at 98.6%.

flows towards the grounded electrode. The silane and hydrogen is inlet into reactor from powered electrode with velocity of about 7 cm/s and the normal velocity decreases to zero at the grounded electrode. Figure 2.7(b) presents the tangential velocity in the reactor. The tangential velocity of the gas mixture describes the tangential component of fluid velocity, which is along the  $e_r$  axis (showed in Figure 2.1). We can see that the tangential velocity reaches to the maximum at the mid of the reactor in Z axis.

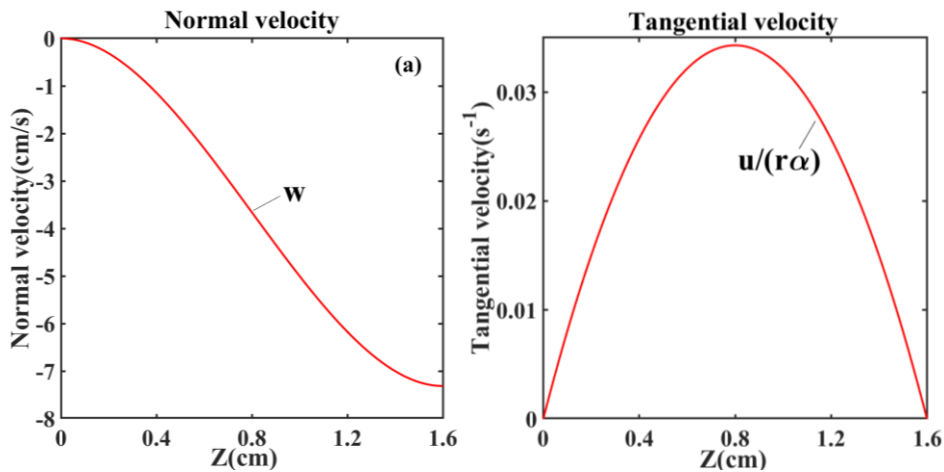


**Figure 2.7** (a) Normal velocity profile along the Z axis in the discharge; (b) Tangential velocity profile.

## 2.13 Conclusions

A 1-D fluid self-consistent model has been developed to simulate SiH<sub>4</sub>/H<sub>2</sub> plasma discharges. This model includes electrical properties, convection velocity, chemical mechanism in the discharge, deposition and etching rate analysis. The Poisson equation is used for the electric potential and the equation for the electron temperature is incorporated. The expressions for transport fluxes have been simplified by using Hirschfelder-Curtiss approximation<sup>7,25</sup>. A complete chemistry mechanism includes: i) electron collision reactions which depend on the electron temperature; ii) heavy-species reactions which depend on the heavy-species temperature; iii) surface chemistry mechanisms.

Under typical process conditions, the 1-D fluid model is performed to study the silane-hydrogen plasma properties. After about 40000 RF cycles a steady state solution is obtained. For the electric properties, the electric potential is larger at the center of discharge (plasma bulk) than that in the vicinity of electrodes (plasma sheaths). Also, the electric potential is nearly constant in the bulk, while a potential drop occurs in the sheaths. The electric field only appears in the plasma sheaths, and it is almost zero in the plasma bulk. The electron temperature in the sheath regions increases when the sheaths expand, while it remains around 5 eV in the plasma bulk. Electrons are mostly constrained in the plasma bulk, and the secondary electrons are emitted with high energy when sheath expands due to the electric field.

The most dominant positive ions are H<sub>3</sub><sup>+</sup>, which are mainly produced from reaction H<sub>2</sub>+H<sub>2</sub><sup>+</sup>→H<sub>3</sub><sup>+</sup>+H. SiH<sub>3</sub><sup>-</sup> and SiH<sub>2</sub><sup>-</sup> are the dominant negative ions. They are mainly produced from dissociative attachment reactions. For neutral species, the SiH<sub>3</sub> radicals are the most abundant Si-containing species, it is the main precursor of silicon thin film deposition.

Finally, the convection velocity is modelled based on equation (2.3.12) and (2.3.13). The gas mixture is inlet from RF powered electrode side with fixed velocity. The normal velocity decreases along the Z axis in the reactor, and the tangential velocity reaches its maximum in the bulk of the discharge.

## References

- <sup>1</sup> J. M. Orlac'h, T. Novikova, V. Giovangigli, E. Johnson and P. Roca. i Cabarrocas, Impact of Charged Species Transport Coefficients on Self-Bias Voltage in an Electrically Asymmetric RF Discharge, *Plasma Sources Sci. Technol.*28(5): 055003,2019, <https://doi.org/10.1088/1361-6595/ab067d>.
- <sup>2</sup> J.M. Orlac'h, V. Giovangigli, T. Novikova, P.Roca. i Cabarrocas, Kinetic Theory of Two-Temperature Polyatomic Plasmas, *Physica A*, 494:503–46, 2018 <https://doi.org/10.1016/j.physa.2017.11.151>.
- <sup>3</sup> D. B. Graves and K. F. Jensen, A Continuum Model of DC and RF Discharges, *IEEE T. Plasma. Sci.*, 14(2): 78–91, 1986, <https://doi.org/10.1109/TPS.1986.4316510>.
- <sup>4</sup> D. J. Economou, Hybrid Simulation of Low Temperature Plasmas: A Brief Tutorial, *Plasma Processes Polym.* 14(1-2): 1600152,2017, <https://doi.org/10.1002/ppap.201600152>.
- <sup>5</sup> E. Amanatides, D. Mataras, and D. E. Rapakoulias, Effect of Frequency in the Deposition of Microcrystalline Silicon from Silane Discharges, *J. Appl. Phys.*,90(11): 5799–5807,2001, <https://doi.org/10.1063/1.1413240>.
- <sup>6</sup> E. Amanatides, D. E. Rapakoulias, and D. Mataras, Electron-Impact Silane Dissociation and Deposition Rate Relationship in the PECVD of Microcrystalline Silicon Thin Films, *Le Journal de Physique IV*, 11(PR3):722,2001, <https://doi.org/10.1051/jp4:2001390>.
- <sup>7</sup> E. Amanatides, S. Stamou, and D. Mataras, Gas Phase and Surface Kinetics in Plasma Enhanced Chemical Vapor Deposition of Microcrystalline Silicon: The Combined Effect of Rf Power and Hydrogen Dilution, *J. Appl. Phys.*, 90(11): 5786–98,2001, <https://doi.org/10.1063/1.1413241>.
- <sup>8</sup> E. Amanatides, A. Hammad, E. Katsi, and D. Mataras, High Pressure Regime of Plasma Enhanced Deposition of Microcrystalline Silicon, *J. Appl. Phys.*, 97(7):073303, 2005, <https://doi.org/10.1063/1.1866477>.
- <sup>9</sup> A. Matsuda, Growth Mechanism of Microcrystalline Silicon Obtained from Reactive Plasmas, *Thin Solid Films*, 337(1): 1–6,1999, <https://doi.org/10.1016/S0040->

6090(98)01165-1.

<sup>10</sup> P. Roca, J. Cabarrocas, J. B. Chevrier, J. Hue, A. Lloret, J. Y. Parey, and J. P. M. Schmitt, A Fully Automated Hot-wall Multiplasma-monochamber Reactor for Thin Film Deposition, *J. Vac. Sci. Technol. A*, 9(4): 2331–41, 1991, <https://doi.org/10.1116/1.577318>.

<sup>11</sup> V. Giovangigli, *Multicomponent Flow Modeling*, Modeling and Simulation in Science, Engineering and Technology (Birkhäuser Basel, 1999), <https://doi.org/10.1007/978-1-4612-1580-6>.

<sup>12</sup> D. B. Graves and K. F. Jensen, A Continuum Model of DC and RF Discharges, *IEEE T. Plasma. Sci.*, 14(2): 78–91, 1986, <https://doi.org/10.1109/TPS.1986.4316510>.

<sup>13</sup> J. P. Boeuf and Ph. Belenguer, Transition from a Capacitive to a Resistive Regime in a Silane Radio Frequency Discharge and Its Possible Relation to Powder Formation, *J. Appl. Phys.* 71(10): 4751–54, 1992, <https://doi.org/10.1063/1.350666>.

<sup>14</sup> K. De Bleeker, A. Bogaerts, W. Goedheer, and R. Gijbelset, Investigation of Growth Mechanisms of Clusters in a Silane Discharge with the Use of a Fluid Model, *IEEE T. Plasma. Sci.*, 32(2): 691–98, 2004, <https://doi.org/10.1109/TPS.2004.826095>.

<sup>15</sup> J. M. Orlac'h, Modeling of a Silane-Hydrogen Plasma Discharge Including Nanoparticle Dynamics for Photovoltaic Applications. These de doctorat, Université Paris-Saclay, 2017, <https://www.theses.fr/2017SACLX023>.

<sup>16</sup> V. Giovangigli, Multicomponent Flow Modeling, *Science China Mathematics* 55(2): 285–308, 2012, <https://doi.org/10.1007/s11425-011-4346-y>.

<sup>17</sup> P. J. Linstrom and W. G. Mallard, The NIST Chemistry WebBook: A Chemical Data Resource on the Internet, *J. Chem. Eng. Data*, 46(5): 1059–63, 2001, <https://doi.org/10.1021/je000236i>.

<sup>18</sup> R. J. Kee, F. M. Rupley, and J. A. Miller, The Chemkin Thermodynamic Data Base, 1990, <http://adsabs.harvard.edu/abs/1990ctdb.rept.....K>.

<sup>19</sup> J. O. Hirschfelder and C. F. Curtiss, Theory of Propagation of Flames. Part I: General Equations, *Symposium on Combustion and Flame, and Explosion Phenomena*, 3(1): 121–27, 1948, [https://doi.org/10.1016/S1062-2896\(49\)80015-8](https://doi.org/10.1016/S1062-2896(49)80015-8).

- <sup>20</sup> E. S. Oran and J. P. Boris, Detailed Modelling of Combustion Systems, *Prog. Energy Combust. Sci.*, 7(1): 1–72, 1981, [https://doi.org/10.1016/0360-1285\(81\)90014-9](https://doi.org/10.1016/0360-1285(81)90014-9).
- <sup>21</sup> V. Giovangigli, Convergent Iterative Methods for Multicomponent Diffusion, *Comput. Sci. Eng.*, 3(3): 244–76, 1991, [https://doi.org/10.1016/0899-8248\(91\)90010-R](https://doi.org/10.1016/0899-8248(91)90010-R).
- <sup>22</sup> R. G. Mortimer and H. Eyring, Elementary Transition State Theory of the Soret and Dufour Effects, *Proc. Natl. Acad. Sci. U.S.A.*, 77(4):1728–31,1980, <https://doi.org/10.1073/pnas.77.4.1728>.
- <sup>23</sup> V. Giovangigli,EGLIB, 2021, <http://www.cmap.polytechnique.fr/www.eglib/>.
- <sup>24</sup> R. J. Kee, G. D. Lewis, J. Warnatz, M. E. Coltrin, J. A. Miller, H. K. Moffat, A Fortran computer code package for the evaluation of gas-phase multicomponent transport properties, *Sandia National Laboratories Report SAND86-8246, 13*, 80401-1887, <https://www3.nd.edu/~powers/ame.60636/transport1986.pdf>.
- <sup>25</sup> G. J. M. Hagelaar and L. C. Pitchford, Updates on the Freeware Electron Boltzmann Equation Solver BOLSIG +, In *APS Annual Gaseous Electronics Meeting Abstracts*, 2013, <https://ui.adsabs.harvard.edu/abs/2013APS..GECMR1075H/abstract>.
- <sup>26</sup> K. D. Bleecker, A. Bogaerts, and W. Goedheer, Modeling of the Formation and Transport of Nanoparticles in Silane Plasmas, *Phys. Rev. E*, 70(5):056407,2004, <https://doi.org/10.1103/PhysRevE.70.056407>.
- <sup>27</sup> Tolman, The Principles of Statistical Mechanics, *Dover Publications*,2010, [https://www.abebooks.co.uk/Principles-Statistical-Mechanics-Tolman-Dover Publications/30516068611/bd](https://www.abebooks.co.uk/Principles-Statistical-Mechanics-Tolman-Dover-Publications/30516068611/bd).
- <sup>28</sup> B. Graille, T. Magin, and M. Massot, Modeling of Reactive Plasmas for Atmospheric Entry Flows Based on Kinetic Theory, *Proceedings of the Summer Program 2008*, 2008.
- <sup>29</sup> M. C. M. van de Sanden, P. P. J. M. Schram, A. G. Peeters, J. A. M. van der Mullen, and G. M. W. Kroesen, Thermodynamic Generalization of the Saha Equation for a Two-Temperature Plasma, *Phys. Rev. A*, 40(9): 5273–76,1989, <https://doi.org/10.1103/PhysRevA.40.5273>.
- <sup>30</sup> D. Giordano and M. Capitelli, Nonuniqueness of the Two-Temperature Saha

Equation and Related Considerations, *Phys. Rev. E*, 65(1):016401,2001, <https://doi.org/10.1103/PhysRevE.65.016401>.

<sup>31</sup> D. P. Lymberopoulos and D. J. Economou, Two-Dimensional Self-Consistent Radio Frequency Plasma Simulations Relevant to the Gaseous Electronics Conference RF Reference Cell, *J. Res. Natl. Inst. Stand. Technol.*,100(4):473–94,1995, <https://doi.org/10.6028/jres.100.036>.

<sup>32</sup> D. P. Lymberopoulos and D. J. Economou, Fluid Simulations of Glow Discharges: Effect of Metastable Atoms in Argon, *J. Appl. Phys.*,73(8):3668–79,1993, <https://doi.org/10.1063/1.352926>.

<sup>33</sup> C. R. Kleijn, Computational Modeling of Transport Phenomena and Detailed Chemistry in Chemical Vapor Deposition – a Benchmark Solution,*Thin Solid Films*,365(2): 294–306,2000, [https://doi.org/10.1016/S0040-6090\(99\)01060-3](https://doi.org/10.1016/S0040-6090(99)01060-3).

<sup>34</sup> R. J. Kee, M. E. Coltrin, and P. Glarborg, Chemically Reacting Flow: Theory and Practice, *John Wiley & Sons*, 2005.

<sup>35</sup> H. Motz and H. Wise, Diffusion and Heterogeneous Reaction. III. Atom Recombination at a Catalytic Boundary, *J. Chem. Phys.*, 32(6):1893–94,1960, <https://doi.org/10.1063/1.1731060>.

<sup>36</sup> P. Diomedede et al., “Hybrid Simulation of a Dc-Enhanced Radio-Frequency Capacitive Discharge in Hydrogen,” *Journal of Physics D: Applied Physics* 45, no. 17 (April 2012): 175204, <https://doi.org/10.1088/0022-3727/45/17/175204>.

<sup>37</sup> A. Haji-Sheikh, B. Litkouhi, D.W. Pepper, H. Koenig and J. V. Beck,“Series in Computational Methods and Physical Processes in Mechanics and Thermal Sciences - Book Series - Routledge & CRC Press,” accessed April 4, 2021, <https://www.routledge.com/Series-in-Computational-Methods-and-Physical-Processes-in-Mechanics-and/book-series/TFSE00229>.

<sup>38</sup> E. Süli, An Introduction to Numerical Analysis, *Wiley*,2021, <https://www.wiley.com/enus/An+Introduction+to+Numerical+Analysis%2C+2nd+Edition-p-9780471624899>.

<sup>39</sup> D. L. Scharfetter and H. K. Gummel, “Large-Signal Analysis of a Silicon Read Diode

Oscillator,” *IEEE Transactions on Electron Devices* 16, no. 1 (January 1969): 64–77, <https://doi.org/10.1109/T-ED.1969.16566>.

<sup>40</sup> O. Leroy et al., Spatiotemporal Analysis of the Double Layer Formation in Hydrogen Radio Frequency Discharges, *J. Phys. D: Appl. Phys.*, 28, no. 3 (March 14, 1995): 500, <https://doi.org/10.1088/0022-3727/28/3/009>.

<sup>41</sup> A. Salabas and L. Marques, Systematic Characterization of Low-Pressure Capacitively Coupled Hydrogen Discharges, *J. Appl. Phys.*, 95(9):4605–20, 2004, <https://doi.org/10.1063/1.1690488>.

<sup>42</sup> D. G. Tsalikis et al., “A Hybrid Kinetic Monte Carlo Method for Simulating Silicon Films Grown by Plasma-Enhanced Chemical Vapor Deposition,” *The Journal of Chemical Physics* 139, no. 20 (November 26, 2013): 204706, <https://doi.org/10.1063/1.4830425>.

# Chapter 3 Role of $\text{SiH}_x$ radicals and $\text{H}_3^+$ ions in deposition and etching of silicon thin films from $\text{SiH}_4/\text{H}_2$ discharges

## Contents

<b>Chapter 3 Role of <math>\text{SiH}_x</math> radicals and <math>\text{H}_3^+</math> ions in deposition and etching of silicon thin films from <math>\text{SiH}_4/\text{H}_2</math> discharges .....</b>	<b>49</b>
<b>3.1 Introduction.....</b>	<b>50</b>
<b>3.2 Experimental setup and parameters.....</b>	<b>53</b>
<b>3.3 Silicon thin film characterization techniques.....</b>	<b>54</b>
<b>3.4 Results and discussions.....</b>	<b>57</b>
<b>3.5 Conclusions.....</b>	<b>67</b>
<b>References.....</b>	<b>68</b>

### 3.1 Introduction

Plasma-enhanced chemical vapor deposition (PECVD)<sup>1,2,3</sup> has been widely used for a wide variety of silicon thin films deposition, including hydrogenated amorphous silicon (a-Si:H), microcrystalline ( $\mu$ c-Si:H) and crystalline silicon (c-Si) epitaxial films for applications in large-area electronics, optoelectronics, and photovoltaics. For silicon thin-film deposition in CCP RF discharges, the plasma process parameters have a big impact on the growth rate and film properties, e.g., gas pressure, silane concentration, excitation frequency, RF power, and inter-electrode distance. Even if there is a general agreement on SiH<sub>3</sub> being the main film precursor under standard PECVD conditions, i.e. low pressure (< 100 mTorr) and low RF power ( $\sim 10$  mW/cm<sup>2</sup>)<sup>4</sup>, other precursors such as silicon clusters (Si<sub>n</sub>H<sub>m</sub>) and etching by atomic hydrogen, H<sub>2</sub><sup>+</sup> and H<sub>3</sub><sup>+</sup> may also play a role<sup>5</sup>. However, the processes taking place in silane/hydrogen discharges, including plasma chemistry and plasma-surface interactions, are complex and still not fully understood. In particular, the details of the growth mechanisms remain unclear.

Modeling of silane-based plasmas has been widely applied to understand the plasma chemistry and to determine the contribution of different species to the growth<sup>6,7,8,9</sup>. However, most of these studies are related to the low-pressure conditions and are not representative of the high-pressure regime in which we are interested in for the deposition of polymorphous silicon thin films on glass substrates and epitaxial growth on c-Si<sup>10,11</sup>.

Nevertheless, a few groups have studied such high-pressure conditions. The group of D. Mataras developed an experimental based chemical kinetic-mass transfer model to study the growth of  $\mu$ c-Si:H in highly diluted SiH<sub>4</sub> in H<sub>2</sub> discharges<sup>12</sup>. Besides the

---

<sup>1</sup> A. M Antoine et al., *J. Non. Cryst. Solids*, 77–78(2): 769–72, 1985.

<sup>2</sup> Werner Luft, Hydrogenated Amorphous Silicon Alloy Deposition Processes, *Applied Physics Series*, 1993.

<sup>3</sup> P. Roca i Cabarrocas et al., *Mater. Res. Soc. Symp. Proc.*, 1426: 319–29, 2012.

<sup>4</sup> R. A. Street, Hydrogenated Amorphous Silicon, *Cambridge University Press*, 2005.

<sup>5</sup> K. Landheer et al., *J. Appl. Phys.* 120(5): 053304, 2016.

<sup>6</sup> G. J. Nienhuis et al., *J. Appl. Phys.* 82(5): 2060–71, 1997.

<sup>7</sup> Olivier Leroy et al., *Plasma Sources Sci. Technol.*, 7(3): 348–58, 1998.

<sup>8</sup> A. A. Howling et al., *Plasma Sources Sci. Technol.*, 21(1): 015005, 2012.

<sup>9</sup> Mark J. Kushner, *O.P.L.*, 68, 1986.

<sup>10</sup> Pere Roca i Cabarrocas et al., *Pure Appl. Chem.*, 74(3): 359–67, 2002.

<sup>11</sup> P. Roca i Cabarrocas et al., *J. Phys. D:Appl.Phys.*, 40(8): 2258–66, 2007.

<sup>12</sup> E. Amanatides et al, *J. Appl. Phys.*, 90(11): 5786–98, 2001.

38 gas phase reactions considered, their model also includes a set of surface chemical reactions based on three types of surface sites: dangling bond sites, H covered sites and SiH<sub>3</sub> physisorbed sites. The reaction probabilities for each radical with different surface sites are taken into account, for example, the reaction probability of SiH<sub>3</sub> radical and Si<sub>2</sub>H<sub>5</sub> radical with dangling bond sites is equal to 1 and this probability with H covered sites is 0.5. The sticking coefficients  $\sigma$  of SiH<sub>3</sub> and Si<sub>2</sub>H<sub>5</sub> radicals are consistent with the work of J. Perrin<sup>13,14,15</sup>. J. Perrin<sup>13</sup> reviewed the physics and chemistry of low pressure SiH<sub>4</sub> glow discharges used to deposit hydrogenated amorphous silicon films (*a*-Si:H), including thermochemical data, electron-molecule collisions, ion-molecule collisions, neutral-neutral collisions, electron-ion collisions, ion-ion collisions and silicon cluster growth kinetics in dusty plasmas. He also studied the surface reaction probabilities ( $\beta$ ) and the kinetics of H, SiH<sub>3</sub>, Si<sub>2</sub>H<sub>5</sub> species during the deposition of *a*-Si:H films in the experiments, and found that  $\beta = 0.28 \pm 0.03$  for SiH<sub>3</sub>,  $0.1 < \beta < 0.3$  for Si<sub>2</sub>H<sub>5</sub>,  $0.4 < \beta < 1$  for H<sup>14,15</sup>, which are derived from the temporal decay of radical densities during the discharge afterglow by using time-resolved threshold ionization mass spectrometry. Under the high pressure–high SiH<sub>4</sub> concentration case (1 Torr, 6 % SiH<sub>4</sub> in H<sub>2</sub>), the deposition rate of  $\mu\text{c}$ -Si:H films increases from 1 Angstroms/s to 7 Angstroms/s with the increase of power density (10–70 mW/cm<sup>2</sup>). They reported Si<sub>2</sub>H<sub>4</sub>, SiH<sub>3</sub> and SiH<sub>2</sub> radicals to be the main precursors of the film deposition, while etching rate by H atoms was found to be negligible. Later on, D.G. Tsalikis in Mataras group<sup>16</sup> presented a hybrid kinetic Monte Carlo method to simulate the effect of the silane mole fraction in the range from 1% to 6% on the growth of nanocrystalline silicon in hydrogen/silane discharges at 3 Torr and 310 mW/cm<sup>2</sup> RF power. In their model, five species (H, SiH<sub>3</sub>, SiH<sub>2</sub>, SiH and Si<sub>2</sub>H<sub>5</sub>), which form 29 surface reactions with different surface sites, are taken into account in the surface process. As a result, the computed deposition rate shows an increasing trend as silane mole fraction increases, which reproduces the trend of experiments, but there is a

---

<sup>13</sup> J. Perrin et al, *Contrib. to Plasma Phys.*,36(1): 3–49,1996.

<sup>14</sup> Jérôme Perrin et al., *J. Vac. Sci. Technol. A*, 16(1): 278–89,1998.

<sup>15</sup> Jérôme Perrin et al, *Appl. Phys. Lett.*,50(8): 433–35,1987.

<sup>16</sup> D. G. Tsalikis et al., *J. Chem. Phys.*,139(20): 204706,2013.

discrepancy of about 2 Angstroms/s in deposition rate values between the model and experiments.

The species contributing to silicon thin film deposition mostly come from radicals in modelling studies. However, few researchers have considered the significance of ion species in deposition and etching process in silane/hydrogen discharges. L.L. Alves<sup>17</sup> studied the contributions of radicals and ions to deposition of a-Si:H films using a fluid model under conditions of very high silane concentration and low gas pressure (83% SiH<sub>4</sub>, 68 mTorr and 60% SiH<sub>4</sub>, 68 mTorr). The loss probabilities  $l$  and sticking coefficient  $\sigma$  of SiH<sub>3</sub> and Si<sub>2</sub>H<sub>5</sub> radicals were taken from J. Perrin<sup>13,14,15</sup>, while  $l = \sigma = 0.6$  was assumed for SiH<sub>2</sub> and Si<sub>2</sub>H<sub>4</sub> radicals. Ion loss possibilities were taken equal to 1. They found that the thin film formation is controlled by SiH<sub>3</sub> and SiH<sub>2</sub> radicals, while the contribution of ions (mainly SiH<sub>3</sub><sup>+</sup> and SiH<sub>2</sub><sup>+</sup>) to deposition is about 9%. In addition, the modelled deposition rates showed a good agreement with experiments. O. Leroy<sup>7</sup> also studied the role of ions in deposition and etching rate of a-Si:H films by using a 2D model under low-pressure conditions (9 Pa and 40 Pa). For the surface processes, the loss probability  $l$  and sticking coefficient  $\sigma$  of radicals are the same as J. Perrin<sup>13,14,15</sup>. For ions, both SiH<sub>m</sub><sup>+</sup> ions and H<sub>2</sub><sup>+</sup> ions (H<sup>+</sup> and H<sub>3</sub><sup>+</sup> are excluded) are considered in surface processes with sticking coefficient  $\sigma = 1$  and etching probability  $\varepsilon_k = 1$ . According to their results, the main film precursors are SiH<sub>3</sub> and SiH<sub>2</sub> radicals, while SiH<sub>m</sub><sup>+</sup> ions account for less than 10% of the deposition rate and H<sub>2</sub><sup>+</sup> ions etching rate was found to be negligible under the studied conditions. However, these studies about ions contribution to silicon thin film deposition rate are not in the high-pressure regime which we are interested in.

This work focuses on the comparison of experimental and modelled deposition rates taking place at a relatively high-pressure range (1-3.5 Torr) and low silane concentration (2 – 10% silane in hydrogen). These conditions lead to the growth of polymorphous silicon on glass substrates and epitaxial growth on (100) oriented crystalline silicon substrates<sup>3</sup>. The model includes Poisson's equation and the drift-

---

<sup>17</sup> L. L. Alves and L. Marques, *Plasma Phys. Control. Fusion*, 54(12):124012, 2012.

diffusion equations with the appropriate boundary conditions, the transport parameters, the reaction rates, and the gas-phase chemistry. In particular, the surface chemistry including recombination, etching, and deposition reactions is coupled to the fluid model via a set of reaction probabilities. The net deposition rate from the model is compared to that obtained experimentally and the main contributors to deposition and etching are identified.

## 3.2 Experimental setup and parameters

A capacitively coupled parallel plate reactor, having a base vacuum of  $10^{-7}$  mbar, was used for silicon thin film deposition<sup>18</sup>. Figure 3.1 shows a schematic representation of the axisymmetric reactor. The silane-hydrogen gas mixture is injected from the 15 cm diameter RF electrode side as shown in the figure. The lower electrode carrying the substrates is grounded and the gases are pumped via a slit between the substrate holder and a plasma box confining the discharge between the two electrodes.

In this work, <100> c-Si wafers and Corning glass were used as the substrates for silicon thin film deposition. For the series of experiments with varying silane concentration, the hydrogen flow rate was fixed at 500 sccm and the silane flow rate was varied whereas the total pressure was kept constant. For the pressure series experiments the gas flow rate of silane and hydrogen were kept constant at 7 sccm and 500 sccm, respectively, whereas the total pressure was varied by changing the pumping rate of the gases. From spectroscopic ellipsometry measurements it has been evidenced that polymorphous silicon films<sup>19</sup> are deposited on the glass substrates while on c-Si substrates the films are microcrystalline or epitaxial depending on the total pressure. The thickness of silicon thin films was determined from the modelling of spectroscopic ellipsometry measurements using a Tauc-Lorentz model for the polymorphous silicon films deposited on glass substrates<sup>19</sup> or a Bruggeman effective medium approximation model for the microcrystalline and epitaxial films deposited on c-Si substrates<sup>20</sup>. The

---

<sup>18</sup> P. Roca i Cabarrocas et al., *J. Vac. Sci. Technol. A*, 9(4): 2331–41,1991.

<sup>19</sup> A. Fontcuberta i Morral et al, *Phys. Rev. B*, 69(12): 125307, 2004.

<sup>20</sup> P. Roca i Cabarrocas et al., *Appl. Phys. Lett.* 69(4): 529–31,1996.

corresponding deposition rates are calculated by dividing the measured thickness by deposition time. The film properties deduced from spectroscopic ellipsometry measurements and modelling will be discussed below.

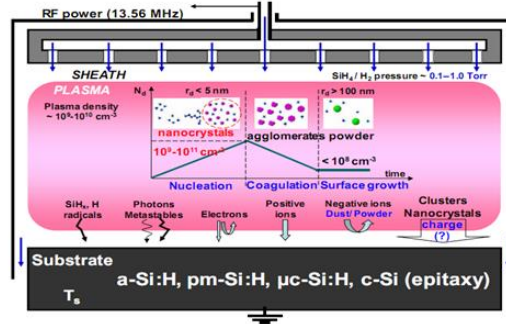


**Figure 3.1** Schematic representation of a parallel plate capacitively coupled RF glow discharge reactor<sup>3</sup>.

### 3.3 Silicon thin film characterization techniques

#### 3.3.1 Introduction of spectroscopic ellipsometry

In this study, the spectroscopic ellipsometry is used to characterize the properties of silicon thin films. Spectroscopic ellipsometry is a powerful technique, which is not only useful for ex-situ characterization but also this setup can be mounted on a PECVD reactor to study in-situ material growth from which one can detect small variations in the thickness or the composition of a growing layer. In our study, spectroscopic ellipsometry is used for ex-situ characterization of silicon thin film. This technique is based on the measurement of change in polarization state of a probing light beam caused by the reflection on the material surface or the transmission through the material. From the change in polarization state, the film thickness and optical properties of the material can be inferred. Ellipsometry is particularly suitable for the characterization of semiconductors, where we have a large number of substrates, thin film layers ranging from a few nanometers to tens of microns, and multilayer structures. In addition, ellipsometry is a fast and non-destructive technique that allows the monitoring the growth of thin films in real time.

#### 3.3.2 Principle of spectroscopic ellipsometry

A schematic setup of the spectroscopic ellipsometry is shown in Figure 3.2. Unpolarized white light emitted from a light source is transmitted through a linear polarizer. Linearly polarized light impinges the sample placed on the sample stage. The incident beam of light is reflected by a sample, the polarization of light changes after reflection (in general, it becomes elliptically polarized). When polarized light is going through the modulator, it is affected by the modulated birefringence, and as a result the two components undergo a modulated phase shift: an input linearly polarized beam becomes elliptically polarized at the output of the modulator, and the size of the ellipse is modulated at the frequency of modulation. This modulation is performed without any mechanical movement, resulting in improved signal stability and accuracy. And then light goes through an analyzer to a detector. We can describe the electric field of the incident (i) and the reflected (r) light by a parallel (p-polarized) component, and a perpendicular (s-polarized) component with respect to the plane of incidence. Therefore, one can define two complex Fresnel reflection coefficients for the p-polarized and s-polarized light in the form

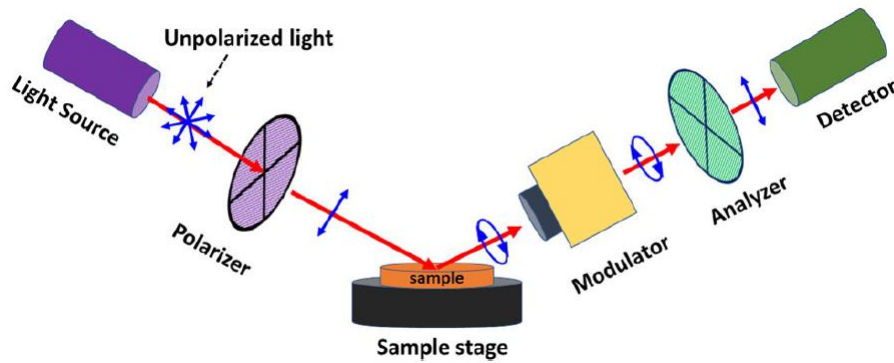


**Figure 3.2** Schematic diagram of spectroscopic ellipsometry system<sup>21</sup>.

$$\tilde{r}_p = |\tilde{r}_p| e^{i\theta_p}, \text{ and } \tilde{r}_s = |\tilde{r}_s| e^{i\theta_s} \quad (3.3.1)$$

where  $|\tilde{r}_p|$  and  $|\tilde{r}_s|$  are the modulus of the complex Fresnel reflection coefficient which indicate the attenuation of p-polarized and s-polarized light respectively, and  $\theta_p$  and  $\theta_s$  mean the phase change of the respective p-polarized and s-polarized light due to reflection. The change in polarization can be defined by the ratio of the complex

<sup>21</sup> Mithil Mazumder et al., *Int. J. Civ. Eng.*,18(3): 251–59,2020.

reflection coefficient, which is often written as

$$\vartheta = \frac{\tilde{r}_p}{\tilde{r}_s} = \tan(\varnothing) e^{i\Delta} \quad (3.3.2)$$

where  $\tan(\varnothing) = \frac{\tilde{r}_p}{\tilde{r}_s}$  indicates the ratio of the modules and  $\Delta = \theta_p - \theta_s$  ( $0^\circ \ll \Delta \ll 360^\circ$ ) is the phase change. The ellipsometry measures the parameters  $\varnothing$  and  $\Delta$ . Then the pseudo-dielectric function of the material can be written in the form

$$\langle \epsilon \rangle = \sin^2 \theta_i \left[ 1 + \tan^2 \theta_i \left( \frac{1-\vartheta}{1+\vartheta} \right)^2 \right] \quad (3.3.3)$$

where  $\theta_i$  is the incident angle. The pseudo-dielectric function (3.3.3) can also be expressed as a function of its real and imaginary part  $\langle \epsilon \rangle = \langle \epsilon_r \rangle + i \langle \epsilon_i \rangle$ . These two quantities are the ones which are usually used to characterize thin film materials<sup>22</sup>.

### 3.3.3 Modelling of spectroscopic ellipsometry data

From the measured parameters, the optical and structural properties of a silicon thin film can be determined by appropriate modelling. The parameters of interest include for example: complex refractive index of thin film material in near UV, visible, and near IR wavelength ranges; monolayer or multilayer thickness; thickness of layers in superlattice structure; surface and interface roughness; anisotropy and gradient of optical constants in single layers, *etc.*

In this study, the silicon thin films are modelled using Tauc-Lorentz dispersion formula<sup>23</sup> and Bruggeman effective medium approximation (BEMA)<sup>24</sup>. Tauc-Lorentz model is very popular for the representation of the dielectric functions of amorphous semiconductors and dielectrics<sup>25</sup>. The Tauc-Lorentz model requires the imaginary part of a pseudo-dielectric function  $\epsilon_i$  to be zero for the energies less than the band gap. Consequently, Tauc-Lorentz model does not consider the intra-band absorption: any defect or intra-band absorption increases the values of  $\epsilon_i$  below the band gap and generates bad fits in that region. For the BEMA model, the analytical model for well-known materials is used to model a more complex material, or a material whose composition depends on its thickness. In our case, the silicon thin films are deposited

<sup>22</sup> R.M.A. Azzam et al, *Ellipsometry and Polarized Light*, North-Holland Personal Library, 1988

<sup>23</sup> Melanie Gaillet, Tauc-Lorentz Dispersion Formula.

<sup>24</sup> D. a. G. Bruggeman, *Annalen der Physik*, 416(7): 636–64,1935.

<sup>25</sup> D. V. Likhachev et al, *Thin Solid Films* 589: 844–51, 2015.

on a crystalline wafer, whose thickness is taken as infinite. Also, the interface layer is considered since it occurs in epitaxial growth experimentally. Figure 3.3 shows the imaginary part of the dielectric function versus the photon energy (the red curve) for an epitaxial silicon thin film. As one can see, this function presents two peaks: at photon energies of 3.4 eV and 4.2 eV, which is typical profile for epitaxial silicon thin films.

In general, the spectroscopic ellipsometry is a very sensitive and powerful tool for the thin film thickness measurements. Also, it is good to mention that this technique is non-contact and non-destructive, that is important for research and industrial applications.

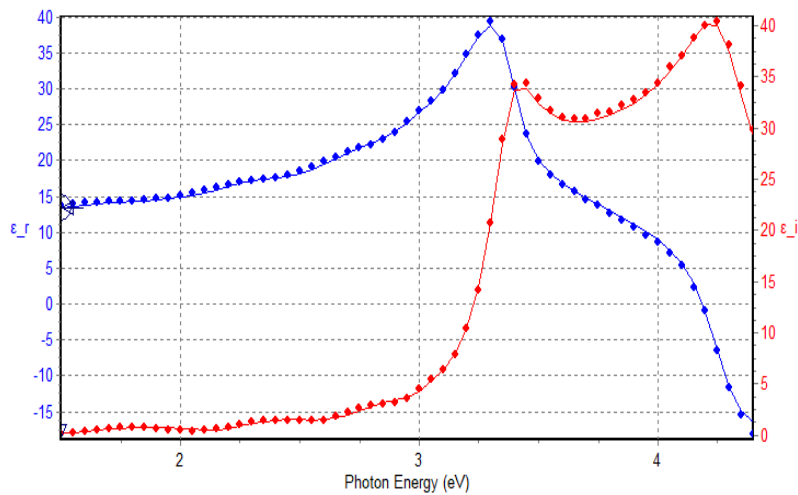


**Figure 3.3** Spectra of the real  $\epsilon_r$  and imaginary parts  $\epsilon_i$  of the pseudo-dielectric function as a function of photon energy, dots – experimental data, solid lines – results of the fit.

## 3.4 Results and discussions

### 3.4.1 The impact of silane concentration on deposition rate

In the following, we address the effect of silane concentration on the deposition rate. The reactor geometry and process conditions are defined as follows: the gas temperature is fixed at 448K, the pressure is 2 Torr, the dissipated RF power is 30 W, the inter-electrode distance is equal to 1.6 cm, and the silane concentration ( $\text{SiH}_4/(\text{SiH}_4+\text{H}_2)$ ) is varied from 2% to 10%. Increasing silane concentration is obtained by increasing the silane flow rate while keeping the  $\text{H}_2$  flow rate fixed at 500 sccm<sup>26</sup>.

<sup>26</sup> Ka-Hyun Kim et al., *Sci. Reports*, 7(1): 40553,2017.

Figure 3.4(a) shows the computed deposition rate (black triangles) compared with experimental values (red circles) taken from<sup>26</sup> as a function of silane concentration. As we can see, the model reproduces the trend in deposition rate, but there is a discrepancy

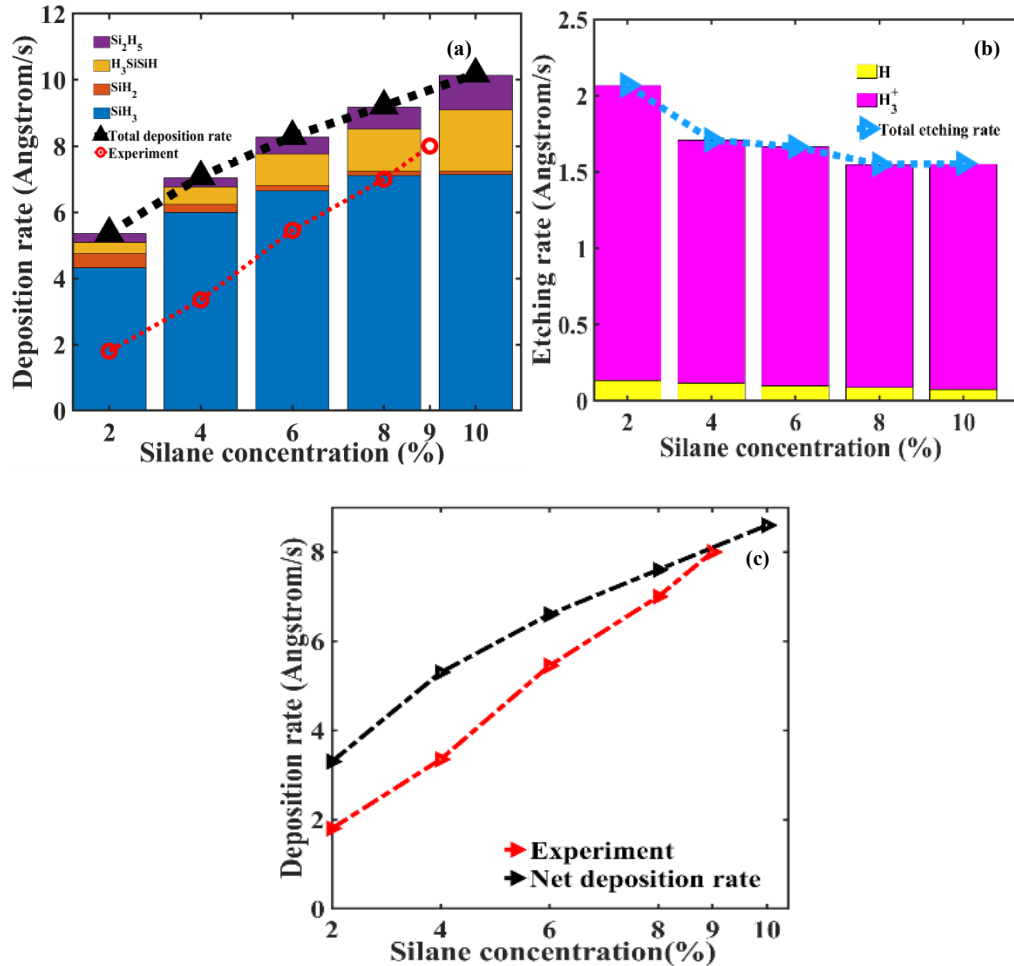


**Figure 3.4** Effect of the silane concentration on the deposition and etching rates. (a). Computed deposition rate compared with experimental values as a function of silane concentration. The black triangles indicate the computed deposition rate, the histograms show the contribution of the main species to deposition rate, and the red circles represent deposition rates from experiments. (b) Computed etching rate as a function of silane concentration, the histograms show the contribution of  $\text{H}$  and  $\text{H}_3^+$  to the etching rate. (c) The net deposition rate from the model is compared with experimental values.

in the absolute values, in particular, in the low silane concentration range. The contribution of species such as  $\text{SiH}_3$ ,  $\text{SiH}_2$ ,  $\text{Si}_2\text{H}_5$ , and  $\text{H}_3\text{SiSiH}$  to the total deposition rate is also shown in this figure. The  $\text{SiH}_3$  radical is found to be the main precursor for the film growth and its absolute contribution increases with the silane concentration in the gas mixture. For the given process conditions, other reactive species considered in

the model (see table I in Chapter 2) have a negligible contribution to the deposition rate. Note that the contribution of  $\text{Si}_2\text{H}_5$  and  $\text{H}_3\text{SiSiH}$  also shows an increasing trend with silane concentration, whereas  $\text{SiH}_2$  contribution to deposition rate decreases. Such behavior is the result of the secondary reactions (RH4, RH7, RH11 and RH12 in Annex II) which become important at 2 Torr. The contribution of ions to deposition is negligible compared to radicals; for example,  $\text{SiH}_3^+$  ions cover the range from 0.022 Å/s at 2% silane concentration to 0.038 Å/s at 10% silane concentration, which is less than 1% of the computed deposition rate.

Note that the difference in deposition rate between the model and experiments becomes smaller as silane concentration increases. To explain this difference, we consider etching by hydrogen species that will reduce the computed net deposition rate. Previous numerical studies have shown that etching by atomic hydrogen and hydrogen ions has a negligible effect<sup>7,12</sup>, while experimental studies have shown that etching does take place in RF hydrogen plasmas<sup>5,27,28</sup>. Figure 3.4(b) presents the total etching rate as a function of silane concentration. The increase of silane concentration results in a decrease in the total etching rate from 2.07 Å/s at 2% silane to 1.55 Å/s at 10% silane. Leroy et al.<sup>7</sup> suggested that the main precursor of etching is  $\text{H}_2^+$ , however, as can be seen in Figure 3.4 (b),  $\text{H}_3^+$  ions take over 90% of the etching rate, and shows a decreasing trend as silane concentration increases. For atomic hydrogen, the etching rate is much smaller compared to the  $\text{H}_3^+$  etching rate, which varies from 0.07 Å/s to 0.14 Å/s in the studied silane concentration range. The net deposition rate is determined as the difference between the computed deposition and etching rates. The comparison between the calculated net deposition rate and the corresponding experimental values is presented in Figure 3.4(c). We can see that the net deposition rate comes closer to the experimental values. It is interesting to mention that the contribution of  $\text{SiH}_3$  and  $\text{SiH}_2$  radicals tends to saturation at large  $\text{SiH}_4\%$ , (see Figure 3.4(a)). However, the additional contribution of the large radicals ( $\text{H}_3\text{SiSiH}$  and  $\text{Si}_2\text{H}_5$ ) and the decrease of the etching rate are enough to recover a linear increase of the net deposition rate. The deposition

<sup>27</sup> F. Käil et al., *Philos. Mag.*, 84(6): 595–609,2004.

<sup>28</sup> A. F. i Morral et al, *EPJ Appl. Phys.*, 35(3): 165–72,2006.

rate due to  $\text{Si}_2\text{H}_5$  radicals increases from 0.5 Å/s at 6%  $\text{SiH}_4$  to 1 Å/s at 10%  $\text{SiH}_4$ . For  $\text{H}_3\text{SiSiH}$  radicals the deposition rate increases from 0.94 Å/s at 6%  $\text{SiH}_4$  to 1.83 Å/s at 10%  $\text{SiH}_4$ . Whereas the etching rate decreases only from 1.66 Å/s at 6%  $\text{SiH}_4$  to 1.55 Å/s at 10%  $\text{SiH}_4$  (see Figure 3.4(b)). So the decrease of etching rate at large  $\text{SiH}_4\%$  is smaller than the increase of deposition rate due to the contribution of large radicals which recovers a linear increase of the net deposition rate.

The dominant contribution of the  $\text{SiH}_3$  radicals and  $\text{H}_3^+$  ions to the computed deposition and etching rates, respectively, can be traced back to the fluxes of the film precursors towards the substrate. Figure 3.5(a) shows the fluxes of various species towards the substrate as a function of silane concentration. It is clearly seen that the flux of  $\text{SiH}_3$  radicals is much larger than the fluxes of other radicals and ions. It indicates that  $\text{SiH}_3$  radicals are the main precursors of silicon thin film deposition, even if its sticking coefficient (0.1) is lower than that of  $\text{SiH}_2$  (0.8) and  $\text{H}_3\text{SiSiH}$  (0.8). As we can see, the increase of silane concentration is followed by an increase of  $\text{SiH}_3$  fluxes, from  $5.5 \times 10^{15} \text{ cm}^{-2} \cdot \text{s}^{-1}$  at 2% of silane to  $8.8 \times 10^{15} \text{ cm}^{-2} \cdot \text{s}^{-1}$  at 8% of silane, and then by a slight decrease to  $8.5 \times 10^{15} \text{ cm}^{-2} \cdot \text{s}^{-1}$  at 10% silane. We can see that the trend in  $\text{SiH}_3$  radical flux with silane concentration in Figure 3.5(a) reflects the trend of  $\text{SiH}_3$  deposition rate in Figure 3.4(a). Figure 3.5(b) shows the fluxes of  $\text{SiH}_2$  and higher silane species ( $\text{Si}_2\text{H}_5$ , and  $\text{H}_3\text{SiSiH}$ ) versus silane concentration. As we can see, the decrease of  $\text{SiH}_2$  flux and the increase of  $\text{Si}_2\text{H}_5$  and  $\text{H}_3\text{SiSiH}$  fluxes reflect the trends of their contribution to the deposition rate shown in Figure 3.4(a). These trends can be explained by the enhancement of the secondary reactions (see Annex II) taking place at 2 Torr. As shown in Figure 3.5(c),  $\text{H}_3^+$  ion flux decreases from  $7.3 \times 10^{14} \text{ cm}^{-2} \cdot \text{s}^{-1}$  at 2% of silane to  $4.7 \times 10^{14} \text{ cm}^{-2} \cdot \text{s}^{-1}$  at 10% of silane, and this trend correlates with the decrease of  $\text{H}_3^+$  ions etching rate as a function of silane concentration in Figure 3.4(b).

The contribution of each species to the deposition and etching rate as a function of silane concentration can also be traced back to each species production rate. Figure 3.6 presents the computed time-space-averaged production rates of species as a function of silane concentration. As Figure 3.6(a) shows, the production rate of  $\text{SiH}_3$  radicals is

dominant and its trend reflects the trend in SiH<sub>3</sub> radicals contribution to the deposition rate. From the model, we obtain that SiH<sub>3</sub> radicals are mainly produced by the secondary reaction SiH<sub>4</sub> + H = SiH<sub>3</sub> + H<sub>2</sub> (RH3 in Annex II). As silane concentration increases, the production rate of SiH<sub>3</sub> radicals increases from 7.6×10<sup>15</sup> cm<sup>-3</sup>·s<sup>-1</sup> at 2% of silane to 1.4×10<sup>16</sup> cm<sup>-3</sup>·s<sup>-1</sup> at 10% of silane. The concentration of atomic hydrogen stays high enough with silane concentration increase, because hydrogen is always in a large excess (≥90%). The production rates of the radicals SiH<sub>2</sub>, Si<sub>2</sub>H<sub>5</sub>, and H<sub>3</sub>SiSiH

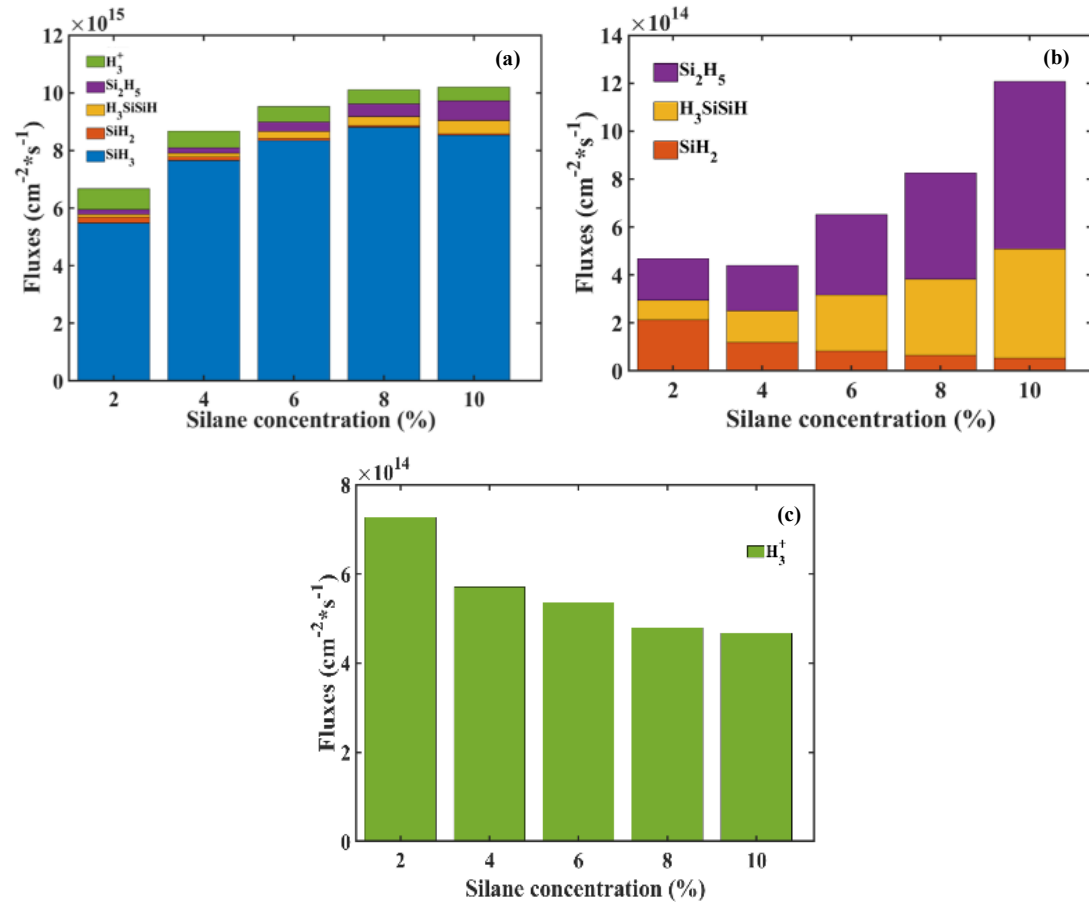


**Figure 3.5** Computed fluxes of species toward the substrate as a function of silane concentration. (a). Time-averaged fluxes of species (SiH<sub>2</sub>, Si<sub>2</sub>H<sub>5</sub>, H<sub>3</sub>SiSiH, SiH<sub>3</sub> and H<sub>3</sub><sup>+</sup>) toward the substrate. (b) Time-averaged fluxes of radicals SiH<sub>2</sub>, Si<sub>2</sub>H<sub>5</sub>, and H<sub>3</sub>SiSiH towards the substrate. (c) Time-averaged H<sub>3</sub><sup>+</sup> ions fluxes toward the substrate.

versus silane concentration are shown in Figure 3.6 (b). We can see that the decrease in the production rate of SiH<sub>2</sub> radicals and the increase in Si<sub>2</sub>H<sub>5</sub> and H<sub>3</sub>SiSiH production rates reflects the trend in their contribution to the deposition rate in Figure 3.4(a). The main etching precursor (H<sub>3</sub><sup>+</sup> ions) is mainly produced via the reaction H<sub>2</sub> + H<sub>2</sub><sup>+</sup> = H<sub>3</sub><sup>+</sup> + H (see RH16 in Annex II). Its production rate as a function of silane concentration is

presented in Figure 3.6 (c).  $H_3^+$  ions production rate decreases from  $1.72 \times 10^{15} \text{ cm}^{-3} \cdot \text{s}^{-1}$  at 2% of silane to  $1.23 \times 10^{15} \text{ cm}^{-3} \cdot \text{s}^{-1}$  at 10% of silane and this trend reflects the decrease of  $H_3^+$  ions etching rate as a function of silane concentration (see Figure 3.4(b)).

In summary, as silane concentration increases, the increase of experimental deposition rate values is reproduced qualitatively by the computed deposition rate, despite some quantitative discrepancy. The difference between computed and experimental values is considerably reduced by taking into account the etching rate. Also, we show that  $SiH_3$  radicals are the main precursors for the deposition, and  $H_3^+$

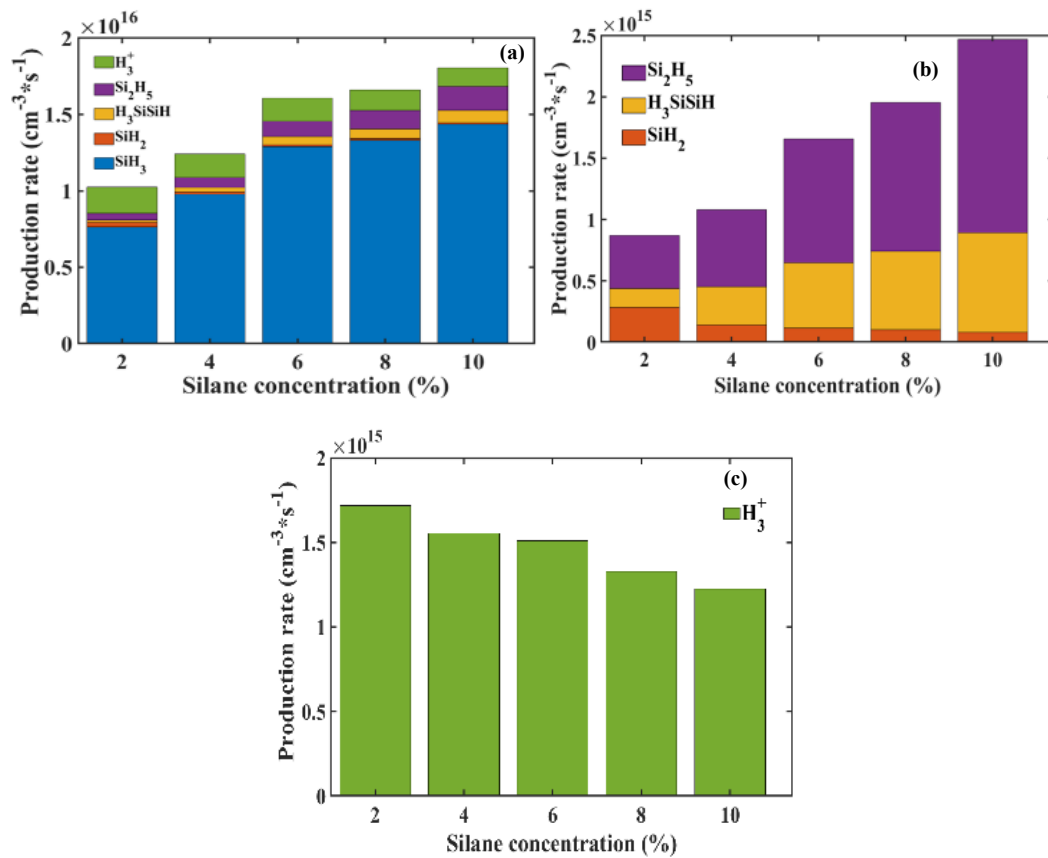


**Figure 3.6** (a) Computed time-space-averaged production rates of the species ( $SiH_2$ ,  $Si_2H_5$ ,  $H_3SiSiH$ ,  $SiH_3$  and  $H_3^+$ ) as a function of silane concentration. (b) Computed time-space-averaged production rates of the radicals  $SiH_2$ ,  $Si_2H_5$ , and  $H_3SiSiH$  as a function of silane concentration. (c) Computed time-space-averaged production rate of  $H_3^+$  ions as a function of silane concentration.

ions mainly contribute to the etching. In general, we can attribute the increase of the net deposition rate at small  $SiH_4\%$  (less than 6%) to the contribution of  $SiH_3$  radicals. However at large  $SiH_4\%$  ( $\geq 6\%$ ) the contribution of these radicals tends to saturate while that of large radicals ( $H_3SiSiH$  and  $Si_2H_5$ ) takes over. Finally, each species contribution is explained by its fluxes towards the substrate and its production rate.

### 3.4.2 *The impact of gas pressure on deposition rate*

In the following, we apply our model to study the effect of the gas pressure (in the range of 1- 3.5 Torr) on the deposition rate of silicon thin films deposited on c-Si substrates. For pressure series studies the following process conditions were defined: the gas temperature is fixed at 448K, the gas composition is 1.4 % SiH<sub>4</sub> + 98.6 H<sub>2</sub>, the applied RF power is 10 W, the inter-electrode distance is 1.6 cm. Figure 3.7 (a) shows the comparison of total deposition rate between modeling and experiments as a function of gas pressure. The trend in the experimental deposition rate on (100) crystalline silicon versus total pressure is reproduced by the computed deposition rates, however, as for the silane concentration studies, the values of the computed deposition rate are higher than the experimental ones. The computed deposition rate increases to a maximum of 2.6 Å/s at 2.5 Torr and then decreases to 2.2 Å/s at 3.5 Torr. In the experiments, the deposition rate has a maximum value of 1.52 Å/s at 2.75 Torr and then decrease to 1.37 Å/s at 3.5 Torr. The contributions of SiH<sub>3</sub>, SiH<sub>2</sub>, Si<sub>2</sub>H<sub>5</sub>, and H<sub>3</sub>SiSiH species to the total deposition rate are also shown in this figure. The SiH<sub>3</sub> radicals are the main precursors for silicon thin film deposition with a maximal value of corresponding deposition rate (2.33 Å/s) at 2.5 Torr that decreases to 2.06 Å/s at 3.5 Torr. Other radicals, such as SiH<sub>2</sub> show a decreasing contribution to the total deposition rate as gas pressure increases. The deposition rates due to the radicals Si<sub>2</sub>H<sub>5</sub> and H<sub>3</sub>SiSiH increases to a maximum (0.28 Å/s for Si<sub>2</sub>H<sub>5</sub>, 0.1 Å/s for H<sub>3</sub>SiSiH) at 2Torr, and then become negligible for pressure values above 2 Torr. The decreasing trend of the deposition rate of these radicals (SiH<sub>3</sub>, Si<sub>2</sub>H<sub>5</sub> and H<sub>3</sub>SiSiH) after 2.5 Torr is because silane dissociation rates decrease, as presented in Figure 3.8(a). The contribution of positive ions to the deposition is much smaller compared to that of radicals, for example, SiH<sub>3</sub><sup>+</sup> ions contribution ranges from 0.058 Å/s to 0.018 Å/s, which is less than 5% of the total deposition rate. Other ions, such as SiH<sub>2</sub><sup>+</sup> and Si<sub>2</sub>H<sub>4</sub><sup>+</sup> also have a negligible contribution to the total deposition rate.

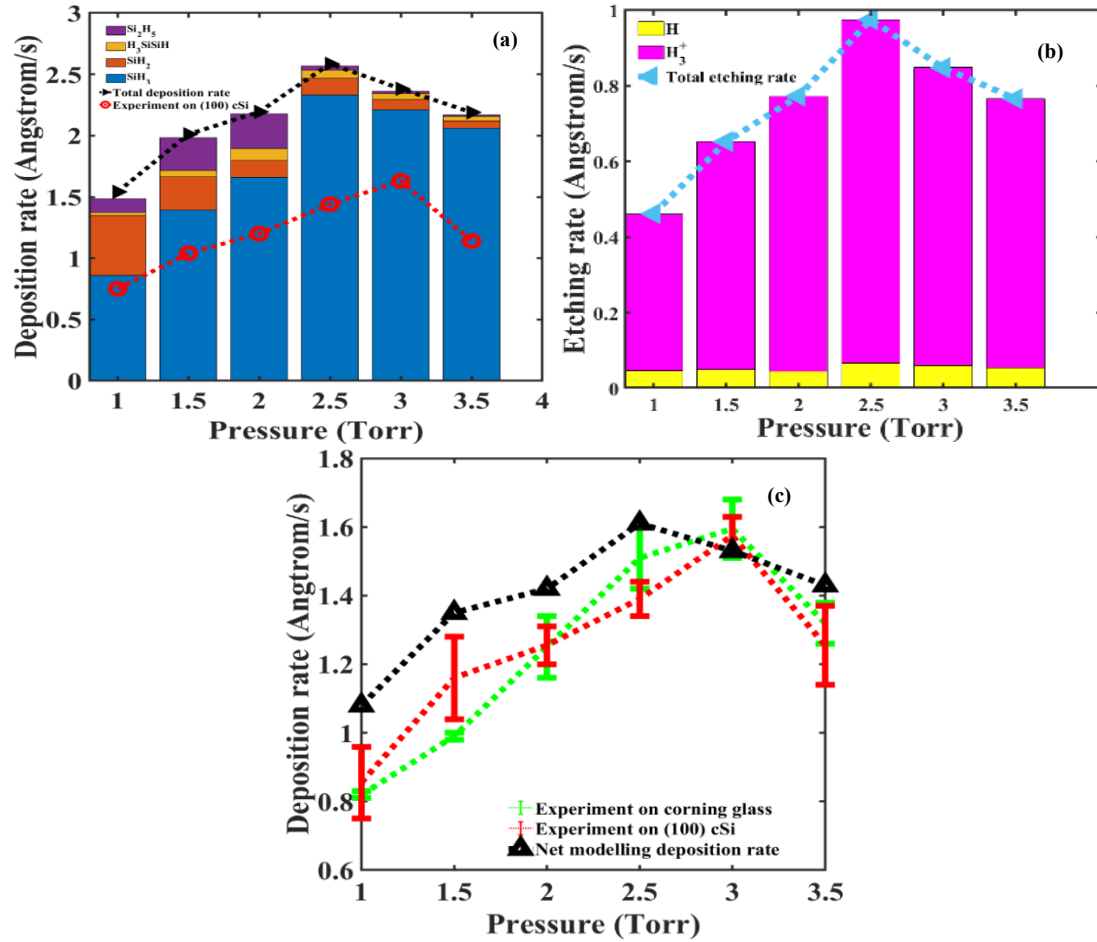


**Figure 3.7** Deposition rate and etching rate as a function of total gas pressure. (a). Experimental values of the deposition rate (red circles, computed values of the total deposition rate (black triangles); the histograms show the contribution of different radicals to the deposition rate. (b) Total etching rate as a function of gas pressure, the histograms show the contribution of different species to the etching rate. (c) The net deposition rate from the model compared with experimental values. The experimental deposition rates on corning glass and (100) cSi are indicated as green and red dotted lines, the error bars are presented at each pressure point.

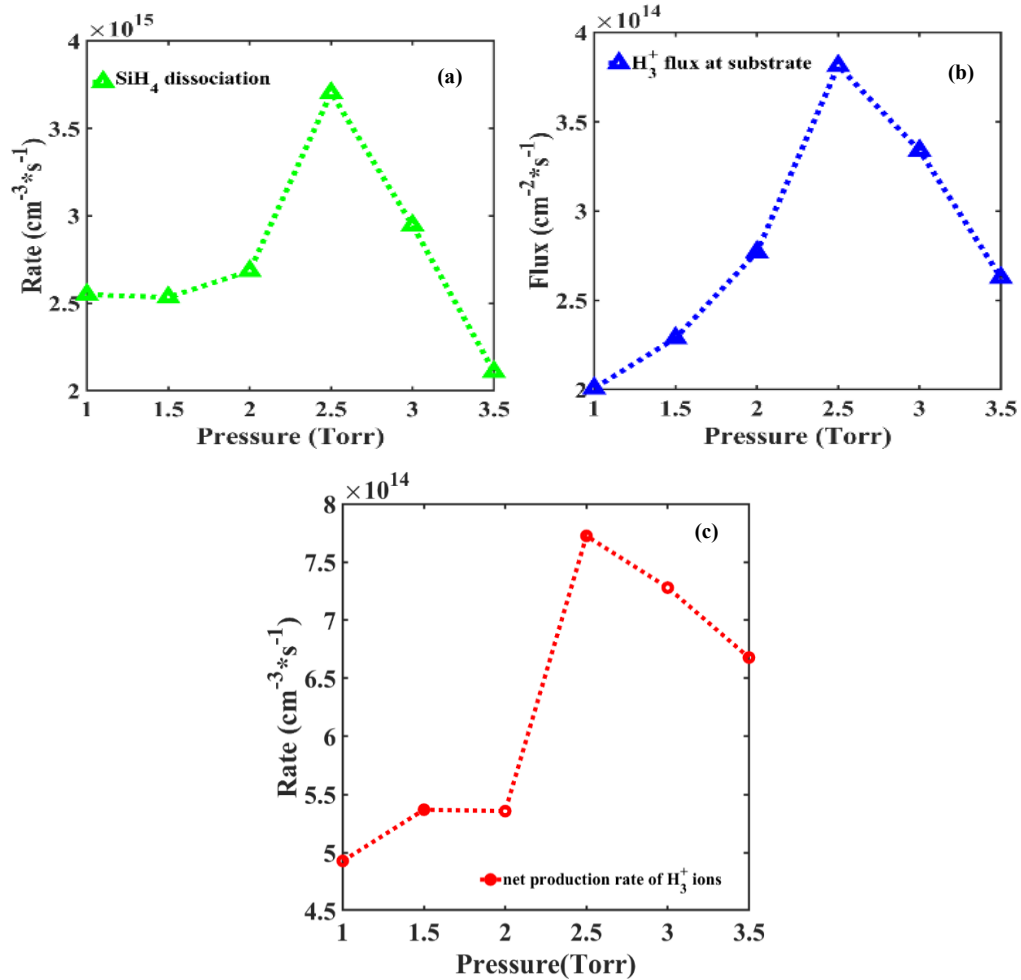
As for the silane concentration study, to account for the difference between the computed deposition rate and the experimental one, we consider the effect of etching by hydrogen species. Figure 3.7(b) presents the etching rate as a function of total gas pressure. The increase in gas pressure results in an increase in the etching rate from 0.46 Å/s at 1 Torr to 0.98 Å/s at 2.5 Torr and a decrease to 0.77 Å/s at 3.5 Torr. As we can see in Figure 3.7(b), the main precursors of etching are  $\text{H}_3^+$  ions, which take over 90% of the etching rate. The etching rate by atomic hydrogen is much smaller; it varies from 0.05 Å/s to 0.07 Å/s and reaches a maximum at 2.5 Torr. The decrease of etching rates by  $\text{H}_3^+$  ions above 2.5 Torr is due to the decrease of the  $\text{H}_3^+$  ion fluxes as shown in

Figure 3.8(b).

The comparison between the computed net deposition rate and the corresponding experimental values of deposition rate on (100) crystalline silicon and corning glass is shown in Figure 3.7 (c). The computed net deposition rate values are close to the corresponding experimental ones. Note that the deposition rate shows the same trend for the deposition on both c-Si and glass substrates. However, the structure of the films is completely different as it is polymorphous silicon on glass and c-Si (epitaxial) on c-Si, in agreement with our previous studies.

As we can see, the  $\text{SiH}_3$  radicals and  $\text{H}_3^+$  ions are dominant in deposition and etching process. It is very interesting to explain the dynamics of these two species in the pressure series. For  $\text{SiH}_3$  radicals, silane dissociation by electron impact and the reaction  $\text{H} + \text{SiH}_4 = \text{SiH}_3 + \text{H}_2$  are the main channels to produce  $\text{SiH}_3$  radicals, and other neutral species production rates cannot compare with  $\text{SiH}_3$ , so  $\text{SiH}_3$  radicals are the main precursor to the deposition even if it has smaller sticking coefficient than other species. The increase of deposition rate of  $\text{SiH}_3$  from 1 to 2.5 Torr is due to the increase of dissociation rate of  $\text{SiH}_4$  and  $\text{H}_2$ . From 2.5 Torr to 3.5 Torr, we can see the deposition rate of  $\text{SiH}_3$  radicals decrease. This is because at a constant power, the power deposited per molecule and the electron temperature decrease with the pressure increasing, which lowers the dissociation rate of  $\text{SiH}_4$  and therefore the production of  $\text{SiH}_3$  radicals.

$\text{H}_3^+$  ions can be produced from reactions RH16 and RH17 in Annex II, and RH16 ( $\text{H}_2 + \text{H}_2^+ = \text{H}_3^+ + \text{H}$ ) mainly produce  $\text{H}_3^+$  ions. While  $\text{H}_3^+$  ions can be consumed by reactions RE7, RE17, RE18 in Annex I and RS 5 in Annex IV, and RE17 ( $\text{H}_3^+ + \text{e} = 3\text{H}$ ) is the main consumption reaction in the discharge and RS5 ( $4\text{H}_3^+ (\text{g}) + 3\text{Si-wall} = 3\text{SiH}_4(\text{g})$ ) is the main consumption reaction at the surface. When the gas pressure increases from 1 to 2.5 Torr, the net production rate of  $\text{H}_3^+$  ions increases as it can be seen in the Figure 8(c). However, above 2.5 Torr, net production rate of  $\text{H}_3^+$  ions decrease. It should



**Figure 3.8** (a) Computed time-space-averaged SiH<sub>4</sub> dissociation rate as a function of gas pressure. (b). Computed time-averaged H<sub>3</sub><sup>+</sup> flux at substrate. (c) Time-space averaged net production rate of H<sub>3</sub><sup>+</sup> ions as a function of gas pressure.

be mentioned that at higher gas pressure (above 2.5 Torr in our case) both consumption and production of H<sub>3</sub><sup>+</sup> ions decrease, while the electron dissociative attachment rate (RE11, RE12 and RE13 in Annex I) increases, which will promote the cluster growth reactions (RH13 and RH14 in Annex II). Also, the H<sub>3</sub><sup>+</sup> ions fluxes are dominated by its thermal fluxes. At the boundaries, the H<sub>3</sub><sup>+</sup> ions thermal fluxes follow the trend in Figure 3.8 (b). So the net production of H<sub>3</sub><sup>+</sup> ions (production and consumption) controls the role of H<sub>3</sub><sup>+</sup> ions etching.

### 3.5 Conclusions

The 1-D fluid model for capacitively coupled RF silane-hydrogen discharges developed in<sup>29,30</sup> has been improved both in terms of plasma and surface chemistry to compute the deposition rate of silicon thin films. The computed deposition rates have been compared with the experimental ones for various values of total pressure and silane concentration. The computed total deposition rate linearly increases with silane concentration and SiH<sub>3</sub> radicals are the main precursors of thin film deposition in the pressure range of 1 to 3.5 Torr and for silane concentrations of 2 - 10%. The net deposition rate shows a good agreement with the experimental values after taking into account the etching rate. Moreover, modelling shows that H<sub>3</sub><sup>+</sup> ions are the main species contributing to the etching process and that their effect decreases with increasing silane concentration. Similar results have been obtained for the study on the effect of gas pressure on the deposition rate, namely the deposition rate is dominated by the contribution of SiH<sub>3</sub> radicals, while H<sub>3</sub><sup>+</sup> ions are responsible for the etching rate. At 2.5 Torr the etching rate by H<sub>3</sub><sup>+</sup> amounts to 1 Å/s, which is about 40% of the deposition induced by radicals (2.6 Å/s), resulting in a net deposition rate of 1.6 Å/s. After including the etching rate into the calculations of the net deposition rate the values of the latter come close to the experimental values.

---

<sup>29</sup> Jean-Maxime Orlac'h et al., *Plasma Sources Sci. Technol.*, 28(5): 055003, 2019.

<sup>30</sup> Jean-Maxime Orlac'h, Modeling of a Silane-Hydrogen Plasma Discharge Including Nanoparticle Dynamics for Photovoltaic Applications, These de doctorat, 2017.

## References

- <sup>1</sup>A. M. Antoine, B. Drevillon and P. Roca. i Cabarrocas, Growth Processes of RF Glow Discharge Deposited a-Si:H and a-Ge:H Films, *J. Non. Cryst. Solids*, 77–78 (2): 769–72, 1985, [https://doi.org/10.1016/0022-3093\(85\)90773-2](https://doi.org/10.1016/0022-3093(85)90773-2).
- <sup>2</sup> W. Luft and Y. S. Tsuo, Hydrogenated Amorphous Silicon Alloy Deposition Processes, *Applied Physics Series (Marcel Dekker, Inc.)*, 1993.
- <sup>3</sup> P. Roca. i Cabarrocas, K.H. Kim, R. Cariou, M. Labrune, E.V. Johnson, M. Moreno, A. T. Rios, S. Abolmasov and S. Kasouti, Low Temperature Plasma Synthesis of Nanocrystals and Their Application to the Growth of Crystalline Silicon and Germanium Thin Films, *Mater. Res. Soc. Symp. Proc.*, 1426:319–29, 2012, <https://doi.org/10.1557/opl.2012.1094>.
- <sup>4</sup> R. A. Street, Hydrogenated Amorphous Silicon, *Cambridge University Press*, 2005.
- <sup>5</sup> K. Landheer, W. J. Goedheer, I. Poullos, R. E. I. Schropp and J. K. Rath, Chemical Sputtering by  $H_2^+$  and  $H_3^+$  Ions during Silicon Deposition, *J. Appl. Phys.*, 120(5): 053304, 2016, <https://doi.org/10.1063/1.4960351>.
- <sup>6</sup> G. J. Nienhuis, W. J. Goedheer, E. A. G. Hamers, W. G. J. H. M. van Sark, and J. Bezemer, A Self-Consistent Fluid Model for Radio-Frequency Discharges in  $SiH_4-H_2$  Compared to Experiments, *J. Appl. Phys.*, 82(5):2060–71, 1997, <https://doi.org/10.1063/1.366016>.
- <sup>7</sup> O. Leroy, G. Gousset, L. L. Alves, J. Perrin and J. Jolly, Two-Dimensional Modelling of  $SiH_4-H_2$  Radio-Frequency Discharges for a-Si:H Deposition, *Plasma Sources Sci. Technol.*, 7(3): 348–58, 1998, <https://doi.org/10.1088/0963-0252/7/3/013>.
- <sup>8</sup> A. A. Howling, B. Legradic, M. Chesaux and C. Hollenstein, Plasma Deposition in an Ideal Showerhead Reactor: A Two-Dimensional Analytical Solution, *Plasma Sources Sci. Technol.*, 21(1): 015005, 2012, <https://doi.org/10.1088/0963-0252/21/1/015005>.
- <sup>9</sup> Mark J. Kushner, A Plasma Chemistry and Surface Model for the Deposition of a-Si:H from RF Glow Discharges: A Study of Hydrogen Content, *Mater. Res. Soc. Symp. Proc.*, 68:293-307, 1986, <https://doi.org/10.1557/PROC-68-293>.
- <sup>10</sup>P. Roca. i Cabarrocas, A. F. i Morral, S. Lebib and Y. Poissant, Plasma prod

uction of nanocrystalline silicon particles and polymorphous silicon thin films for large-area electronic devices, *Pure Appl. Chem.* 74(3): 359–67,2002, <https://doi.org/10.1351/pac200274030359>.

<sup>11</sup> P. Roca i Cabarrocas, T. Nguyen-Tran, Y. Djeridane, A. Abramov, E. Johnson and G. Patriarche, Synthesis of Silicon Nanocrystals in Silane Plasmas for Nanoelectronics and Large Area Electronic Devices, *J. Phys. D: Appl. Phys.* 40(8):2258–66,2007, <https://doi.org/10.1088/0022-3727/40/8/S04>.

<sup>12</sup> E. Amanatides, S. Stamou, and D. Mataras, Gas Phase and Surface Kinetics in Plasma Enhanced Chemical Vapor Deposition of Microcrystalline Silicon: The Combined Effect of Rf Power and Hydrogen Dilution, *J. Appl. Phys.*, 90(11):5786–98,2001, <https://doi.org/10.1063/1.1413241>.

<sup>13</sup> J. Perrin, O. Leroy, and M. C. Bordage, Cross-Sections, Rate Constants and Transport Coefficients in Silane Plasma Chemistry, *Contrib. to Plasma Phys.*, 36(1): 3–49,1996, <https://doi.org/10.1002/ctpp.2150360102>.

<sup>14</sup> J. Perrin, M. Shiratani, P. Kae-Nune, H. Videlot, J. Jolly and J. Guillon, Surface Reaction Probabilities and Kinetics of H, SiH<sub>3</sub>, Si<sub>2</sub>H<sub>5</sub>, CH<sub>3</sub>, and C<sub>2</sub>H<sub>5</sub> during Deposition of a-Si:H and a-C:H from H<sub>2</sub>, SiH<sub>4</sub>, and CH<sub>4</sub> Discharges, *J. Vac. Sci. Technol. A*, 16(1): 278–89, 1998, <https://doi.org/10.1116/1.580983>.

<sup>15</sup> J. Perrin and T. Broekhuizen, Surface Reaction and Recombination of the SiH<sub>3</sub> Radical on Hydrogenated Amorphous Silicon, *Appl. Phys. Lett.*, 50(8): 433–35,1987, <https://doi.org/10.1063/1.98165>.

<sup>16</sup> D. G. Tsalikis, C. Baig, V. G. Mavrantzas, E. Amanatides and D. Mataras, A Hybrid Kinetic Monte Carlo Method for Simulating Silicon Films Grown by Plasma-Enhanced Chemical Vapor Deposition, *J. Chem. Phys.*, 139(20): 20470 6,2013, <https://doi.org/10.1063/1.4830425>.

<sup>17</sup> L. L. Alves and L. Marques, Fluid Modelling of Capacitively Coupled Radio-Frequency Discharges: A Review, *Plasma Phys. Control. Fusion*, 54(12): 124012,2012, <https://doi.org/10.1088/0741-3335/54/12/124012>.

<sup>18</sup> P. Roca i Cabarrocas, J. B. Chévrier, J. Huc, A. Lloret, J. Y. Parey and J. P. M. Schmitt, A Fully Automated Hot-wall Multiplasma-monochamber Reactor

for Thin Film Deposition, *J. Vac. Sci. Technol. A*, 9(4): 2331–41,1991, <https://doi.org/10.1116/1.577318>.

<sup>19</sup> A. Fontcuberta. i Morral, P. Roca. i Cabarrocas and C. Clerc, Structure and Hydrogen Content of Polymorphous Silicon Thin Films Studied by Spectroscopic Ellipsometry and Nuclear Measurements, *Phys. Rev. B*, 69(12): 125307,2004, <https://doi.org/10.1103/PhysRevB.69.125307>.

<sup>20</sup> P. Roca. i Cabarrocas, S. Hamma and A. Hadjadj, New Features of the Layer-by-layer Deposition of Microcrystalline Silicon Films Revealed by Spectroscopic Ellipsometry and High Resolution Transmission Electron Microscopy, *Appl. Phys. Lett.* 69(4): 529–31, 1996, <https://doi.org/10.1063/1.117776>.

<sup>21</sup> M. Mazumder, R. Ahmed, M. Hasan, S. J. Lee and M. S. Lee, Spectroscopic Ellipsometry of Asphalt Binder: A Study of Optical Constants, *Int. J. Civ. Eng.*, 18(3): 251–59, 2020, <https://doi.org/10.1007/s40999-019-00468-5>.

<sup>22</sup> R.M.A. Azzam, N.M. Bashara, Ellipsometry and Polarized Light, *North-Holland Personal Library*, 1988.

<sup>23</sup> M. Gaillet, Tauc-Lorentz Dispersion Formula.

<sup>24</sup> D. A. G. Bruggeman, Berechnung verschiedener physikalischer Konstanten von heterogenen Substanzen. I. Dielektrizitätskonstanten und Leitfähigkeiten der Mischkörper aus isotropen Substanzen, *Annalen der Physik*, 416(7): 636–64,1935, <https://doi.org/10.1002/andp.19354160705>.

<sup>25</sup>D. V. Likhachev, N. Malkova, and L. Poslavsky, Modified Tauc–Lorentz Dispersion Model Leading to a More Accurate Representation of Absorption Features below the Bandgap, *Thin Solid Films*, 589 (31): 844–51, 2015, <https://doi.org/10.1016/j.tsf.2015.07.035>.

<sup>26</sup> K. H. Kim, E. V. Johnson, A. G. Kazanskii, M. V. Khenkin and P. Roca. i Cabarrocas, Unravelling a Simple Method for the Low Temperature Synthesis of Silicon Nanocrystals and Monolithic Nanocrystalline Thin Films, *Sci. Rep.*, 7(1): 40553,2017, <https://doi.org/10.1038/srep40553>.

<sup>27</sup> F. Käil, A. F. i Morral, A. Hadjadj, P. Roca. i Cabarrocas and A. Beorchia, Hydrogen-Plasma Etching of Hydrogenated Amorphous Silicon: A Study by a Combination of Spectroscopic Ellipsometry and Trap-Limited Diffusion Model,

*Philos. Mag.*, 84(6): 595–609, 2004, <https://doi.org/10.1080/14786430310001635440>.

<sup>28</sup>A. F. i Morral and P. Roca. i Cabarrocas, Role of Hydrogen Diffusion on the Growth of Polymorphous and Microcrystalline Silicon Thin Films, *EPJ Appl. Phys.* 35(3):165–72,2006, <https://doi.org/10.1051/epjap:2006094>.

<sup>29</sup>J. M. Orlac'h, T. Novikova, V. Giovangigli, E. Johnson and P. Roca. i Cabarrocas, Impact of Charged Species Transport Coefficients on Self-Bias Voltage in an Electrically Asymmetric RF Discharge, *Plasma Sources Sci. Technol.* 28(5): 055003,2019, <https://doi.org/10.1088/1361-6595/ab067d>.

<sup>30</sup>J. M. Orlac'h, Modeling of a Silane-Hydrogen Plasma Discharge Including Nanoparticle Dynamics for Photovoltaic Applications. These de doctorat, Université Paris-Saclay, 2017, <https://www.theses.fr/2017SACLX023>.



# Chapter 4 Nanoparticle formation in SiH<sub>4</sub>-H<sub>2</sub> discharges

## Contents

<b>Chapter 4 Nanoparticle formation in SiH<sub>4</sub>-H<sub>2</sub> discharges.....</b>	<b>73</b>
<b>4.1 Introduction.....</b>	<b>74</b>
<b>4.2 An overview of nanoparticle formation .....</b>	<b>75</b>
<b>4.3 Sectional model .....</b>	<b>79</b>
<b>4.4 Coupled 1-D fluid-sectional model.....</b>	<b>89</b>
<b>4.5 Numerical implementation .....</b>	<b>90</b>
<b>4.6 Results and discussion .....</b>	<b>94</b>
<b>4.7 Conclusions.....</b>	<b>104</b>
<b>4.8 References.....</b>	<b>105</b>

## 4.1 Introduction

This chapter studies the phenomenon of nanoparticle formation in SiH<sub>4</sub>-H<sub>2</sub> plasmas. In deposition plasmas, the formation of nanoparticles is considered to be harmful. This is related to the fact that semiconductor devices are shrinking in size. In this case, particles accidentally dropped on the substrate can damage the device, which are considered as "killer" particles. Therefore, the main motivation in microelectronics industry is to develop methods to make these plasmas 'particle-free'. A series of experimental and theoretical studies were conducted to understand the process of particle formation in deposition and etching plasmas so that methods can be developed to eliminate them<sup>1</sup>. Despite these efforts to eliminate particles from the plasma, it is recognized that these same objects can be used to achieve useful "electro-optical" properties if the particles are generated in a controlled size and composition.

Several studies have been made by Pere Roca i Cabarrocas<sup>2,3,4,5,6</sup> and coworkers at LPICM. Powder formation in silane-hydrogen plasmas was considered as a drawback because it might cause the formation of macroscopic defects in the deposited layers. However, Pere Roca<sup>2,3</sup> et al showed that silicon thin films can be deposited under deposition conditions close to those for powder formation and that these films have improved electronic transport properties which most likely result from the structure of this material made of nanoparticles embedded into an amorphous matrix, referred as polymorphous silicon (pm-Si:H). The light-soaking kinetics of pm-Si:H is faster than that of standard a-Si:H material. These properties make pm-Si:H promising for future photovoltaic applications. Moreover, nanoparticles have been shown to be involved in the growth of epitaxial Si on (100) oriented c-Si substrates. As a conclusion, instead of a drawback, nanoparticle formation in silane-hydrogen plasmas is considered as a potential for achieving new silicon thin films. The plasma conditions close to powder

---

<sup>1</sup> A. Bouchoule, *Dusty plasmas: physics, chemistry, and technological impacts in plasma processing*, Wiley Press, 1999.

<sup>2</sup> P. Roca i Cabarrocas et al., *J. Vac. Sci. Technol. A*, 14(2):655,1998.

<sup>3</sup> P Roca i Cabarrocas et al., *J. Non. Cryst. Solids*, 227:(871-875),1998.

<sup>4</sup> P Roca i Cabarrocas et al., *J. Non. Cryst. Solids*, 266-269: (31-37), 2000.

<sup>5</sup> Pere Roca i Cabarrocas et al, *Pure Appl. Chem.*, 74(3):359-67,2002.

<sup>6</sup> C Longeaud et al., *J. Non. Cryst. Solids*, 227-230(1):96-99, 1998.

formation and the concentration of clusters and/or nano-crystallites contributing to deposition need to be studied further. Nanoparticles that can be generated in plasmas with controlled size, shape, composition and crystallinity are the main objective of many researchers. However, there is limited success to control nanoparticles' generation. Thus, the modelling studies of nanoparticle formation in plasma are necessary.

In this chapter, a sectional model will be employed to study the nanoparticle formation in SiH<sub>4</sub>-H<sub>2</sub> plasmas. First, an overview is given to show how nanoparticles are formed in the discharge. Second, the dynamic equations of sectional model are presented. Third, a numerical scheme, time-splitting method, is introduced to make this model efficient. The sectional model with time-splitting method is validated. Also, some initial results are presented. In particular, the contribution of nanoparticles to silicon thin films deposition is studied.

## 4.2 An overview of nanoparticle formation

Nanoparticle formation by experiments and modeling has been studied for 30 years. The generation and behavior of nanoparticles in silane-based plasmas was first studied by Bouchoule and Boufendi<sup>7,8,9,10,11,12</sup>. They used 90° laser-light scattering (LLS) of a He-Ne laser as an *in-situ* technique to observe the appearance, growth, and the dynamics of the particles generated in the plasma<sup>6,7</sup>. TEM (transmission electron microscopy) and SEM (scanning electron microscopy) as *ex-situ* techniques were employed to determine the particle size and shape. They also studied the effect of process conditions (such as gas temperature, RF voltage and gas flow rate) on the formation of nanoparticles and determined the parameters leading to the formation of particles in silane-argon plasma. By the experimental observations and measurements on the nanoparticle growth kinetics<sup>8,9,10,11</sup>, they concluded that the formation of dust

---

<sup>7</sup> A. Bouchoule et al., *J. Appl. Phys.*, 70(4):1991–2000,1991.

<sup>8</sup> L. Boufendi et al., *Appl. phys. lett.*, 60(2):169-171, 2021.

<sup>9</sup> A. Bouchoule et al., *Plasma Sources Sci. Technol.*, 2(3):204,1993.

<sup>10</sup> L. Boufendi et al., *Plasma Sources Sci. Technol.*, 3(3):262–67, 1994.

<sup>11</sup> L. Boufendi et al., *J. Appl. Phys.*, 76(1):148–53,1994.

<sup>12</sup> A Bouchoule et al. , *Plasma Sources Sci. Technol.*,3(3):292–301,1994.

follows a three steps process: (1) clusters' formation (about 2nm) with high concentration, up to  $10^9 - 10^{10} \text{ cm}^{-3}$ ; (2) agglomeration resulting in nanoparticles growth up to 50 – 60 nm diameter; (3) surface deposition of  $\text{SiH}_x$  species on the nanoparticles with constant concentration. During the first phase, small crystallites can be produced because of chemical reactions in the plasma. Small crystallites (2 nm) can be observed by dark field TEM. During the second phase, the particles' size increases rapidly and the number density of nanoparticles decreases. TEM pictures show that these nanoparticles have a rough surface. In the third phase, the number density of nanoparticles nearly remains constant and the particles' growth is much slower compared to the second phase. Also, it was observed that the particles' surface is smoother than in the second phase. Bouchoule and Boufendi<sup>8</sup> found that the third phase of nanoparticles' growth is related to the surface growth and coagulation is negligible in this phase. This is because the particles are large and negatively charged. These particles will then begin to repel each other and the collisions between the particles will be greatly reduced. The nanoparticles' formation in silane-based plasma is illustrated in Figure 4.1.

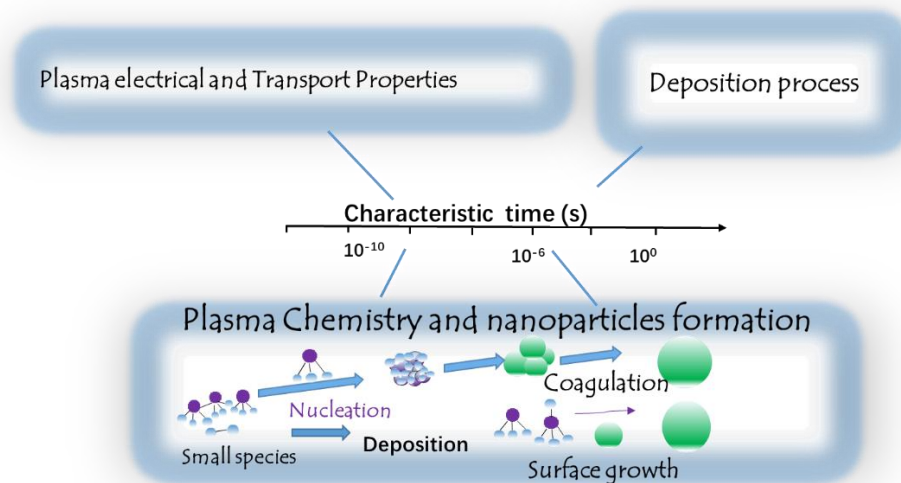


Figure 4.1 Nanoparticles' formation in silane-based plasmas. The purple balls represent the silicon atoms, and the green balls points to the particles.

Although many experimental works can reveal the progress of nanoparticles'

formation, there are still many issues to be addressed, for example, the pathway leading to clusters' formation (the 1st phase) is a contentious issue. Therefore, numerical modelling to further understand the nanoparticles' behavior and formation is essential so that one can optimize the process parameters in experiments in order to acquire the desired thin films. U. V. Bhandarkar<sup>13</sup> *et. al.* developed a model of hydrogenated silicon clusters to study the nucleation of nanoparticles in low-temperature silane plasmas. A quasi-one-dimensional model that combines plasma chemistry with particle growth mechanisms was used to model particle formation in an argon–silane plasma with process conditions similar to the experiments conducted by Boufendi *et al*<sup>9</sup>. From the model, the main pathway leading to the formation of silicon clustering was governed by anion–neutral reactions. It was found that SiH<sub>2</sub> radical insertion is important only in the initial stages of clustering. The increase of ion density induces faster clustering because the formation of reactive radicals increases. U. V. Bhandarkar *et al*<sup>14</sup> also investigated that particle nucleation is delayed with an increase in the temperature by using the clustering model, which reproduces the experimental observations in L. Boufendi's work<sup>9</sup>. They concluded that the temperature dependence of the diffusion coefficient is a strong candidate to explain the observed delay of nucleation. Also, the delay is a combined effect of increasing diffusion losses and reduced particle growth rate when the gas temperature increases. Not only nanoparticle's formation from nucleation to cluster growth can be studied by modelling, but the coagulation, surface growth and particle's charging are also modelled in order to fully understand nanoparticles' behavior in plasmas. K. D. Bleecker *et al*<sup>15,16,17</sup> investigated powder formation (including nucleation, coagulation, surface growth and particles' charging) in silane-based plasmas by developing a 1-D fluid model coupled with an aerosol dynamics model. This model is employed to predict the number density, the charge and

---

<sup>13</sup> U. V. Bhandarkar *et al.*, *J. Phys. D: Appl. Phys.*, 33(21): 2731–46,2000.

<sup>14</sup> U. Bhandarkar *et al.*, *J. Phys. D: Appl. Phys.*, 36(12):1399–1408,2003.

<sup>15</sup> K. de Bleecker *et al.*, Modeling of Dusty Silane Discharges: Nanoparticle Formation, Transport and Charging, In APS Annual Gaseous Electronics Meeting Abstracts (pp. JM1-004).

<sup>16</sup> K. De Bleecker, *New J. Phys.*, 8(9) : 178–178, 2006.

<sup>17</sup> K. De Bleecker *et al.*, *J. Phys. D: Appl. Phys.*, 36(15) :1826–33,2003.

the transport of nanoparticle agglomerates undergoing particle coagulation<sup>15</sup>. In the coagulation block, a sectional approach is used to solve the general dynamic equation for an aerosol by dividing the nanoparticle domain in 78 volume sections, covering nanoparticle range from about 0.8 nm to 50 nm in diameter. For every step in the coagulation module, the effect of particle charging and external forces such as the electrostatic force, ion drag force, and thermophoresis on the transport and behavior of nanoparticles is included and addressed with the same temporal resolution. They found<sup>18</sup> that the charge of nanoparticles is very sensitive to changes in particle size and local plasma conditions. The minimum charge was obtained in the bulk plasma region. An increase in electron attachment was observed in the sheath region, which maximizes the charge of the nanoparticles, resulting in an electrostatic potential barrier that effectively traps negatively charged particles. Finally, they studied the effect of thermophoresis force, arising from a thermal gradient in gas temperature induced by heating or cooling of the electrodes, on the spatial distribution of nanoparticles density profiles<sup>19</sup>. They concluded that the nanoparticles are shifted towards the electrode with lower temperature when the temperature difference between two electrodes is applied.

In the present study, we are interested in the  $\alpha \rightarrow \gamma$  transition in SiH<sub>4</sub>-H<sub>2</sub> plasma, as showed in Figure 4.2. Indeed, this regime corresponds to improved deposition rate and material quality, and both the deposition of so-called “polymorphous” silicon and epitaxy of crystalline silicon are achieved under such conditions. In this regime, the nanoparticle size remains generally below 10 nm, which current experimental techniques cannot detect easily. Also, it is not easy to measure the nanoparticles density and the size distribution profile in the plasma. Therefore, numerical modelling has an advantage to give a clear description for the formation and behavior of nanoparticles in SiH<sub>4</sub>-H<sub>2</sub> plasmas.

---

<sup>18</sup> K. De Bleecker et al., *Phys. Rev. E*, 70(5):056407,2004.

<sup>19</sup> K. De Bleecker et al., *Phys. Rev. E*, 71(6): 066405, 2005.

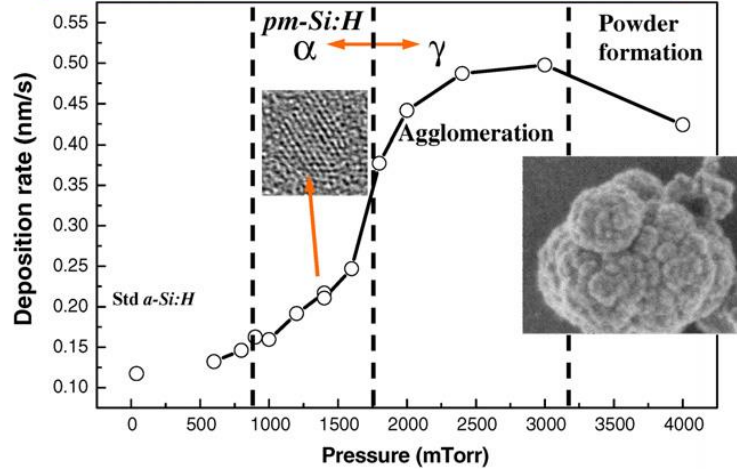


Figure 4.2 – Schematic representation of powder formation in silane-hydrogen plasmas<sup>20</sup>.

## 4.3 Sectional model

### 4.3.1 General Dynamic Equation

In this chapter, the pristine plasma software presented in Chapter 2 has been coupled with a sectional model, which takes into account nucleation, coagulation, surface growth, charging and transport of nanoparticles. The sectional model divides nanoparticles into sections with given size and charge, following the method of Girshick and coworkers<sup>21, 22</sup>. In particular, the influence of image potential and electrostatic interaction between charged particles are taken into account in the coagulation module. The complete dusty plasma model is illustrated in Figure 4.3.

The general dynamic equation for nanoparticles is described below:

$$\frac{\partial N_{pc}}{\partial t} + \partial_x \cdot (N_{pc} \vec{V}_{pc}) = \left[ \frac{\partial N_{pc}}{\partial t} \right]_{\text{nuc}} + \left[ \frac{\partial N_{pc}}{\partial t} \right]_{\text{growth}} + \left[ \frac{\partial N_{pc}}{\partial t} \right]_{\text{coag}} + \left[ \frac{\partial N_{pc}}{\partial t} \right]_{\text{charge}} \quad (4.3.1)$$

Where  $N_{pc}$  denotes the density of nanoparticles in size section  $p$  and charge  $c$ ,  $p = 1, \dots, N_p$  and  $c = -K_-, \dots, K_+$ .  $\vec{V}_{pc}$  is the average diffusion velocity of nanoparticles in section  $p$  with charge  $c$ . The source terms on the right hand side,  $\left[ \frac{\partial N_{pc}}{\partial t} \right]_{\text{nuc}}$ ,  $\left[ \frac{\partial N_{pc}}{\partial t} \right]_{\text{growth}}$ ,  $\left[ \frac{\partial N_{pc}}{\partial t} \right]_{\text{coag}}$ ,  $\left[ \frac{\partial N_{pc}}{\partial t} \right]_{\text{charge}}$  represent nucleation, coagulation, surface growth and charging process of nanoparticles.

<sup>20</sup> P. Roca i Cabarrocas et al., *J. Phys. D: Appl. Phys.*, 40(8): 2258–66, 2007.

<sup>21</sup> S. J. Warthesen, *Plasma Chem. Plasma Process.*, 27(3): 292–310, 2007.

<sup>22</sup> P. Agarwal et al., *Plasma Sources Sci. Technol.*, 21(5): 055023, 2012.

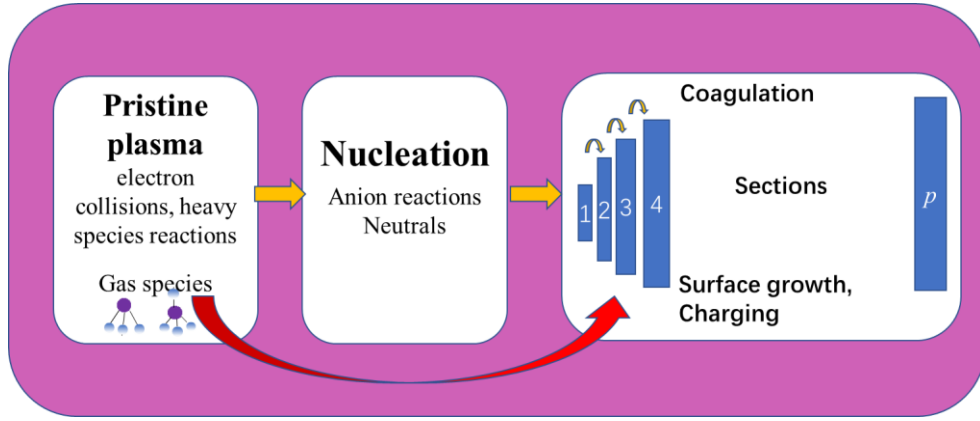


Figure 4.3 Overview of dusty plasma model.

In each section, the evolution equation for the densities of nanoparticles is solved<sup>23</sup>:

$$N_{pc}(t, \mathbf{x}) = \int_{v_{p-1}}^{v_p} n_c(t, \mathbf{x}, v) dv = \eta_{pc}(t, \mathbf{x}) \ln \left( \frac{v_p}{v_{p-1}} \right), 1 \leq p \leq N_p, -K_- \leq c \leq K_+ \quad (4.3.2)$$

Where  $v$  is the volume of the particle,  $n_c(t, \mathbf{x}, v)$  denotes the continuous distribution function of particles with charge number  $c$ . The volume between two subsequent sections are geometrically spaced:  $v_p = f v_{p-1}$ , where  $f$  is the volume factor in order to proceed to the next section,  $f > 1$ . The particle volume density in each section is assumed to be constant:

$$v n_c(t, \mathbf{x}, v) = \eta_{pc}(t, \mathbf{x}), v \in [v_{p-1}, v_p] \quad (4.3.3)$$

The volume of nanoparticles in each section can be written as:

$$V_{pc}(t, \mathbf{x}) = \int_{v_{p-1}}^{v_p} v n_c(t, \mathbf{x}, v) dv = \eta_{pc}(t, \mathbf{x}) (v_p - v_{p-1}), 1 \leq p \leq N_p, -K_- \leq c \leq K_+ \quad (4.3.4)$$

The nanoparticle's density also can be written as

$$N_{pc}(t, \mathbf{x}) = \frac{V_{pc}(t, \mathbf{x})}{\bar{v}_p}, 1 \leq p \leq N_p, -K_- \leq c \leq K_+ \quad (4.3.5)$$

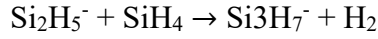
Where  $\bar{v}_p$  is the average volume of particle in section  $p$ :

$$\bar{v}_p = \frac{v_p - v_{p-1}}{\ln \left( \frac{v_p}{v_{p-1}} \right)}, 1 \leq p \leq N_p \quad (4.3.6)$$

<sup>23</sup> Jean-Maxime Orlac'h, Modeling of a Silane-Hydrogen Plasma Discharge Including Nanoparticle Dynamics for Photovoltaic Applications, These de doctorat, Université Paris-Saclay (ComUE), 2017.

### 4.3.2 Nucleation

The main pathway of nanoparticle nucleation is from anion reactions<sup>12,14</sup>. In this model, the nucleation rate is equivalent to the production rate of  $\text{Si}_3\text{H}_x^-$  negative ions, which are produced from the clustering reactions below:



The nucleation rate of nanoparticles  $\left[\frac{\partial N_{pc}}{\partial t}\right]_{\text{nuc}}$  is calculated as:

$$\left[\frac{\partial N_{pc}}{\partial t}\right]_{\text{nuc}} = \delta_{p1}\delta_{c(-1)}(k_{\text{nuc}}n_{\text{H}_3\text{SiSiH}^-}n_{\text{SiH}_4} + k_{\text{nuc}}n_{\text{Si}_2\text{H}_5^-}n_{\text{SiH}_4}) \quad (4.3.7)$$

where  $k_{\text{nuc}} = 1.0 \times 10^{-12} \text{cm}^3 \cdot \text{s}^{-1}$  is the reaction rate constant of these reactions. The formed nanoparticles belong to the section with size  $p = 1$  and charge  $c = -1$ .

### 4.3.3 Coagulation

The collision kernel is defined in order to calculate the coagulation rate. The collision rate of particles of volume  $u$  colliding with particles of volume  $v$  is given by:

$$\beta(u, v) = \varphi \left(\frac{3}{4\pi}\right)^{\frac{1}{6}} \left(\frac{6k_B T}{\rho_P}\right)^{\frac{1}{2}} \left(\frac{1}{u} + \frac{1}{v}\right)^{\frac{1}{2}} \left(u^{\frac{1}{3}} + v^{\frac{1}{3}}\right)^2 \quad (4.3.8)$$

Where  $T$  is the gas temperature,  $\rho_P$  is the particle volume density. For silicon nanoparticles<sup>14</sup>, the volume density is  $\rho_P = 2.3 \text{kg} \cdot \text{m}^{-3}$ .  $\varphi$  is the collision enhancement due to particles being charged.  $\varphi = \varphi(c_1, c_2, r_1, r_2)$ , where  $r_1, r_2$  represent the radius of nanoparticles with volumes  $u$  and  $v$ , the radius  $r$  can be written as  $r(u) = \left(\frac{3u}{4\pi}\right)^{\frac{1}{3}}$  generally. The equation (4.3.8) can be achieved from the kinetic theory of gases for rigid spherical molecules<sup>24,25</sup>. The collision enhancement  $\varphi$  can be written as<sup>26,27</sup>:

<sup>24</sup> S. Chapman et al., The mathematical theory of non-uniform gases: an account of the kinetic theory of viscosity, thermal conduction and diffusion in gases. *Cambridge university press*, 1991.

<sup>25</sup> S. K. Friedlander, Smoke, Dust, and Haze: Fundamentals of Aerosol Dynamics *Oxford University Press*, 2000.

<sup>26</sup> U. Kortshagen et al., *Phys. Rev. E*, 60(1):887–98, 1999.

<sup>27</sup> P. Agarwal et al., *Plasma Sources Sci. Technol.*, 21(5): 055023, 2012.

$$\varphi(c_1, c_2, r_1, r_2) = \begin{cases} 1, & c_1 = c_2 = 0 \\ 1 - \frac{c_1 c_2}{4\pi\epsilon_0(r_1+r_2)k_B T_h}, & c_1 c_2 < 0 \\ \exp\left(-\frac{c_1 c_2}{4\pi\epsilon_0(r_1+r_2)k_B T_h}\right), & c_1 c_2 > 0 \\ \mathcal{E}(c_1, r_1, r_2), & c_2 = 0, c_1 \neq 0 \end{cases} \quad (4.3.9)$$

where  $\mathcal{E}(c_1, r_1, r_2)$  is the enhancement in the collision rate between neutral and charged particle because of image potentials, which is detailed in the reference<sup>28</sup>. Here, the image potential can be written as follows:

$$E_{\text{image}} = \frac{1}{2} \int_0^1 \frac{1}{x^2} \frac{d}{dx} \left( x \frac{d\Phi(x)}{dx} \right) \times \exp\left(\frac{x}{2} \frac{d\Phi(x)}{dx} - \Phi(x)\right) dx + \exp\left(\frac{1}{2} \frac{d\Phi(x)}{dx} \Big|_{x=1} - \Phi(1)\right), \quad (4.3.10)$$

$$x = \frac{r_1+r_2}{r}, \quad (4.3.11)$$

where  $r$  denotes the distance between the nanoparticles and  $\Phi(x)$  represents the inter-particle potential. In case of SiH<sub>4</sub>-H<sub>2</sub> plasma with formation of nanoparticles, the main source of coagulation between neutral and charged particles is from coagulation between very small neutral particles and larger charged particles<sup>29</sup>. In this case,  $\Phi(x)$  is written as:

$$\Phi(x) = \frac{aMx^2}{2(1-bx^2)}, \quad (4.3.12)$$

$$M = \frac{e^2}{4\pi\epsilon_0 k_B T (r_1+r_2)^2}, \quad (4.3.13)$$

$$a = \frac{\epsilon-1}{\epsilon+1} Z_1^2 \left(1 - \frac{r_1}{r_1+r_2}\right), \quad (4.3.14)$$

$$b = \left(\frac{\epsilon-1}{\epsilon+1}\right)^2 \left(\frac{r_1}{r_1+r_2}\right) \left(1 - \frac{r_1}{r_1+r_2}\right), \quad (4.3.15)$$

where,  $\epsilon$  is the dielectric constant of the nanoparticles.

The coagulation rate of two nanoparticles with volumes  $u$  and  $v$  is written as:

$$\left[\frac{dN}{dt}\right]_{\text{Coag}} = \iint n_u n_v \beta(u, v) du dv \quad (4.3.16)$$

where  $n_u$  and  $n_v$  are the size distribution functions for  $u$  and  $v$  volumes.

In this model, since we are trying to keep the volume (mass) flow rate constant, for each section the mass flow rate into and out of any given section  $p$  are calculated.

Several situations need to be considered. (1) The mass flow rate into section  $p$  will be

<sup>28</sup> D. D. Huang et al., *J. Colloid Interface Sci.*, 141(1): 191–98, 1991.

<sup>29</sup> L. Ravi et al., *Phys. Rev. E*, 79(2): 026408, 2009.

given by those coagulation events whose size is less than or equal to this section, and whose volume ends up in the size interval of section  $p$ . Noting this, the mass flow rate into section  $p$  for nanoparticles whose volumes are smaller than those in this section is followed by:

$$\frac{1}{2} \int_{v_0}^{v_{p-1}} \int_{v_0}^{v_{p-1}} \theta(v_{p-1} < u + v < v_p) (u + v) \beta(u, v) n(u, t) n(v, t) dudv \quad (4.3.17)$$

where the  $1/2$  is used to avoid the double calculations.  $\theta$  is a step function indicating that the sum of the volumes  $u$  and  $v$  falls within the interval of the section  $p$ . Each time two nanoparticles with volume  $u$  and  $v$  coagulate into section  $p$ , the sum of both volumes,  $u + v$ , is necessarily added to the section to conserve volume(mass).

(2) coagulation of nanoparticles with section  $p$  with lower sections that can have volumes that still lie in the section  $p$ . In this case, the mass flow rate is given by:

$$\int_{v_0}^{v_{p-1}} \int_{v_{p-1}}^{v_p} \theta(u + v < v_p) v \beta(u, v) n(u, t) n(v, t) dudv \quad (4.3.18)$$

In this situation, only  $v$  is included to the integrand since volume  $u$  was already in the section  $p$ .

(3) nanoparticles that leaves the volume interval in the section  $p$  is considered as the loss of the section  $p$ :

$$\int_{v_0}^{v_{p-1}} \int_{v_{p-1}}^{v_p} \theta(u + v > v_p) u \beta(u, v) n(u, t) n(v, t) dudv \quad (4.3.19)$$

where  $u$  is the volume(mass) coming to a higher section. If the volume factor  $f$  is larger than 2, then two nanoparticles with volumes lie in the same section will produce a nanoparticle in the same section.

(4) However, if the volume factor  $f$  is smaller than 2, the coagulation of two nanoparticles with volumes in the same section will produce a nanoparticle of a higher section:

$$\frac{1}{2} \int_{v_{p-1}}^{v_p} \int_{v_{p-1}}^{v_p} \theta(u + v > v_p) (u + v) \beta(u, v) n(u, t) n(v, t) dudv \quad (4.3.20)$$

(5) the coagulation of nanoparticle of section  $p$  with any other nanoparticle with larger section will leave section  $p$ :

$$\int_{v_{p-1}}^{v_p} \int_{v_p}^{v_m} u \beta(u, v) n(u, t) n(v, t) dudv \quad (4.3.21)$$

As a result, one can have the mass flow rates for section  $p$ :

$$\begin{aligned}
\frac{dQ_p}{dt} = & \frac{1}{2} \int_{v_0}^{v_{p-1}} \int_{v_0}^{v_{p-1}} \theta(v_{p-1} < u + v < v_p) (u + v) \beta(u, v) n(u, t) n(v, t) dudv \\
& + \int_{v_0}^{v_{p-1}} \int_{v_{p-1}}^{v_p} \theta(u + v < v_p) v \beta(u, v) n(u, t) n(v, t) dudv \\
& - \int_{v_0}^{v_{p-1}} \int_{v_{p-1}}^{v_p} \theta(u + v > v_p) u \beta(u, v) n(u, t) n(v, t) dudv \\
& - \frac{1}{2} \int_{v_{p-1}}^{v_p} \int_{v_{p-1}}^{v_p} \theta(u + v > v_p) (u + v) \beta(u, v) n(u, t) n(v, t) dudv \\
& - \int_{v_{p-1}}^{v_p} \int_{v_p}^{v_m} u \beta(u, v) n(u, t) n(v, t) dudv
\end{aligned} \tag{4.3.22}$$

In order to arrive at the coagulation rate, the volume rate  $\frac{dQ_p}{dt}$  must be divided by the average volume of section  $p$ , which is written as:

$$\begin{aligned}
\frac{dN_p}{dt} = & \frac{1}{2} \int_{v_0}^{v_{p-1}} \int_{v_0}^{v_{p-1}} \theta(v_{p-1} < u + v < v_p) \beta(u, v) n(u, t) n(v, t) dudv \\
& + \int_{v_0}^{v_{p-1}} \int_{v_{p-1}}^{v_p} \theta(u + v < v_p) \beta(u, v) n(u, t) n(v, t) dudv \\
& - \int_{v_0}^{v_{p-1}} \int_{v_{p-1}}^{v_p} \theta(u + v > v_p) \beta(u, v) n(u, t) n(v, t) dudv \\
& - \frac{1}{2} \int_{v_{p-1}}^{v_p} \int_{v_{p-1}}^{v_p} \theta(u + v > v_p) \beta(u, v) n(u, t) n(v, t) dudv \\
& - \int_{v_{p-1}}^{v_p} \int_{v_p}^{v_m} \beta(u, v) n(u, t) n(v, t) dudv
\end{aligned} \tag{4.3.23}$$

In order to obtain the contribution of the various sections to  $\left[ \frac{\partial N_{pc}}{\partial t} \right]_{coag}$ , one needs to sum the integrals over each section. Here, we consider the coagulation events of the situations required. Noting that the detailed equations for the representation of coagulation terms are skipped since it is lengthy, one can find the detailed description in the references<sup>30,31</sup>.

#### 4.3.4 Surface growth

In this section we deal with nanoparticle growth due to surface reactions. There are two situations we need to consider: first the nanoparticles grow but still remain in the same section; second the particles grow and move to the higher section. Therefore, the  $k$ th section can be conserved due to the increase of surface growth of nanoparticles that remain in the section and the influx of the volume of nanoparticles moving into the  $k$ th section from the previous section. Also, the  $k$ th section can be conserved due to the decrease of nanoparticle surface growth from section  $k$  to  $k+1$ . Nevertheless, surface growth of nanoparticles is a number conserving phenomenon, since the particles do not

<sup>30</sup> F. Gelbard et al., *J. Colloid Interface Sci.*, 76(2):541–56, 1980.

<sup>31</sup> Y. P. Kim et al., *J. Colloid Interface Sci.*, 135(1): 185–99, 1990.

increase in number, but just grow in size. Thus, the nanoparticle growth between sections is also simulated so as to conserve number. The number conserving scheme was developed by Warren and Seinfeld<sup>32</sup> for nanoparticles experiencing simultaneous coagulation and surface growth. The nanoparticle surface growth term can be written as:

$$\left[ \frac{\partial N_{pc}}{\partial t} \right]_{\text{growth}} = \frac{\bar{v}_{p-1}}{\bar{v}_p - \bar{v}_{p-1}} \bar{H}_{p-1c} N_{p-1c} - \frac{\bar{v}_p}{\bar{v}_{p+1} - \bar{v}_p} \bar{H}_{pc} N_{pc} \quad (4.3.24)$$

Where  $\bar{H}_{pc}$  is the intra-sectional growth rate, and reads

$$\bar{H}_{pc}(t) = \left( \sum_{l \in \mathcal{C}} \hat{\omega}_{pc}^l V_m^{\text{Si}} \nu_{\text{Si}}^l \right) \frac{\bar{s}_p}{\bar{v}_p} \quad (4.3.25)$$

where  $\hat{\omega}_{pc}^l$  is the average molar surface flux of the  $l^{\text{th}}$  gas species coming to the nanoparticle with size  $p$  and charge  $c$ ,  $V_m^{\text{Si}}$  is the molar volume of silicon,  $\nu_{\text{Si}}^l$  is the average number of silicon atoms of  $l^{\text{th}}$  species depositing on the nanoparticles and  $\bar{s}_p$  is the average surface of nanoparticles with size  $p$ , which is written as:

$$\bar{s}_p = \frac{3}{2} \pi^{1/3} 6^{2/3} \frac{v_p^{2/3} - v_{p-1}^{2/3}}{\ln\left(\frac{v_p}{v_{p-1}}\right)} \quad (4.3.26)$$

The average molar surface flux  $\hat{\omega}_{pc}^l$  of the  $l^{\text{th}}$  gas species coming to the nanoparticle with size  $p$  and charge  $c$  depends on the respective charges of nanoparticles and gas species. There are several cases to calculate this term:

(1) Neutral species depositing on a neutral particle,  $c_c = c_l = 0$ . In this case, the average molar surface flux is equivalent to the thermal flux<sup>23</sup>:

$$\hat{\omega}_{pc}^l = \frac{1}{4} \sigma_{pc}^l \gamma_l v_{\text{th},l} \quad (4.3.27)$$

Where  $\sigma_{pc}^l$  is the sticking coefficient of  $l^{\text{th}}$  gas species on a nanoparticle with size  $p$  and charge  $c$ ,  $\gamma_l$  is the molar concentration of  $l^{\text{th}}$  species,  $v_{\text{th},l}$  is the thermal velocity of the  $l^{\text{th}}$  species, which has a form:

$$v_{\text{th},l} = \left( \frac{8RT_l}{\pi W_l} \right)^{\frac{1}{2}}, l \in \mathcal{C} \quad (4.3.28)$$

(2) Neutral species depositing on a charged particle,  $c_c \neq 0, c_l = 0$ ,  $\hat{\omega}_{pc}^l$  has the same

<sup>32</sup> D. R. Warren et al., *Aerosol Sci. Technol.*, 4(1): 31–43, 1985.

form as in case (1).

- (3) Charged species depositing on a charged particle with opposite signs,  $c_c c_l < 0$ ,  $\hat{\omega}_{pc}^l$  is written as:

$$\hat{\omega}_{pc}^l = \frac{1}{4} \gamma_l \bar{v}_l \left( 1 - 2 \frac{c_c c_l}{4\pi \epsilon_0 \bar{r}_p W_l \bar{v}_l^2} \right) \quad (4.3.29)$$

where  $\bar{v}_l$  is an average macroscopic velocity of  $l^{\text{th}}$  species, written as<sup>15</sup>:

$$\bar{v}_l = \left( v_l^2 + (2v_{\text{th},l})^2 \right)^{\frac{1}{2}} \quad (4.3.30)$$

- (4) a charged species depositing on a charged nanoparticle with the same sign,  $c_c c_l > 0$ , then  $\hat{\omega}_{pc}^l$  is written as:

$$\hat{\omega}_{pc}^l = \frac{1}{4} \gamma_l \bar{v}_l \exp \left( -2 \frac{c_c c_l}{4\pi \epsilon_0 \bar{r}_p W_l \bar{v}_l^2} \right) \quad (4.3.31)$$

- (5) an ion species depositing on a neutral nanoparticle.  $c_c = 0$  and  $c_l \neq 0$ , then  $\hat{\omega}_{pc}^l$  is calculated based on ‘OML’ theory (Orbital Motion Limited)<sup>33,34</sup>, written as:

$$\hat{\omega}_{pc}^l = \frac{1}{4} \gamma_l \bar{v}_l \quad (4.3.32)$$

### 4.3.5 Charge fluctuations rate

The charging fluctuation rate is generally written in the form:

$$\left[ \frac{\partial N_{pc}}{\partial t} \right]_{\text{charge}} = v_{p,c+1}^e N_{p,c+1} + \sum_{l \in Z^-} v_{p,c+1}^l N_{p,c+1} + \sum_{l \in Z^+} v_{p,c-1}^l N_{p,c-1} - v_{pc}^e N_{pc} - \sum_{l \in Z^-} v_{pc}^l N_{pc} - \sum_{l \in Z^+} v_{pc}^l N_{pc} \quad (4.3.33)$$

Where  $Z^-$  and  $Z^+$  represents the groups of negative and positive ions respectively.  $v_{pc}^e$  and  $v_{pc}^l$  are the electron and ion attachment frequencies to the nanoparticle with size  $p$  and charge  $c$ . It is assumed that the charging process of nanoparticles is only due to ions and electron attachment, while other charging processes, such as UV photodetachment and secondary electron emission are not considered. In the model,  $v_{pc}^l$  is written as:

$$v_{pc}^l = 4\pi \bar{r}_p^2 \mathcal{N}_A \hat{\omega}_{pc}^l \quad (4.3.34)$$

Where  $\hat{\omega}_{pc}^l$  is the average molar surface flux of the  $l^{\text{th}}$  gas species coming to the nanoparticle with size  $p$  and charge  $c$ . The charge fluctuation of nanoparticles by ion

<sup>33</sup> V. A. Schweigert et al., *J. Phys. D: Appl. Phys.*, 29(3):655–59,1996.

<sup>34</sup> T. Matsoukas et al., *J. Vac. Sci. Technol. A*, 14(2): 624–30,1996.

and electron collisions in the nanometer size range can be described by the orbital motion limited (OML) probe theory<sup>31,32</sup>.

#### 4.3.6 Forces acting on the nanoparticles

It is known that external forces have a big impact on the transport of nanoparticles in the discharge. In this model, the external forces acting on the nanoparticles include gravity, ion drag force and electric drift force. The thermophoresis force arising from the thermal gradient induced by different electrode temperatures is neglected in the thesis since we are focusing on the cases of uniform temperature. The gravity force is written as:

$$\vec{F}_{pc}^{\text{grav}} = \frac{4}{3}\pi\bar{r}_p^3\rho_p\vec{g} \quad (4.3.35)$$

where  $\vec{g}$  denotes the gravity vector and  $\rho_p$  represents the volume density of silicon nanoparticles. The electric drift force is given by:

$$\vec{F}_{pc}^{\text{drift}} = q_c\vec{E}_{\text{eff}} \quad (4.3.36)$$

where  $q_c$  denotes the charge of nanoparticles, and  $\vec{E}_{\text{eff}}$  is the effective electric field acting on the nanoparticles, the detailed equations to solve the effective electric field are described in the section of numerical scheme. The ion drag force, based on the ‘‘OML’’ theory<sup>31,32</sup>, consists of a collection force and an orbital force:

$$\vec{F}_{pc}^{\text{ion}} = \vec{F}_{pc}^{\text{coll}} + \vec{F}_{pc}^{\text{orb}} \quad (4.3.37)$$

The collection force explains the momentum transfer attributed to the collected ions by nanoparticles with size  $p$  and charge  $c$ , which is written as<sup>35</sup>:

$$\vec{F}_{pc}^{\text{coll}} = \sum_{l \in Z} \pi b_c^2 \bar{v}_l n_l W_l \vec{v}_l \quad (4.3.38)$$

Where  $Z$  denotes the group of ions,  $\bar{v}_l$  is the mean speed of collected ions,  $b_c$  is the collection parameter, written as:

---

<sup>35</sup> M. S. Barnes et al., *Phys. Rev. Lett.*, 68(3): 313–16,1992.

$$b_c^2 = \begin{cases} \bar{r}_p^2 \left[ 1 - \frac{2c_c c_l}{4\pi\epsilon_0 \bar{r}_p W_l \bar{v}_l^2} \right], & c_c c_l < 0 \\ \bar{r}_p^2 \exp \left[ -\frac{2c_c c_l}{4\pi\epsilon_0 \bar{r}_p W_l \bar{v}_l^2} \right], & c_c c_l > 0 \\ \bar{r}_p^2, & c_c = 0 \end{cases} \quad (4.3.39)$$

The orbital force accounts for the momentum transfer due to deflected ions via Coulomb interactions with the impact parameter  $b_{\pi/2}$  for  $90^\circ$  deflection, which is written as:

$$\vec{F}_{pc}^{\text{orb}} = \sum_{l \in \mathcal{Z}} 4\pi b_{\pi/2}^2 \Gamma_G \bar{v}_l n_l W_l \vec{v}_l \quad (4.3.40)$$

Where  $b_{\pi/2}$  is written as:

$$b_{\pi/2} = \bar{r}_p \left( -\frac{c_c c_l}{4\pi\epsilon_0 \bar{r}_p W_l \bar{v}_l^2} \right) \quad (4.3.41)$$

and  $\Gamma_G$  is the Coulomb logarithm integrated from  $b_c$  to  $\lambda_D$ , written as

$$\Gamma_G = \frac{1}{2} \ln \left( \frac{\lambda_D^2 + b_{\pi/2}^2}{b_c^2 + b_{\pi/2}^2} \right) \quad (4.3.42)$$

Where  $\lambda_D$  is the linearized Debye length, written as:

$$\frac{1}{\lambda_D^2} = \frac{1}{\lambda_e^2} + \frac{1}{\lambda_l^2} \quad (4.3.43)$$

Where  $\lambda_e$  and  $\lambda_l$  are the electron and ion Debye lengths:

$$\begin{aligned} \lambda_e &= \left( \frac{\epsilon_0 k_B T_e}{n_e q_e^2} \right)^{\frac{1}{2}} \\ \lambda_l &= \left( \frac{\epsilon_0 W_l \bar{v}_l^2}{n_l q_l^2} \right)^{\frac{1}{2}}, l \in \mathcal{Z} \end{aligned} \quad (4.3.44)$$

As a conclusion, the total force acting on nanoparticles with size  $p$  and charge  $c$  is:

$$\vec{F}_{pc}^{\text{ext}} = \vec{F}_{pc}^{\text{grav}} + \vec{F}_{pc}^{\text{ion}} + \vec{F}_{pc}^{\text{drift}} \quad (4.3.45)$$

#### 4.3.6 Nanoparticle transport

The classic drift-diffusion approximation applied for pristine plasma is also used for nanoparticles transport<sup>23</sup>. The sectional velocity for nanoparticles is written in the form<sup>36,37</sup>:

$$N_{pc} \vec{V}_{pc} = \frac{1}{f_{pc}} \vec{F}_{pc}^{\text{ext}} - D_{pc} \mathbf{\partial}_x N_{pc} \quad (4.3.46)$$

<sup>36</sup> S. Chandrasekhar et al., *Rev. Mod. Phys.*, 15(1): 1–89,1943.

<sup>37</sup> M. R. Akdim et al., *J. Appl. Phys.*,94(1): 104–9,2003.

where  $\vec{F}_{pc}^{\text{ext}}$  is the sum over all external forces on the nanoparticles with size  $p$  and charge  $c$ ,  $f_{pc}$  is the friction coefficient of nanoparticles, and  $D_{pc}$  denotes their diffusion coefficient, which is given by Stokes-Einstein expression, namely:

$$D_{pc} = \frac{k_B T_h}{f_{pc}} \quad (4.3.47)$$

For the friction coefficient of nanoparticles, when the particle diameter is much smaller than its mean free path,  $f_{pc}$ , is written based on the Epstein's law<sup>38</sup> as:

$$f_{pc} = \frac{4}{3} \pi \bar{r}_p^2 n \sqrt{\frac{8k_B T \bar{W}}{\pi}} \left(1 + \frac{\pi\alpha}{8}\right) \quad (4.3.48)$$

where  $n$  is the density of gas species,  $\bar{W}$  is the mean molar mass of the gas mixture, written as:

$$\frac{1}{\bar{W}} = \sum_{l \in C} \frac{Y_l}{W_l} \quad (4.3.49)$$

$\alpha$  is the adjustment factor, which represents the fraction of gas molecules leaving the surface in equilibrium with the surface, and the rest of the fraction  $1-\alpha$  is reflected by the surface.

## 4.4 Coupled 1-D fluid-sectional model

The coupled 1-D fluid-sectional model is used to describe the evolution of gas species density, nanoparticle's density, electron temperature and electrical potential in SiH<sub>4</sub>-H<sub>2</sub> dusty plasmas. The continuity equation (2.4.1), electron energy equation (2.4.4) and Poisson equation (2.4.5) are modified, the equations of fluid velocity are copied, and the dynamic equation for nanoparticles density are solved. Therefore, the equations for the coupled 1-D fluid-sectional model are written as:

$$\partial_t(\rho Y_k) + \partial_x \cdot (\rho Y_k w + \rho Y_k \vec{V}_k) = W_k \omega_k - \sum_{p=1}^{N_p} \sum_{c=-K_-}^{K_+} W_k \Omega_{pc}^k, k \in C, \quad (4.4.1)$$

$$\partial_x^2 \varphi = -\frac{nq_l}{\varepsilon_0} - \sum_{p=1}^{N_p} \sum_{c=-K_-}^{K_+} \frac{N_{pc} c c}{\varepsilon_0}, \quad (4.4.2)$$

$$\partial_t \left( \frac{3}{2} n_e k_B T_e \right) + \partial_x \cdot \vec{Q}_e = n_e q_e V_e \vec{E} + \dot{E}_{eh} - \sum_{p=1}^{N_p} \sum_{c=-K_-}^{K_+} \dot{E}_{pc}^e, \quad (4.4.3)$$

$$\partial_t \rho + 2\rho \alpha \tilde{u} + \partial_z \tilde{v} = 0 \quad (4.4.4)$$

$$\rho \partial_t \tilde{u} + \tilde{v} \partial_z \tilde{u} = \alpha(\rho^{\text{in}} - \rho \tilde{u}^2) + \partial_z(\eta \partial_z \tilde{u}) \quad (4.4.5)$$

<sup>38</sup> P. S. Epstein, *Phys. Rev.*,23(6): 710–33,1924.

$$\begin{aligned} & \frac{\partial N_{pc}}{\partial t} + \partial_x \cdot (N_{pc} \vec{V}_{pc}) \\ &= \left[ \frac{\partial N_{pc}}{\partial t} \right]_{\text{nuc}} + \left[ \frac{\partial N_{pc}}{\partial t} \right]_{\text{growth}} + \left[ \frac{\partial N_{pc}}{\partial t} \right]_{\text{coag}} + \left[ \frac{\partial N_{pc}}{\partial t} \right]_{\text{charge}} \end{aligned} \quad (4.4.6)$$

In Eq. (4.4.1),  $\mathcal{L}_{pc}^k$  denotes the loss term of  $k^{\text{th}}$  species depositing on the nanoparticles with size  $p$  and charge  $c^{39}$ , which is written as:

$$\mathcal{L}_{pc}^k = v_{pc}^k N_{pc}, k \in \mathbb{C}, 1 \leq p \leq N_p, -K_- \leq c \leq K_+ \quad (4.4.7)$$

Then we denote  $Rloss = \sum_{p=1}^{N_p} \sum_{c=-K_-}^{K_+} W_k \mathcal{L}_{pc}^k$ .

In Eq. (4.4.2), charged nanoparticles are considered in Poisson equation. The contribution to the plasma potential is denoted as  $Ploss = \sum_{p=1}^{N_p} \sum_{c=-K_-}^{K_+} \frac{N_{pc} q_c}{\epsilon_0}$ . Also in Eq. (4.4.3), the electron energy loss attributed to collisions with nanoparticles is considered, which is written as<sup>37</sup>:

$$\Delta E_{pc}^e = -\frac{q_c q_e}{4\pi \epsilon_0 \bar{r}_p} \mathcal{L}_{pc} \quad (4.4.8)$$

Then the contribution of nanoparticles to the electron temperature is denoted  $Eloss = \sum_{p=1}^{N_p} \sum_{c=-K_-}^{K_+} \dot{E}_{pc}^e$ . The boundary conditions for Eq. (4.4.3) – Eq. (4.4.5) have been given in section 2.8, which correspond to gas species, electric potential and electron temperature. For nanoparticles (Eq. (4.4.6)), the boundary conditions depend on the nanoparticle's charge. For negative charged particles, since they are confined in the plasma bulk, the density at both electrodes is considered set to zero:

$$\begin{aligned} N_{pc} \Big|_{t,0} &= 0, 1 \leq p \leq N_p, -K_- \leq c \leq -1 \\ N_{pc} \Big|_{t,L} &= 0, 1 \leq p \leq N_p, -K_- \leq c \leq -1 \end{aligned} \quad (4.4.9)$$

For positive and neutral particles, the density gradients at both electrodes are set to zero:

$$\begin{aligned} (\partial_x N_{pc} \cdot \vec{n}) \Big|_{t,0} &= 0, 1 \leq p \leq N_p, 0 \leq c \leq K_+ \\ (\partial_x N_{pc} \cdot \vec{n}) \Big|_{t,L} &= 0, 1 \leq p \leq N_p, 0 \leq c \leq K_+ \end{aligned} \quad (4.4.10)$$

Where  $\vec{n}$  represents the unit vector pointing to the electrodes.

## 4.5 Numerical implementation

Alike the numerical method of chapter 2, the spatial discretization of the equations

<sup>39</sup> S. J. Warthesen, Numerical investigations of nanodusty plasmas, Ph.D. thesis, 2006.

(4.4.1) - (4.4.6) is obtained by applying a three-point finite difference scheme. The drift-diffusion equations for species mass fractions and electron temperature are dealt with Scharfetter-Gummel discretization scheme<sup>40,41</sup>. The time derivatives of Equations (4.4.1), (4.4.3) and (4.4.6) are discretized in a fully implicit manner and solved by Newton method using a Euler predictor<sup>42</sup>.

However, the fully coupled model is very time-consuming. In order to increase the efficiency of current nanoparticle coupled with fluid model, we apply a time-splitting method.

#### 4.5.1 Time-splitting method

In general, the equations required to be solved are divided into two blocks, a fast and a slow block. It is assumed that charged species are in the fast block and nanoparticles are in the slow block. In principle, the fast block runs with time step of  $10^{-10}$  s, the slow block has time step of  $10^{-8}$  s. In the fast block, the continuity equations for gas species and electron energy (Eq. (4.4.1) and (4.4.3)), Poisson equation for gas species ( $\partial_x^2 \varphi = -\frac{nq_l}{\epsilon_0}$ ), conservation equations for tangential and normal velocities (Eq. (4.4.4) and (4.4.5)) are solved. In slow block, the general dynamic equation for nanoparticles (Eq. (4.4.6)) and Poisson equation for charged nanoparticles ( $\partial_x^2 \varphi = -\sum_{p=1}^{N_p} \sum_{c=-K_-}^{K_+} \frac{N_{pc} c_c}{\epsilon_0}$ ) are addressed. After the fast block runs for several RF cycles, the slow block started to run. Both blocks run for the same physical time, then this process repeats until the model reaches the desired physical time.

Let us detail the exchange of information between fast and slow blocks. The model starts to run several RF cycles in fast block at first. At this time, the terms  $R_{loss}$ ,  $E_{loss}$ ,  $P_{loss}$  are taken equal to 0, which means that the nanoparticles' effect on species densities, electron energy and electrical potential are not considered at the first fast block calculation. When the fast block runs to the last RF cycle, the averaged coefficients applied to the slow block have to be calculated. The averaged coefficients

---

<sup>40</sup> A. Haji-Sheikh et al, Series in Computational Methods and Physical Processes in Mechanics and Thermal Sciences, *CRC Press*,2021.

<sup>41</sup> E. Süli, An Introduction to Numerical Analysis, *Wiley*,2021.

<sup>42</sup> D. L. Scharfetter et al, *IEEE T. Electron Dev.* 16(1):64–77,1969.

depend on fast variables in fast block. In general, the outputs of fast block, such as  $Y_k$ ,  $T_e$ ,  $\varphi$ ,  $\tilde{w}$ ,  $\tilde{u}$ , have to be averaged and transferred to the slow block. Also, some coefficients related with nanoparticles have to be averaged, as discussed below. These averaged coefficients will be kept constant in slow block during the period of slow block. To fully understand the way of calculating averaged terms, Eq. (4.4.6) is rewritten as:

$$\partial_t N_{pc} + \nabla \cdot \left( \frac{1}{f_{pc}} \vec{F}_{pc}^{\text{ext}} - D_{pc} \partial_x N_{pc} \right) = S_{\text{easy}} + S_{\text{polynomial}} + S_{\text{slow}} \quad (4.5.1)$$

where,  $D_{pc}$  is the diffusion coefficient,  $\vec{F}_{pc}^{\text{ext}}$  is the external forces acting on nanoparticles, that is  $\vec{F}_{pc}^{\text{ext}} = \vec{F}_{pc}^{\text{grav}} + \vec{F}_{pc}^{\text{ion}} + \vec{F}_{pc}^{\text{drift}}$ , and  $S_{\text{easy}}$ ,  $S_{\text{polynomial}}$ , and  $S_{\text{slow}}$

denote all the other terms regrouped depending on their structure.  $\vec{F}_{pc}^{\text{grav}} = \vec{F}_{pc}^{\text{grav}}(W_{\text{slow}}, t)$  depends only on slow variables, and can be calculated in slow block.

$\vec{F}_{pc}^{\text{drift}} = \vec{F}_{pc}^{\text{drift}}(W_{\text{fast}}, t) = c_c \vec{E}$ . For the electric field we apply the splitting method to the Poisson equation since charged nanoparticles with large mass cannot react to the instantaneous electric field. This method will be detailed later. The ion drag force, is decomposed according to the Orbital Motion Limited, or ‘‘OML’’ theory, into a collection force and an orbital force  $\vec{F}_{pc}^{\text{ion}} = \vec{F}_{pc}^{\text{coll}} + \vec{F}_{pc}^{\text{orb}}$ . The collection force is

described as:  $\vec{F}_{pc}^{\text{coll}} = \sum_{l \in J} \pi b_c^2 \bar{v}_l n_l m_l \mathbf{v}_l$ . Here  $\bar{v}_l$  is an average macroscopic velocity

of the  $l^{\text{th}}$  species and  $b_c$  is the collection parameter. For orbital force,  $\vec{F}_{pc}^{\text{orb}} =$

$\sum_{l \in J} 4\pi b_{\pi/2}^2 \Gamma_G \bar{v}_l n_l m_l \mathbf{v}_l$ . Here,  $b_{\pi/2}$  is the effective impact parameter,  $\Gamma_G$  is the integral of the Coulomb logarithm from  $b_c$  to  $\lambda_D$  (the linearized Debye length). So, both collection force and orbital force depend on fast variables. The averaged values can be

calculated in fast block over one RF cycle:  $\bar{\mathbf{F}} = \frac{1}{t_{rf}} \int_t^{t+t_{rf}} \mathbf{F}(W_{\text{fast}}, t') dt'$ . The diffusion

coefficient of particles in section (p, c)  $D_{pc}$ ,  $D_{pc} = D_{pc}(W_{\text{fast}}, t') = \frac{k_B T}{f_{pc}}$  depends on

fast variables, thus the averaged diffusion coefficients should be calculated as  $\overline{D_{pc}} =$

$\frac{1}{t_{rf}} \int_t^{t+t_{rf}} D_{pc}(W_{\text{fast}}, t') dt'$ . The averaged values of source terms  $S_{\text{easy}}$ ,  $S_{\text{polynomial}}$ , and

$S_{\text{slow}}$  are calculated based on their dependency structure.  $S_{\text{easy}}$  is assumed to be a function of only fast variables,  $S_{\text{easy}} = S_{\text{easy}}(w_{\text{fast}})$ . The averaged source term is calculated:  $\overline{S_{\text{easy}}} = \frac{1}{t_{\text{rf}}} \int_t^{t+t_{\text{rf}}} S_{\text{easy}}(W_{\text{fast}}, t') dt'$ . For example, the averaged nucleation rate  $\left[\frac{\partial N_{pc}}{\partial t}\right]_{\text{nuc}}$  is calculated in this form.  $S_{\text{slow}}$  represents the source terms that only depend on slow variables,  $S_{\text{slow}} = S_{\text{slow}}(W_{\text{slow}}, t)$ , which is calculated in slow block. In our model, only coagulation rate  $\left[\frac{\partial N_{pc}}{\partial t}\right]_{\text{coag}}$  does not need to be averaged.  $S_{\text{polynomial}}$  is assumed to be a polynomial function of the slow variables with coefficients that are only functions of fast variables, written in the form:

$$S_{\text{polynomial}} = \sum_{pc} \alpha_{pc}(w_{\text{fast}}, t) N_{pc} + \sum_{pc, qd} \alpha_{pc, qd}(w_{\text{fast}}, t) N_{pc} N_{qd} \quad (4.5.2)$$

Where  $\alpha_{pc}(w_{\text{fast}}, t)$  and  $\alpha_{pc, qd}(w_{\text{fast}}, t)$  are the terms which only depend on fast variables,  $N_{pc}$  and  $N_{qd}$  are the slow variables. The remaining source terms,  $\left[\frac{\partial N_{pc}}{\partial t}\right]_{\text{charge}}$  and  $\left[\frac{\partial N_{pc}}{\partial t}\right]_{\text{growth}}$ , belong to this case. The surface growth can be written as:

$$\left[\frac{\partial N_{pc}}{\partial t}\right]_{\text{growth}} = \frac{\bar{v}_{p-1}}{\bar{v}_p - \bar{v}_{p-1}} \bar{H}_{p-1c} N_{p-1c} - \frac{\bar{v}_p}{\bar{v}_{p+1} - \bar{v}_p} \bar{H}_{pc} N_{pc}, \quad (4.5.3)$$

Where  $\bar{H}_{pc}(t) = \left(\sum_{l \in \mathcal{S}} \hat{\omega}_{pc}^l V_m^{\text{Si}} v_{\text{Si}}^l\right) \frac{\bar{s}_p}{\bar{v}_p}$ ,  $\hat{\omega}_{pc}^l$  is the average molar surface flux of molecules of the  $l$ th species onto particles in section  $(p, c)$ . In  $\left[\frac{\partial N_{pc}}{\partial t}\right]_{\text{growth}}$ , only  $\hat{\omega}_{pc}^l$  has dependency on fast variables,  $\hat{\omega}_{pc}^l = \hat{\omega}_{pc}^l(w_{\text{fast}}, t)$ . So the average value of  $\hat{\omega}_{pc}^l$  is calculated in the fast block,  $\overline{\hat{\omega}_{pc}^l} = \frac{1}{t_{\text{rf}}} \int_t^{t+t_{\text{rf}}} \hat{\omega}_{pc}^l(W_{\text{fast}}, t') dt'$ . The charge fluctuation

$\left[\frac{\partial N_{pc}}{\partial t}\right]_{\text{charge}}$  is rewritten as:

$$\begin{aligned} \left[\frac{\partial N_{pc}}{\partial t}\right]_{\text{charge}} &= v_{p, c+1}^e N_{p, c+1} + \sum_{l \in \mathcal{S}^-} v_{p, c+1}^l N_{p, c+1} + \sum_{l \in \mathcal{S}^+} v_{p, c-1}^l N_{p, c-1} \\ &\quad - v_{pc}^e N_{pc} - \sum_{l \in \mathcal{S}^-} v_{pc}^l N_{pc} - \sum_{l \in \mathcal{S}^+} v_{pc}^l N_{pc} \end{aligned} \quad (4.5.4)$$

Where  $v_{pc}^l = 4\pi \bar{r}_p^2 \mathcal{N}_A \hat{\omega}_{pc}^l$ . In this term, we can see that only  $\hat{\omega}_{pc}^l$  has to be averaged in the fast block. In conclusion, as one fast block approaches to the end, the coefficients of  $Y_k, T_e, \varphi, \tilde{w}, \tilde{u}, \mathbf{E}, F_{pc}^{\text{coll}}, F_{pc}^{\text{orb}}, D_{pc}, \left[\frac{\partial N_{pc}}{\partial t}\right]_{\text{nuc}}, \hat{\omega}_{pc}^l$  have to be averaged over the last

RF cycle and transferred to the slow block.

In the slow block,  $E_{loss}$ ,  $R_{loss}$  and  $P_{loss}$  will be calculated at each iteration and transferred to the fast block at the end of the slow block. During the running of the fast block, these three terms are kept constant.

#### 4.5.2 the splitting method for Poisson equation

The Poisson equation is dealt with both in fast and slow blocks. In the fast block, Poisson equation is written as

$$\partial_x^2 \varphi_{fast}(x, t) = -\frac{nqI}{\epsilon_0} \quad (4.5.5)$$

The boundary conditions are in the form:

$$\text{Grounded electrode: } \varphi_{fast}(0, t) = 0$$

$$\text{Driven electrode } \varphi_{fast}(d, t) = \varphi_{app} \quad (4.5.6)$$

where  $\varphi_{app}$  denotes the applied voltage.

As the first fast-slow block is running, the effective potential:  $\varphi_{fast\_eff}(x, t) = \varphi_{fast}(x, t)$ . After the first running: the effective potential:  $\varphi_{fast\_eff}(x, t) = \varphi_{fast}(x, t) + \varphi_{slow}(x, t)$ .  $\varphi_{slow}(x, t)$  is solved in the slow block.

In slow block: The Poisson equation is written as:

$$\partial_x^2 \varphi_{slow}(x, t) = -\sum_{p=1}^{N_p} \sum_{c=-K_-}^{K_+} \frac{N_{pc} c_c}{\epsilon_0} \quad (4.5.7)$$

The corresponding boundary conditions are in the form:

$$\text{Grounded electrode: } \varphi_{slow}(0, t) = 0$$

$$\text{Driven electrode: } \varphi_{slow}(d, t) = 0 \quad (4.5.8)$$

The effective potential is in the form:

$$\varphi_{slow\_eff}(x, t) = \overline{\varphi_{fast}(x, t)} + \varphi_{slow}(x, t) \quad (4.5.9)$$

Therefore, we know the electrical potential in the slow and fast block, the effective electric fields in both blocks are the derivative of effective electrical potentials respectively.

## 4.6 Results and discussion

### 4.6.1 Validation

The time-splitting SiH<sub>4</sub>-H<sub>2</sub> dusty plasma model must be validated before application. The fast block has to be validated before the time-splitting model is complete. Therefore, the validation contains two sections: (1) the validation of fast block of the time-splitting model against pristine plasma model; (2) once the fast block is validated, the validation of the time-splitting model is required. Then the time-splitting SiH<sub>4</sub>-H<sub>2</sub> dusty plasma model can be used for our studies.

(1) Validation of fast block of the time-splitting model against pristine plasma model

The process conditions for both models are the following:  $p = 2.5$  Torr,  $T = 448$  K,  $f = 13.56$  MHz; gas composition includes 1.4% SiH<sub>4</sub> and 98.6% H<sub>2</sub>, the applied

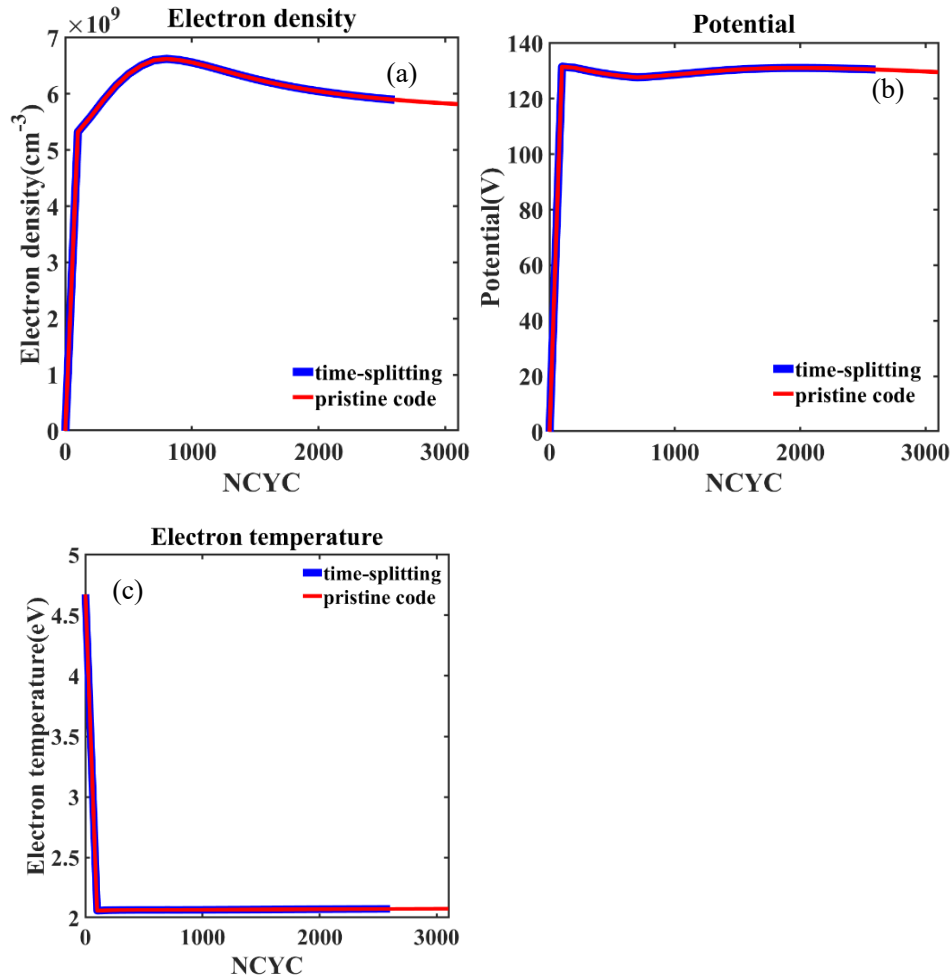


**Figure 4.4.** Time-averaged values as function of number of RF cycles (NCYC) at the center of the discharge. 1 RF cycle is equivalent to 74 ns. The red curve is calculated using pristine plasma model, the blue one is calculated from time-splitting model. (a) time-averaged electron density. (b) time-averaged electric potential. (c) time averaged electron temperature.

voltage is 300 V. The gas chemistry and surface chemistry are the same as in Chapter 2. It is necessary for both models to employ the exact same process conditions in order to validate the time-splitting model.

The Figure 4.4 shows the time-averaged electron density, electric potential and electron temperature at the center of the discharge as a function of the number of RF cycles. We can see that both models produce the exact same results. To further validate the fast block, the spatiotemporal evolutions of the plasma properties in the discharge have to be checked. Figure 4.5 presents the spatiotemporal evolution of electric potential, electron temperature and electron density over one RF cycle at steady state. We can clearly see that the time-splitting model and pristine plasma model produce the exact same results. Therefore, the fast block of time-splitting model is validated against pristine model. For the Figure 4.5(a) and (b), we can see that the electric potential at the grounded electrode remains equal to zero along one RF cycle, while it matches a sine function at the powered electrode. In Figure 4.5(c) and (d), the value of electron temperature in the plasma bulk is about 5 eV, while the value of electron temperature becomes larger when the plasma sheaths expand. In Figure 4.5(e) and (f), we can see that electron density is much higher in the plasma bulk than that in the sheaths, which is because electrons are confined in the plasma. In particular, electron density near the sheath edge becomes larger when the plasma sheaths contract.

## (2) validation of the time-splitting model with coupled model

After the fast block of time-splitting model is validated, the time-splitting model has to be validated against the fully coupled model before application. The coupled model represents the fluid-sectional model without using time-splitting method. The process conditions for validation (2) are the same as the condition of validation (1). Figure 4.6 shows the comparison of results between time-splitting model and fully coupled model. In order to reduce computing time, a simple gas chemistry (9 electron collisions and 12 heavy species reactions) is applied and the results are computed after 0.15 ms. As we can see from Figure 4.6 (a), for the negative nanoparticle and positive nanoparticle profile, the coupled model and time-splitting model give very similar

results. Also, both models show the same results of net charged particle density profile, as shown in Figure 4.6 (b). Based on this, we can consider that the time-splitting model is validated.

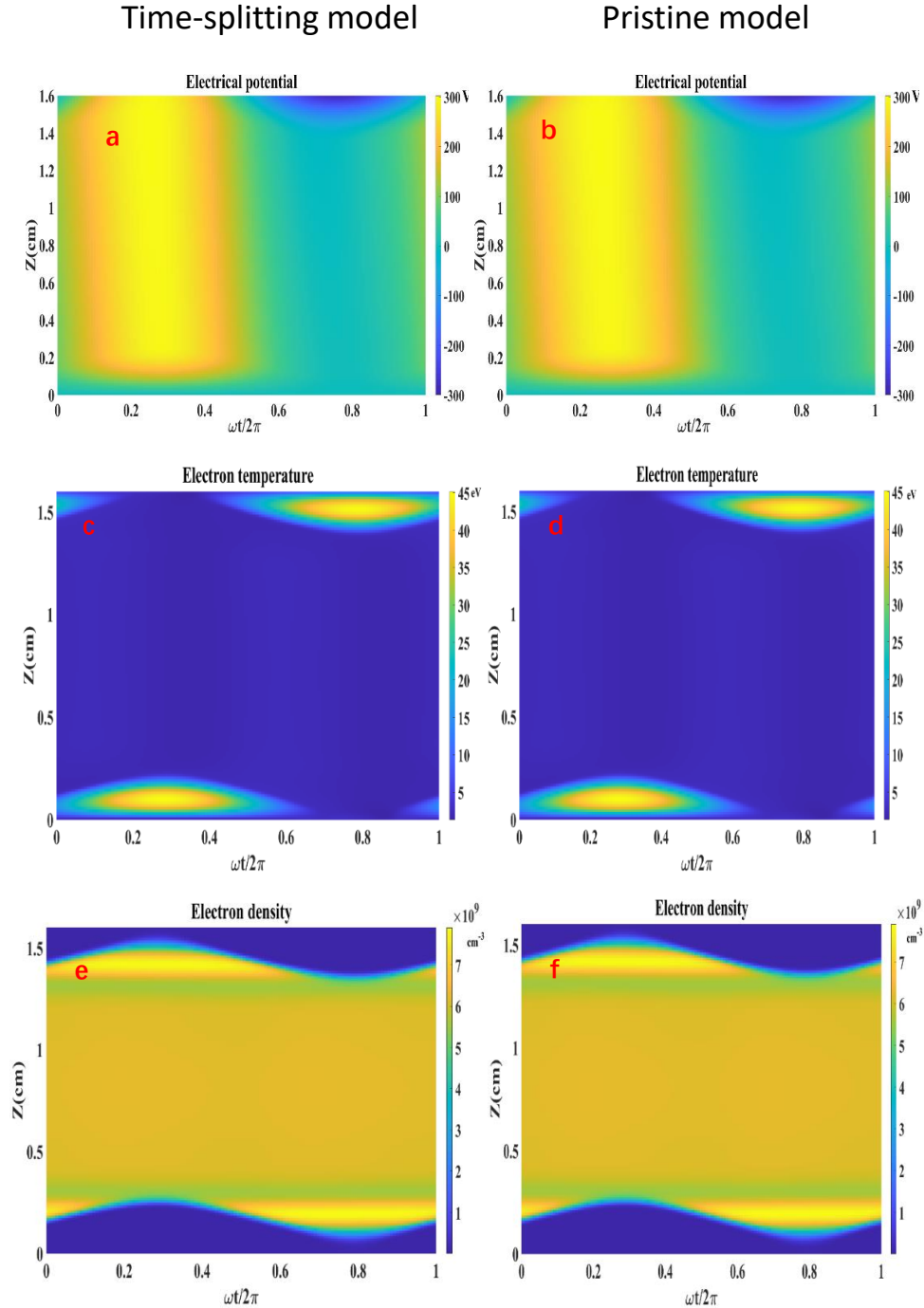


**Figure 4.5.** Time-space evolutions of plasma properties. (a), (c) and (e) are the electrical potential, electrical temperature and electron density profiles in the discharge along one RF cycle, released from time-splitting model. (b), (d) and (f) are the corresponding plasma properties released from pristine plasma model.

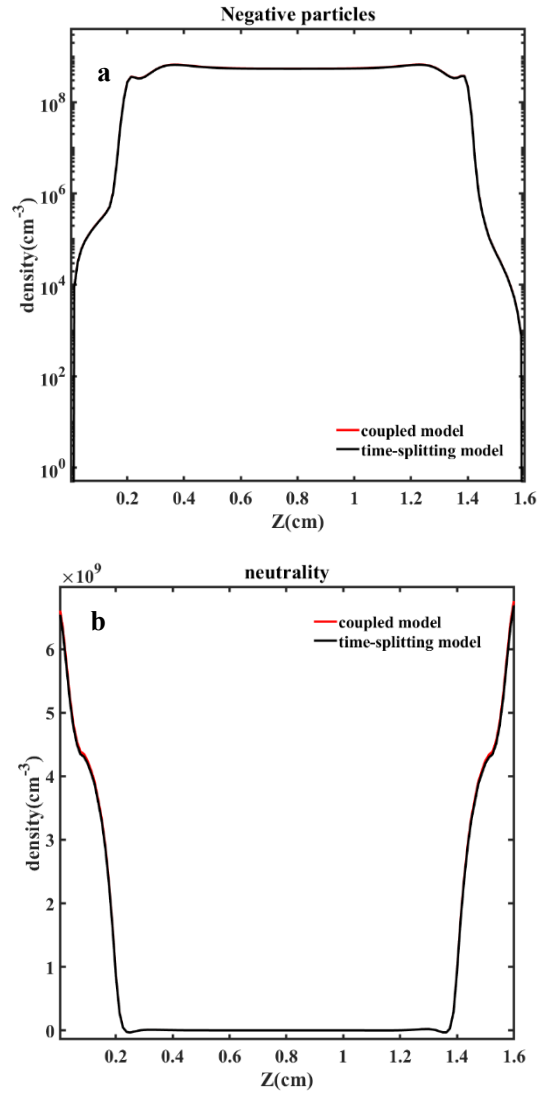


**Figure 4.6.** Validation of the time-splitting model with coupled model. (a) the density of negative particles along the discharge. (b) net charge density along the discharge.

#### 4.6.2 Nanoparticles

The process conditions considered here, which are typical process conditions for deposition of polymorphous silicon<sup>43,44</sup>, are as follows: the gas pressure is set at  $p = 2 \text{ Torr}$ , the applied power  $P = 10 \text{ W}$ , the gas temperature  $T = 448 \text{ K}$ , the inlet gas mass fraction includes 1.4%  $\text{SiH}_4$  and 98.6%  $\text{H}_2$ . The frequency is 13.56 MHz. For the nanoparticles, the initial section of nanoparticles has radius of 0.36 nm. The volume between subsequent two sections have a relation:  $v_p = f v_{p-1}$ , where  $f$  is the volume factor in order to proceed to the next section, and  $f = 2.85$  in the thesis. Because we

<sup>43</sup> P. Roca i Cabarrocas et al., *J. Phys. D: Appl. Phys.*, 40(8):2258–66,2007.

<sup>44</sup> Ka-Hyun Kim et al.,*Sci. Rep.*, 7(1): 40553,2017.

are only interested in the early stage of nanoparticle growth, the absolute charge of nanoparticle does not exceed one elementary charge. Figure 4.7 shows the density of nanoparticles along the discharge. Figure 4.7 (a) shows the density of nanoparticles

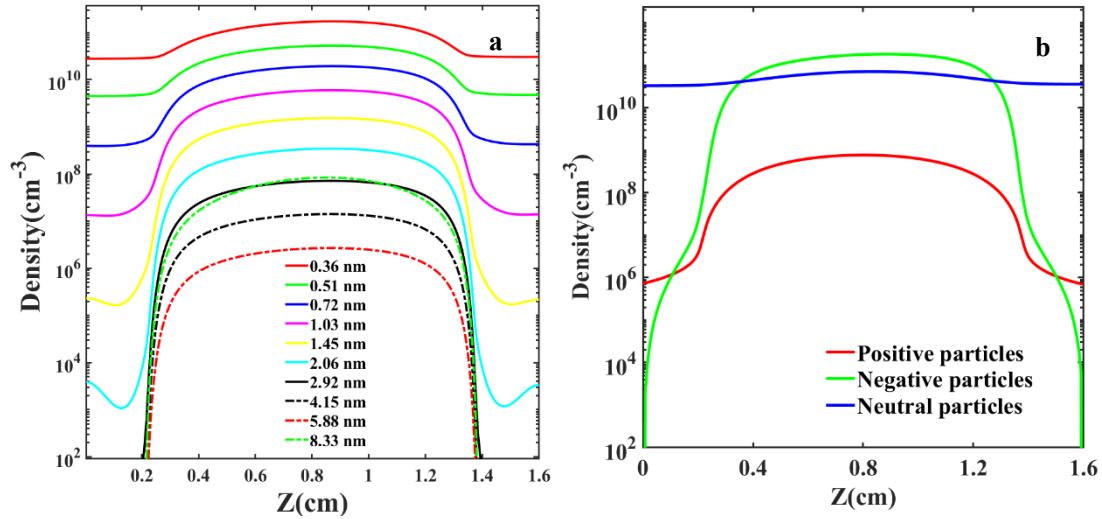


**Figure 4.7** The density of nanoparticles along the reactor. The process conditions are following:  $p = 2$  Torr, the applied power  $P = 10$  W, the gas temperature  $T = 448$  K, the inlet gas mass fraction includes 1.4% SiH $_4$  and 98.6% H $_2$ . The frequency is 13.56 MHz. The time is 4 ms. (a) The density of nanoparticles along the reactor for different nanoparticles' size (radius). Time = 4 ms. (b) The density of positive, negative and neutral particles along the reactor.

of different sizes along the discharge. As we can see, the density of nanoparticles in the middle of the discharge decreases as the size increases. In particular, the nanoparticles with larger size (above 2.92 nm) are fully constrained in the middle of the discharge since they are mainly negatively charged. Also, we can see that the density of nanoparticles with 2.06 nm increases near the electrodes due to inertia effect, while larger particles (above 2 nm) are mainly negatively charged and confined in the plasma bulk. Figure 4.7(b) shows the density of positive, negative and neutral nanoparticles along the discharge. As we can see, the density of negative particles is largest in the middle of discharge since negative particles are not energetic enough to overcome the potential barrier in the sheaths, while positive particles can reach electrodes or walls since they are accelerated by the potential in the plasma sheaths. For neutral particles, they only diffuse in the discharge.

### 4.6.3 The effect of gas pressure on the nanoparticles

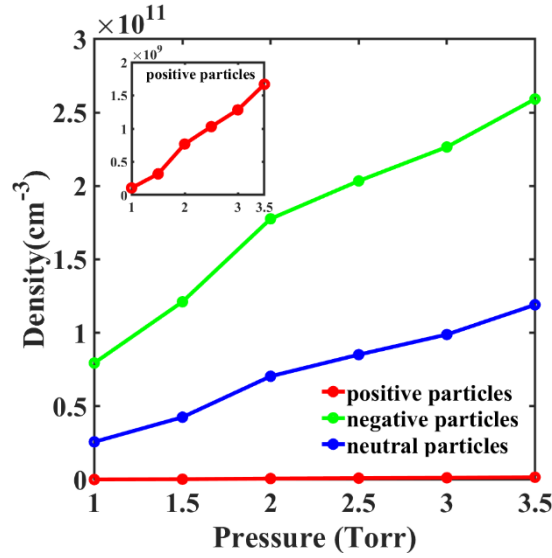


**Figure 4.8.** The density of nanoparticles in the middle of discharge as a function of gas pressure. Time = 4 ms. The green line indicates the density of negative particles, the blue line points to the density of neutral particles, and the red line points to the density of positive particles. In particular, the inset figure shows the density of positive particles as a function of gas pressure.

Figure 4.8 shows that the density of nanoparticles in the mid of the discharge as a function of gas pressure. In these figures, each point is calculated by sum over the nanoparticles' density of all sizes. In general, we can see that the density of nanoparticles increases as the gas pressure increases. This is because the collision frequency increases as gas pressure increases, which induces the increase of nanoparticles' growth. For charged nanoparticles, the density of negative particles is much larger than the density of positive particles at same gas pressure. This is because nanoparticles are mainly formed by electron or negative ions attachment and negative nanoparticles are pulled to the center of the plasma by the electric field, while positively charged particles are mainly from charging fluctuation and are drifted towards the electrodes<sup>25</sup>. In detail, we can see that negatively charged particles increase from  $7.5 \times 10^{10} \text{cm}^{-3}$  at 1 Torr to  $2.6 \times 10^{11} \text{cm}^{-3}$  at 3.5 Torr. The density of positively charged particles increases from  $1 \times 10^8 \text{cm}^{-3}$  at 1 Torr to  $1.6 \times 10^9 \text{cm}^{-3}$  at 3.5 Torr, as shown in the inset figure. For neutral particles, the density increases from  $2.5 \times 10^{10} \text{cm}^{-3}$  at 1 Torr to  $1.2 \times 10^{11} \text{cm}^{-3}$  at 3.5 Torr.

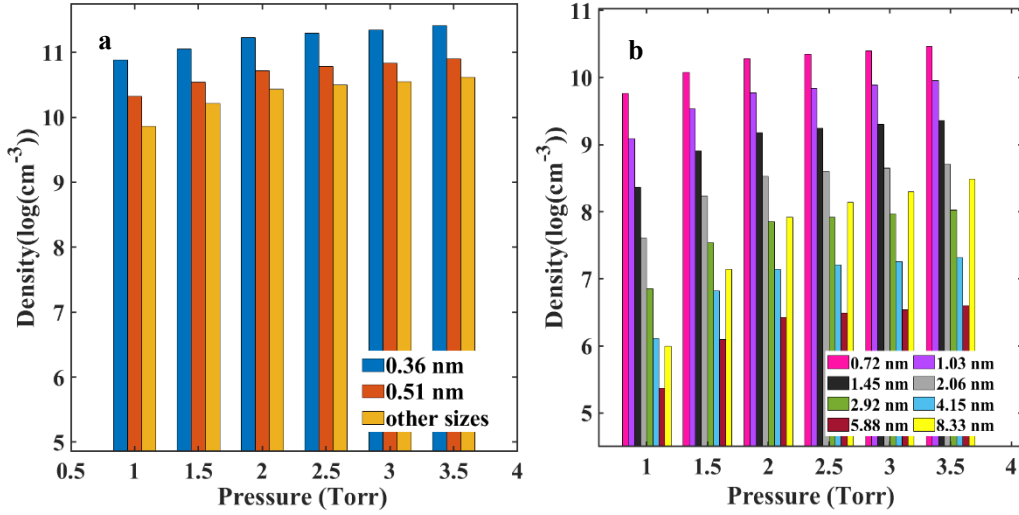


**Figure 4.9.** The density of nanoparticles in the middle of discharge as a function of gas pressure in logarithmic scale. Time = 4 ms. (a) nanoparticles densities with size of 0.36 nm, 0.51 nm and others. (b) nanoparticles densities with sizes larger than 0.51 nm.

Figure 4.9 shows different size of nanoparticles' density as a function of gas pressure. The densities shown in these figures are in logarithmic scale. From Figure 4.9 (a), we can see that the nanoparticles density with size of 0.36 nm are larger than that of 0.51 nm at fixed gas pressure. Also, the density of nanoparticles increases as gas pressure increases, while the density of nanoparticles with sizes larger than 0.51 nm is smaller than particle's density with 0.36 nm and 0.51 nm. Figure 4.9 (b) shows the density distribution of nanoparticles with sizes larger than 0.51 nm as a function of gas pressure. For each pressure, the larger the nanoparticle's size is, the smaller is the density. For example, at 3.5 Torr, we can see that the density of larger nanoparticles is smaller than the smaller ones. In fact, we can see that the particle density with size of 8.33 nm is larger than the smaller sizes at fixed gas pressure. This is a numerical issue because we only consider 10 sections in our model (8.33 nm is largest size) and nanoparticles with larger size than 8.33 nm stay in the largest section.

#### 4.6.4 The contribution of nanoparticles to the deposition of silicon thin films

The deposition rate of nanoparticles is calculated as follow:

$$v_{\text{Si(s)}} = \sum_{n,p} \frac{\sigma_{np} N_{\text{Si}}^{np} \Gamma_{pc,0} M_{\text{Si}}}{N_A n_{\text{Si}}} * 10^8 \text{ (\AA/s)}, \quad (4.67)$$

where  $v_{\text{Si(s)}}$  denotes the deposition rate with units  $\text{\AA/s}$ ,  $\sigma_{np}$  are the sticking coefficients

of nanoparticles. Since the data of sticking coefficients of nanoparticles have not been reported, we assume  $\sigma_{np} = 1$  for all nanoparticles.  $\Gamma_{pc,0} = N_{pc} \vec{V}_{pc} \cdot \vec{n}$  is the nanoparticles' flux towards the substrate in section  $(n, p)$  with units  $(cm^{-2} * s^{-1})$ ,  $M_{Si} = 28 g/mol$  is the molar mass of silicon,  $N_A$  is the Avogadro constant, and  $n_{Si} = 2.33 g/cm^3$  is the mass density of a-Si:H. For each section of nanoparticles, the number of silicon atoms is listed in Table I. In this table, each section represents the average radius of nanoparticles and the silicon atoms contained. Here, we consider 10 sections, which have radius ranging from 0.36 nm to 8.31 nm and contain silicon atoms from 10 to 123914.

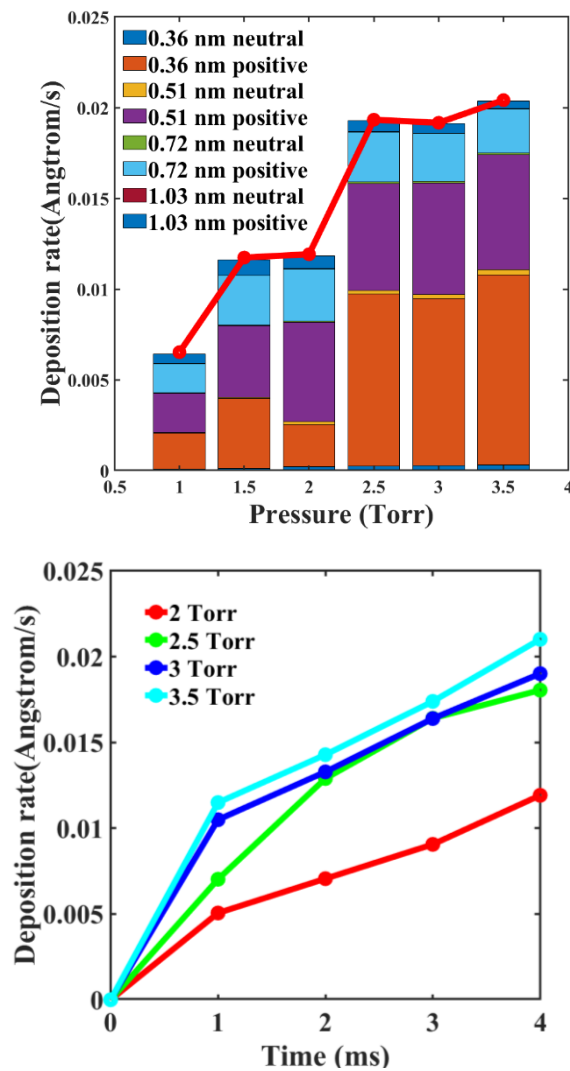
Figure 4.10 (a) shows the contribution of nanoparticles to the deposition rate of silicon thin films. For nanoparticles, we can see that positive particles mainly contribute to the deposition rate, while neutral particles have much less contribution, as shown in

Table I: Average radius and number of Si atoms contained in each section

Section	Average radius (nm)	Number of Si atoms
1	0.36	10
2	0.51	28
3	0.72	81
4	1.02	231
5	1.45	659
6	2.06	1878
7	2.92	5353
8	4.13	15256
9	5.86	43478
10	8.31	123914

Figure 4.10 (a). Also, we can see that the deposition rate of particles increases as the gas pressure increases. In general, the deposition rate of nanoparticles increases from  $7 \times 10^{-3} \text{ \AA/s}$  at 1 Torr to  $2 \times 10^{-2} \text{ \AA/s}$  at 3.5 Torr. The deposition rates resulting from nanoparticles are quite small in the early stage of nanoparticles formation at time = 4 ms. Compared to gaseous species, the deposition rate of nanoparticles is negligible.

This contrasts with the estimations of references<sup>41, 45</sup>, where the nanoparticles' contribution on deposition rate could go up to 100%. The reason of low deposition rate of nanoparticles is attributed to the fact that we are focusing on the initial stage of nanoparticle formation (time = 4 ms). Figure 4.10 (b) shows that the deposition rates of nanoparticles vary with time for gas pressure 2 Torr – 3.5 Torr. As we can see, the deposition rates due to nanoparticles increases as time increases for all pressures. The contribution of nanoparticles on deposition is expected to be larger at longer time.



**Figure 4.10** (a) The contribution of nanoparticles with different sections and sizes on deposition rate as a function of gas pressure. Time = 4 ms. (b) The deposition rates of nanoparticles vary with time for different gas pressures.

<sup>45</sup> Nihed Chaâbane et al., *Appl. Phys. Lett.*, 88(20) : 203111, 2006.

## 4.7 Conclusions

We have applied a fluid-sectional model for nanoparticle formation in  $\text{SiH}_4\text{-H}_2$  plasma by using time-splitting method. The model contains a complete chemistry mechanism of nanoparticles' nucleation, effect of charge enhancement on coagulation, and transport of nanoparticles. Also, the effect of the nanoparticles on plasma species densities, electric potential and electron temperature is taken into account. The model has been used to study the early stages of nanoparticle formation under typical conditions for silicon thin film deposition, where the particle radius remains below 10 nm.

The time-splitting method is applied to make the model efficient. The reason why we take this method is that a fully coupled  $\text{SiH}_4\text{-H}_2$  plasma model used for nanoparticles formation is time-consuming, for example, a result at 1ms takes 6 months! This method has also been applied by P. Agarwal<sup>46</sup> and K. D. Bleecker<sup>14</sup>. Separated time integrations are carried out for “fast” variables, namely the electric potential, the electron temperature and the charged species densities, and “slow” variables, which is the nanoparticles. The results are validated by comparison with the model with a fully coupled method. Also, the computing time is reduced a lot compared to the fully coupled code. For example, the computing time is about 3 months for a 4 ms result.

At constant pressure, the nanoparticles' density decreases as nanoparticle's size increases. For a given size, the negative particles density is much larger than positive and neutral particles. Also, at a given size, the density of nanoparticles increases as gas pressure increases. We can see that the larger size of nanoparticles ( $> 5$  nm) are formed at higher pressure (3 or 3.5 Torr) at time = 4 ms. This is reasonable since larger pressure will cause more collisions between particles or particles with gas species, which promotes particles growth. Finally, we conclude that the contribution of nanoparticles on deposition rate of silicon thin films is negligible at the early stage of nanoparticles formation.

---

<sup>46</sup> P. Agarwal, Numerical Modeling of Plasmas in Which Nanoparticles Nucleate and Grow, Ph.D. thesis, 2012.

## 4.8 References

- <sup>1</sup> A. Bouchoule, *Dusty plasmas: physics, chemistry, and technological impacts in plasma processing*, Wiley Press, 1999.
- <sup>2</sup> P. Roca i Cabarrocas, Patrick Gay, and Aomar Hadjadj, Experimental Evidence for Nanoparticle Deposition in Continuous Argon–Silane Plasmas: Effects of Silicon Nanoparticles on Film Properties, *J. Vac. Sci. Technol. A*, 14(2):655,1998, <https://doi.org/10.1116/1.580162>.
- <sup>3</sup> P. Roca i Cabarrocas, S. Hamma, S.N. Sharma, G. Viera, E. Bertran, J. Costa, Nanoparticle Formation in Low-Pressure Silane Plasmas: Bridging the Gap between a-Si:H and Mc-Si Films, *J. Non. Cryst. Solids*, 227:(871-875),1998, [https://doi.org/10.1016/S0022-3093\(98\)00200-2](https://doi.org/10.1016/S0022-3093(98)00200-2).
- <sup>4</sup> P. Roca i Cabarrocas, Plasma Enhanced Chemical Vapor Deposition of Amorphous, Polymorphous and Microcrystalline Silicon Films, *J. Non. Cryst. Solids*, 266–269: (31–37), 2000, [https://doi.org/10.1016/S0022-3093\(99\)00714-0](https://doi.org/10.1016/S0022-3093(99)00714-0).
- <sup>5</sup> P. Roca i Cabarrocas, A. F. i Morral, S. Lebib, and Y. Poissant, Plasma production of nanocrystalline silicon particles and polymorphous silicon thin films for large-area electronic devices, *Pure Appl. Chem.*, 74(3):359–67,2002, <https://doi.org/10.1351/pac200274030359>.
- <sup>6</sup> C. Longeaud, J.P. Kleider, P. Roca i Cabarrocas, S. Hamma, R. Meaudre, M. Meaudre, Properties of a New A-Si:H-like Material: Hydrogenated Polymorphous Silicon, *J. Non. Cryst. Solids*, 227–230(1):96–99, 1998, [https://doi.org/10.1016/S0022-3093\(98\)00217-8](https://doi.org/10.1016/S0022-3093(98)00217-8).
- <sup>7</sup> A. Bouchoule, A. Plain, L. Boufendi, J. Ph. Blondeau, C. Laure, Particle Generation and Behavior in a Silane-argon Low-pressure Discharge under Continuous or Pulsed Radio-frequency Excitation, *J. Appl. Phys.*, 70(4):1991–2000,1991, <https://doi.org/10.1063/1.349484>.
- <sup>8</sup> L. Boufendi, A. Plain, J. Ph. Blondeau, A. Bouchoule, C. Laure, and M. Toogood, Measurements of Particle Size Kinetics from Nanometer to micrometer scale in a low-pressure argon-silane radio-frequency discharge, *Appl. phys. lett.*, 60(2):169-171, 2021, <https://aip.scitation.org/doi/pdf/10.1063/1.106981>.
- <sup>9</sup> A. Bouchoule and L. Boufendi, Particulate Formation and Dusty Plasma Behaviour in Argon-Silane RF Discharge, *Plasma Sources Sci. Technol.*, 2(3):204,1993,

<https://doi.org/10.1088/0963-0252/2/3/011>.

<sup>10</sup> L. Boufendi and A. Bouchoule, Particle Nucleation and Growth in a Low-Pressure Argon-Silane Discharge, *Plasma Sources Sci. Technol.*, 3(3):262–67, 1994, <https://doi.org/10.1088/0963-0252/3/3/004>.

<sup>11</sup> L. Boufendi, J. Hermann, A. Bouchoule, and B. Dubreuil, Study of Initial Dust Formation in an Ar-SiH<sub>4</sub> Discharge by Laser Induced Particle Explosive Evaporation, *J. Appl. Phys.*, 76(1):148–53,1994, <https://doi.org/10.1063/1.357120>.

<sup>12</sup> A Bouchoule and L Boufendi, High Concentration Effects in Dusty Plasmas, *Plasma Sources Sci. Technol.*,3(3):292–301,1994, <https://doi.org/10.1088/0963-0252/3/3/009>.

<sup>3</sup> U. V. Bhandarkar, M. T. Swihart, S. L. Girshick and U. R. Kortshagen, Modelling of Silicon Hydride Clustering in a Low-Pressure Silane Plasma, *J. Phys. D: Appl. Phys.*, 33(21): 2731–46,2000, <https://doi.org/10.1088/0022-3727/33/21/311>.

<sup>4</sup> U. Bhandarkar, U. Kortshagen, and S. L. Girshick, Numerical Study of the Effect of Gas Temperature on the Time for Onset of Particle Nucleation in Argon–Silane Low-Pressure Plasmas, *J. Phys. D: Appl. Phys.*, 36(12):1399–1408,2003, <https://doi.org/10.1088/0022-3727/36/12/307>.

<sup>5</sup> K. De Bleecker, A. Bogaerts, R. Gijbels, W. Goedheer, Modeling of Dusty Silane Discharges: Nanoparticle Formation, Transport and Charging, In APS Annual Gaseous Electronics Meeting Abstracts (pp. JM1-004).

<sup>6</sup> K. De Bleecker, A. Bogaerts, and W. Goedheer, Modelling of Nanoparticle Coagulation and Transport Dynamics in Dusty Silane Discharges, *New J. Phys.*, 8(9) : 178–178, 2006, <https://doi.org/10.1088/1367-2630/8/9/178>.

<sup>7</sup> K. De Bleecker, D. Herrebout, A. Bogaerts, R. Gijbels, P. Descamps, One-Dimensional Modelling of a Capacitively Coupled Rf Plasma in Silane/Helium, Including Small Concentrations of O<sub>2</sub> and N<sub>2</sub>, *J. Phys. D: Appl. Phys.*, 36(15) :1826–33,2003, <https://doi.org/10.1088/0022-3727/36/15/313>.

<sup>8</sup> K. De Bleecker, A. Bogaerts, and W. Goedheer, Modeling of the Formation and Transport of Nanoparticles in Silane Plasmas, *Phys. Rev. E*, 70(5):056407,2004, <https://doi.org/10.1103/PhysRevE.70.056407>.

<sup>9</sup> K. De Bleecker, A. Bogaerts, and W. Goedheer, Role of the Thermophoretic Force on the Transport of Nanoparticles in Dusty Silane Plasmas, *Phys. Rev. E*, 71(6): 066405, 2005, <https://doi.org/10.1103/PhysRevE.71.066405>.

- <sup>20</sup> P. Roca i Cabarrocas, Th. Nguyen-Tran, Y.Djeridane, A. Abramov, E.Johnson, and G. Patriarche, Synthesis of Silicon Nanocrystals in Silane Plasmas for Nanoelectronics and Large Area Electronic Devices, *J. Phys. D: Appl. Phys.*, 40(8): 2258–66,2007, <https://doi.org/10.1088/0022-3727/40/8/S04>.
- <sup>21</sup> S. J. Warthesen and S. L. Girshick, Numerical Simulation of the Spatiotemporal Evolution of a Nanoparticle–Plasma System, *Plasma Chem. Plasma Process.*, 27(3): 292–310,2007, <https://doi.org/10.1007/s11090-007-9054-6>.
- <sup>22</sup> P. Agarwal and S. L. Girshick, Sectional Modeling of Nanoparticle Size and Charge Distributions in Dusty Plasmas, *Plasma Sources Sci. Technol.*, 21(5): 055023,2012, <https://doi.org/10.1088/0963-0252/21/5/055023>.
- <sup>23</sup> J. M. Orlac'h, Modeling of a Silane-Hydrogen Plasma Discharge Including Nanoparticle Dynamics for Photovoltaic Applications. These de doctorat, Université Paris-Saclay, 2017, <https://www.theses.fr/2017SACLX023>.
- <sup>24</sup> S. Chapman, T. G. Cowling, The mathematical theory of non-uniform gases: an account of the kinetic theory of viscosity, thermal conduction and diffusion in gases. *Cambridge university press*,1991.
- <sup>25</sup> S. K. Friedlander, Smoke, Dust, and Haze: Fundamentals of Aerosol Dynamics *Oxford University Press*, 2000.
- <sup>26</sup> U. Kortshagen and U. Bhandarkar, Modeling of Particulate Coagulation in Low Pressure Plasmas, *Phys. Rev. E*, 60(1):887–98,1999, <https://doi.org/10.1103/PhysRevE.60.887>.
- <sup>27</sup> P. Agarwal and S. L. Girshick, Sectional Modeling of Nanoparticle Size and Charge Distributions in Dusty Plasmas, *Plasma Sources Sci. Technol.*, 21(5): 055023,2012, <https://doi.org/10.1088/0963-0252/21/5/055023>.
- <sup>28</sup> D. D. Huang, J. H. Seinfeld, and K. Okuyama, Image Potential between a Charged Particle and an Uncharged Particle in Aerosol Coagulation—Enhancement in All Size Regimes and Interplay with van Der Waals Forces, *J. Colloid Interface Sci.*,141(1): 191–98,1991, [https://doi.org/10.1016/0021-9797\(91\)90314-X](https://doi.org/10.1016/0021-9797(91)90314-X).
- <sup>29</sup> L. Ravi and S. L. Girshick, Coagulation of Nanoparticles in a Plasma, *Phys. Rev. E*, 79(2): 026408,2009, <https://doi.org/10.1103/PhysRevE.79.026408>.
- <sup>30</sup> F. Gelbard, Y. Tambour, and J. H. Seinfeld, Sectional Representations for Simulating Aerosol Dynamics, *J. Colloid Interface Sci.*, 76(2):541–56,1980,

[https://doi.org/10.1016/0021-9797\(80\)90394-X](https://doi.org/10.1016/0021-9797(80)90394-X).

<sup>31</sup> Y. P. Kim and J. H. Seinfeld, Simulation of Multicomponent Aerosol Condensation by the Moving Sectional Method, *J. Colloid Interface Sci.*, 135(1): 185–99, 1990, [https://doi.org/10.1016/0021-9797\(90\)90299-4](https://doi.org/10.1016/0021-9797(90)90299-4).

<sup>32</sup> D. R. Warren and J. H. Seinfeld, Simulation of Aerosol Size Distribution Evolution in Systems with Simultaneous Nucleation, Condensation, and Coagulation, *Aerosol Sci. Technol.*, 4(1): 31–43, 1985, <https://doi.org/10.1080/02786828508959037>.

<sup>33</sup> V. A. Schweigert and I. V. Schweigert, Coagulation in a Low-Temperature Plasma, *J. Phys. D: Appl. Phys.*, 29(3):655–59,1996, <https://doi.org/10.1088/0022-3727/29/3/026>.

<sup>34</sup> T. Matsoukas, M. Russell, and M. Smith, Stochastic Charge Fluctuations in Dusty Plasmas, *J. Vac. Sci. Technol. A*, 14(2): 624–30,1996, <https://doi.org/10.1116/1.580156>.

<sup>35</sup> M. S. Barnes, J. H. Keller, J. C. Forster, J. A. O'Neill, and D. K. Coultas, Transport of Dust Particles in Glow-Discharge Plasmas, *Phys. Rev. Lett.*, 68(3): 313–16,1992, <https://doi.org/10.1103/PhysRevLett.68.313>.

<sup>36</sup> S. Chandrasekhar, Stochastic Problems in Physics and Astronomy, *Rev. Mod. Phys.*, 15(1): 1–89,1943, <https://doi.org/10.1103/RevModPhys.15.1>.

<sup>37</sup> M. R. Akdim and W. J. Goedheer, Modeling of Dust in a Silane/Hydrogen Plasma, *J. Appl. Phys.*,94(1): 104–9,2003, <https://doi.org/10.1063/1.1578522>.

<sup>38</sup> P. S. Epstein, On the Resistance Experienced by Spheres in Their Motion through Gases, *Phys. Rev.*,23(6): 710–33,1924, <https://doi.org/10.1103/PhysRev.23.710>.

<sup>39</sup> S. J. Warthesen, Numerical investigations of nanodusty plasmas, Ph.D. thesis, 2006.

<sup>40</sup> A. Haji-Sheikh, B. Litkouhi, D. W. Pepper, H. Koenig, J. V. Beck, K. D. Cole, Series in Computational Methods and Physical Processes in Mechanics and Thermal Sciences, *CRC Press*,2021.

<sup>41</sup> E. Süli, An Introduction to Numerical Analysis, *Wiley*,2021.

<sup>42</sup> D. L. Scharfetter, and H. K. Gummel, Large-signal analysis of a silicon read diode oscillator, *IEEE Trans. Electron Devices*, 16(1): 64-77, 1969, <https://doi.org/10.1109/T-ED.1969.16566>.

<sup>43</sup> P. Roca i Cabarrocas, T. Nguyen-Tran, Y. Djeridane, A. Abramov, E. Johnson, and G. Patriarche, Synthesis of Silicon Nanocrystals in Silane Plasmas for Nanoelectronics and

Large Area Electronic Devices, *J. Phys. D: Appl. Phys.*, 40(8):2258–66,2007, <https://doi.org/10.1088/0022-3727/40/8/S04>.

<sup>44</sup> K.H. Kim, E. Johnson, A. G. Kazanskii, M. V. Khenkin, and P. Roca i Cabarrocas, Unravelling a Simple Method for the Low Temperature Synthesis of Silicon Nanocrystals and Monolithic Nanocrystalline Thin Films, *Sci. Rep.*, 7(1): 40553,2017, <https://doi.org/10.1038/srep40553>.

<sup>45</sup> J. M. Orlac'h, Modeling of a Silane-Hydrogen Plasma Discharge Including Nanoparticle Dynamics for Photovoltaic Applications, These de doctorat, Université Paris-Saclay, 2017.

<sup>46</sup> N. Chaâbane, V. Suendo, H. Vach, and P. Roca i Cabarrocas, Soft Landing of Silicon Nanocrystals in Plasma Enhanced Chemical Vapor Deposition, *Appl. Phys. Lett.*, 88(20) : 203111, 2006, <https://doi.org/10.1063/1.2204439>.

<sup>47</sup> P. Agarwal, Numerical Modeling of Plasmas in Which Nanoparticles Nucleate and Grow, Ph.D. thesis, 2012.



## Chapter 5 Conclusions and Perspectives

In this thesis, a fully consistent, 1D fluid model has been developed to study silane-hydrogen plasmas in a capacitively coupled radio frequency glow discharge. This model includes continuity equations for gas species, the second moment of the Boltzmann equation for the electron probability density function, and strained flow equations which determine the fluid velocity. Also, the Poisson equation used to account for the electric potential is incorporated. The drift-diffusion approximation is used for transport fluxes. A complete chemistry mechanism includes: i) electron collision reactions which depend on the electron temperature; ii) heavy-species reactions which depend on the heavy-species temperature; and iii) surface chemistry which includes recombination, etching, and deposition reactions. Under typical process conditions, the 1-D fluid model is performed to study the silane-hydrogen plasma properties. After about 40000 RF cycles a steady state solution is obtained. The computed deposition rates have been compared with the experimental ones for various values of total pressure and silane concentration. In particular,  $\text{SiH}_3$  radicals have been found to be the main precursors of thin film deposition and  $\text{H}_3^+$  ions are the main species contributing to the etching process. The net deposition rate shows a good agreement with the experimental values after taking into account the etching rate.

A sectional model for nanoparticles with respect to size and charge has been implemented in the 1D fluid model. The model contains a complete chemistry mechanism for nanoparticles' nucleation, the effect of charge enhancement on coagulation, and the transport of nanoparticles. Also, the effect of the nanoparticles on plasma species densities, electrical potential and electron temperature has been taken into account. Thus, the 1-D fluid-sectional model can be also used to study nanoparticles formation in the silane-hydrogen discharge. A time-splitting method is applied to make the model efficient. Separated time integrations are carried out for "fast" variables, namely the electric potential, the electron temperature and the charged

species densities, and “slow” variables, which describe the behavior of the nanoparticles. The results are validated by comparison with the model without applying the time-splitting method. Finally, we calculated that, under the studied process conditions, the contribution of nanoparticles to the deposition rate of silicon thin films is negligible compared with  $\text{SiH}_3$  radicals at the early stage of nanoparticles formation.

Several perspectives of research can be drawn. First, from a theoretical viewpoint, a plasma sheath model and ion energy distribution should be implemented into the 1-D fluid model to further study the ions behavior in the silane-hydrogen plasma. The results from this model should be validated against a kinetic model, for example, the particle-in-cell model. Second, the results from 1-D fluid model should be compared with experimental data. The electrical plasma potential, electron energy, gas species densities and ion fluxes should be compared to experimental data. Third, the effect of tailored voltage waveforms on ion fluxes and energies in the discharge will be studied experimentally and numerically. Fourth, the thermophoresis force could be implemented in the 1-D fluid-sectional model to study its effect on nanoparticles' transport properties, and its effect on the deposition of nanoparticles. Finally, the 1-D fluid-sectional model by using time-splitting method can be improved to be faster. The current model is not fast enough, though it can save a lot of time compared with the coupled model.

# ANNEX I. Electron collision reactions included in the fluid model

Reaction number	Electron collision	$A_r$ (mol, cm <sup>3</sup> , s)	$\beta_r$	$\mathcal{E}_r$ (cal.mol <sup>-1</sup> )	Ref.
<b>Ionization</b>					
RE1	$H_2 + e \Rightarrow H_2^+ + 2e$	$4.798 \times 10^{13}$	0.505	361,455	[1]
RE2	$H + e \Rightarrow H^+ + 2e$	$1.080 \times 10^{16}$	0	178,210	[2]
RE3	$H_2 + e \Rightarrow H^+ + H + 2e$	$3.745 \times 10^{10}$	0.810	418,729	[3]
RE4	$SiH_4 + e \Rightarrow SiH_3^+ + H + 2e$	$1.510 \times 10^{32}$	-2.930	553,910	[4]
RE5	$SiH_3 + e \Rightarrow SiH_3^+ + 2e$	$1.355 \times 10^{12}$	0.900	188,396	[4]
<b>Dissociation</b>					
RE6	$H_2 + e \Rightarrow 2H + e$	$1.020 \times 10^{16}$	0	238,347	[1]
RE7	$H_3^+ + e \Rightarrow H^+ + 2H + e$	$1.220 \times 10^{17}$	0	179,380	[5]
RE8	$H_2^+ + e \Rightarrow H^+ + H + e$	$1.460 \times 10^{17}$	0	37,460	[5]
RE9	$SiH_4 + e \Rightarrow SiH_3 + H + e$	$1.1 \times 10^{21}$	-1.000	245,421	[4]
RE10	$SiH_4 + e \Rightarrow SiH_2 + 2H + e$	$5.4 \times 10^{21}$	-1.000	245,421	[4]
<b>Dissociative attachment</b>					
RE11	$SiH_4 + e \Rightarrow SiH_3^- + H$	$2.269 \times 10^{21}$	-1.627	190,540	[4]
RE12	$SiH_4 + e \Rightarrow SiH_2^- + 2H$	$2.269 \times 10^{21}$	-1.627	190,540	[4]
RE13	$SiH_3 + e \Rightarrow SiH_2^- + H$	$3.440 \times 10^{15}$	-0.500	44,740	[4]
<b>Detachment</b>					
RE14	$SiH_3^- + e \Rightarrow SiH_3 + 2e$	$1.900 \times 10^{14}$	0.500	32,425	[4]
RE15	$SiH_2^- + e \Rightarrow SiH_2 + 2e$	$1.900 \times 10^{14}$	0.500	25,921	[4]
<b>Recombination and dissociative recombination</b>					
RE16	$H^+ + 2e \rightarrow H + e$	$3.630 \times 10^{37}$	-4.000	0	[5]
RE17	$H_3^+ + e \rightarrow 3H$	$8.000 \times 10^{17}$	-0.404	0	[5][6]
RE18	$H_3^+ + 2e \rightarrow H + H_2 + e$	$3.170 \times 10^{21}$	-4.500	0	[5]
RE19	$H_2^+ + 2e \rightarrow 2H + e$	$3.170 \times 10^{21}$	-4.500	0	[5]

## References

- <sup>1</sup> A. V. Phelps database, University of Colorado Boulder, [www.lxcat.net/Phelps](http://www.lxcat.net/Phelps).
- <sup>2</sup> Kim Y. K. and Rudd M. E., Binary-encounter-dipole model for electron-impact ionization, *Phys. Rev. A* **50** 3954, 1994, <https://doi.org/10.1103/PhysRevA.50.3954>.
- <sup>3</sup> Janev R. K., Langer W. D., Post D. E. and Evans K. ,Elementary Processes in Hydrogen-Helium Plasmas, *Springer, Berlin, Heidelberg*. pp. 17-114, 1987, <https://www.semanticscholar.org/paper/Elementary-processes-in-hydrogen-helium-plasmas-%3A-Janev-Langer/a78961f97db70903954488d1b13110b1db20aefc>.
- <sup>4</sup> Bhandarkar U. V., Swihart M. T., Girshick S. L. and Kortshagen U. R., Modelling of silicon hydride clustering in a low-pressure silane plasma, *J. Phys. D: Appl. Phys.* **33**:2731,2000, <https://doi.org/10.1088/0022-3727/33/21/311>.
- <sup>5</sup> Scott C. D., Farhat S., Gicquel A., Hassouni K. and Lefebvre M. J. Thermophys., Determining electron temperature and density in a hydrogen microwave plasma, *Heat Trans.* **10** 426,2012, <https://doi.org/10.2514/3.807>.
- <sup>6</sup> Kalache B., Novikova T., Fontcuberta i Morral A., Roca i Cabarrocas P., Morscheidt W. and Hassouni K., Investigation of coupling between chemistry and discharge dynamics in radio frequency hydrogen plasmas in the Torr regime, *J. Phys. D: Appl. Phys.* **37** 1765,2004, <https://doi.org/10.1088/0022-3727/37/13/007>.

## ANNEX II. Heavy species reactions included in the plasma model

Reaction number	Heavy species reactions	$A_r$ (mol, cm <sup>3</sup> , s)	$\beta_r$	$\mathcal{E}_r$ (cal.mol <sup>-1</sup> )	Ref.
<b>Neutral-neutral reactions</b>					
RH1	$H_2+H_2=2H+H_2$	$8.610 \times 10^{17}$	-0.700	52,530	[2]
	Reverse rate	$1.000 \times 10^{17}$	-0.600	0.0	[2]
RH2	$H_2+H=3H$	$2.700 \times 10^{16}$	-0.100	52,530	[2]
	Reverse rate	$3.200 \times 10^{15}$	0	0.0	[2]
RH3	$SiH_4+H=SiH_3+H_2$	$1.51 \times 10^{13}$	0	2,484	[1]
RH4	$Si_2H_6+H=Si_2H_5+H_2$	$1.3 \times 10^{12}$	0	0	[1]
RH5	$Si_2H_6+H=SiH_3+SiH_4$	$4.82 \times 10^{13}$	0	2,484	[1]
RH6	$SiH_2 + H_2 = SiH_4$	$5.260 \times 10^{10}$	0.000	0	[1]
RH7	$SiH_2 + SiH_4 = Si_2H_6$	$3.620 \times 10^{13}$	0.000	0	[1]
RH8	$SiH_3+SiH_3=SiH_2+SiH_4$	$9.03 \times 10^{13}$	0.000	0	[1]
<b>Neutralization reaction</b>					
RH9	$SiH_3+SiH_3^+=SiH_3+SiH_3$	$1.232 \times 10^{18}$	-0.500	0	[1]
RH10	$SiH_2+SiH_3^+=SiH_2+SiH_3$	$1.359 \times 10^{18}$	-0.500	0	[1]
RH11	$Si_2H_5+SiH_3^+=Si_2H_5+SiH_3$	$9.648 \times 10^{17}$	-0.500	0	[1]
RH12	$H_3SiSiH^++SiH_3^+=H_3SiSiH+SiH_3$	$1.001 \times 10^{18}$	-0.500	0	[1]
<b>Cluster growth</b>					
RH13	$SiH_3+SiH_4=Si_2H_5+H_2$	$6.020 \times 10^{11}$	0.000	0	[1]
RH14	$SiH_2+SiH_4=H_3SiSiH^++H_2$	$6.020 \times 10^{11}$	0.000	0	[1]
<b>Additional hydrogen reactions</b>					
RH15	$H_2^++H=H^++H_2$	$3.850 \times 10^{14}$	0.000	0	[2][3]
	Reverse rate	$1.900 \times 10^{14}$	0.000	21,902	[2]
RH16	$H_2+H_2^+\rightarrow H_3^++H$	$1.270 \times 10^{15}$	0.000	0	[2][3]
RH17	$H^++2H_2\rightarrow H_3^++H_2$	$1.950 \times 10^{20}$	-0.500	0	[2][3]

## References

- <sup>1</sup> Bhandarkar U. V., Swihart M. T., Girshick S. L. and Kortshagen U. R., Modelling of silicon hydride clustering in a low-pressure silane plasma, *J. Phys. D: Appl. Phys.* **33**:2731,2000, <https://doi.org/10.1088/0022-3727/33/21/311>.
- <sup>2</sup> Scott C. D., Farhat S., Gicquel A., Hassouni K. and Lefebvre M. J. Thermophys., Determining electron temperature and density in a hydrogen microwave plasma, *Heat Trans.* **10** 426,2012, <https://doi.org/10.2514/3.807>.
- <sup>3</sup> Kalache B., Novikova T., Fontcuberta i Morral A., Roca i Cabarrocas P., Morscheidt W. and Hassouni K., Investigation of coupling between chemistry and discharge dynamics in radio frequency hydrogen plasmas in the Torr regime, *J. Phys. D: Appl. Phys.* **37** 1765,2004, <https://doi.org/10.1088/0022-3727/37/13/007>.

## ANNEX III. Net average electron energy loss in reactive collisions

Reaction number	Electron collision	$-\Delta\mathcal{E}_{er}$ (eV)	Ref.
RE1	$\text{H}_2 + e \Rightarrow \text{H}_2^+ + 2e$	15.43	[1]
RE2	$\text{H} + e \Rightarrow \text{H}^+ + 2e$	13.6	[2]
RE3	$\text{H}_2 + e \Rightarrow \text{H}^+ + \text{H} + 2e$	18	[3]
RE4	$\text{SiH}_4 + e \Rightarrow \text{SiH}_3^+ + \text{H} + 2e$	12.09	[4]
RE5	$\text{SiH}_3 + e \Rightarrow \text{SiH}_3^+ + 2e$	8.01	[4]
RE6	$\text{H}_2 + e \Rightarrow 2\text{H} + e$	10.5	[1]
RE7	$\text{H}_3^+ + e \Rightarrow \text{H}^+ + 2\text{H} + e$	14.87	[5]
RE8	$\text{H}_2^+ + e \Rightarrow \text{H}^+ + \text{H} + e$	8.67	[5]
RE9	$\text{SiH}_4 + e \Rightarrow \text{SiH}_3 + \text{H} + e$	8.00	[4]
RE10	$\text{SiH}_4 + e \Rightarrow \text{SiH}_2 + 2\text{H} + e$	8.00	[4]
RE11	$\text{SiH}_4 + e \Rightarrow \text{SiH}_3^- + \text{H}$	5.70	[4]
RE12	$\text{SiH}_4 + e \Rightarrow \text{SiH}_2^- + 2\text{H}$	5.10	[4]
RE13	$\text{SiH}_3 + e \Rightarrow \text{SiH}_2^- + \text{H}$	5.5	[4]
RE14	$\text{SiH}_3^- + e \Rightarrow \text{SiH}_3 + 2e$	1.41	[4]
RE15	$\text{SiH}_2^- + e \Rightarrow \text{SiH}_2 + 2e$	1.12	[4]
RE16	$\text{H}^+ + 2e \rightarrow \text{H} + e$	-13.6	[5]
RE17	$\text{H}_3^+ + e \rightarrow 3\text{H}$	1.27	[5][6]
RE18	$\text{H}_3^+ + 2e \rightarrow \text{H} + \text{H}_2 + e$	-9.23	[5]
RE19	$\text{H}_2^+ + 2e \rightarrow 2\text{H} + e$	-4.93	[5]

## References

- <sup>1</sup> A. V. Phelps database, University of Colorado Boulder, [www.lxcat.net/Phelps](http://www.lxcat.net/Phelps).
- <sup>2</sup> Kim Y. K. and Rudd M. E., Binary-encounter-dipole model for electron-impact ionization, *Phys. Rev. A* **50** 3954, 1994, <https://doi.org/10.1103/PhysRevA.50.3954>.
- <sup>3</sup> Janev R. K., Langer W. D., Post D. E. and Evans K. ,Elementary Processes in Hydrogen-Helium Plasmas, *Springer, Berlin, Heidelberg*. pp. 17-114, 1987, <https://www.semanticscholar.org/paper/Elementary-processes-in-hydrogen-helium-plasmas-%3A-Janev-Langer/a78961f97db70903954488d1b13110b1db20aefc>.
- <sup>4</sup> Bhandarkar U. V., Swihart M. T., Girshick S. L. and Kortshagen U. R., Modelling of silicon hydride clustering in a low-pressure silane plasma, *J. Phys. D: Appl. Phys.* **33**:2731,2000, <https://doi.org/10.1088/0022-3727/33/21/311>.
- <sup>5</sup> Scott C. D., Farhat S., Gicquel A., Hassouni K. and Lefebvre M. J. Thermophys., Determining electron temperature and density in a hydrogen microwave plasma, *Heat Trans.* **10** 426,2012, <https://doi.org/10.2514/3.807>.
- <sup>6</sup> Kalache B., Novikova T., Fontcuberta i Morral A., Roca i Cabarrocas P., Morscheidt W. and Hassouni K., Investigation of coupling between chemistry and discharge dynamics in radio frequency hydrogen plasmas in the Torr regime, *J. Phys. D: Appl. Phys.* **37** 1765,2004, <https://doi.org/10.1088/0022-3727/37/13/007>.

# ANNEX IV. List of surface reactions.

Notation (g) means gas species; notation (s) means surface species; notation wall means substrate.  $\rho$ ,  $\varepsilon$ , and  $\sigma$  represent the probability of recombination, etching and sticking. For hydrogen and its ions, as these species have negligible influence on the silicon deposition rate, their sticking coefficients are taken equal to 0.0.

Reaction number	surface reactions	$p_r$ (-)	Ref.
RS1	$H + \text{wall} = 0.5H_2(g)$	$\rho_H = 0.7$	[1][2][3]
RS2	$4H + \text{Si-wall} = SiH_4(g)$	$\varepsilon_H = 3.045 \cdot 10^{-4} \exp(1357/T_s)$ ( $T_s$ is the substrate temperature)	[1] [4]
RS3	$4H^+ + \text{Si-wall} = SiH_4(g)$	$\varepsilon_{H^+} = 1.0$	[4]
RS4	$2H_2^+ + \text{Si-wall} = SiH_4(g)$	$\varepsilon_{H_2^+} = 1.0$	[4]
RS5	$4H_3^+ + 3\text{Si-wall} = 3SiH_4(g)$	$\varepsilon_{H_3^+} = 1.0$	[4]
RS6	$SiH_2(g) + \text{wall} = Si(s) + H_2(g)$	$\sigma_{SiH_2} = 0.8$	[1][2][3]
RS7	$SiH_3(g) + \text{wall} = Si(s) + H_2(g) + H(g)$	$\sigma_{SiH_3} = 0.1$	[1][2][3]
RS8	$SiH_3(g) + SiH_3\text{-wall} = Si_2H_6(g)$	$\rho_{SiH_3 \rightarrow Si_2H_6} = 0.0$	[1][2][3]
RS9	$SiH_3(g) + H\text{-wall} = SiH_4(g)$	$\rho_{SiH_3} = 0.16$	[1][2][3]
RS10	$SiH_4(g) + \text{wall} = Si(s) + 2H_2(g)$	$\sigma_{SiH_4} = 5.37 \cdot 10^{-2} \exp(-9400/(T_s))$	[5]
RS11	$H_3SiSiH(g) + \text{wall} = 2Si(s) + 2H_2(g)$	$\sigma_{Si_2H_4} = 0.8$	[1][2][3]
RS12	$Si_2H_5(g) + \text{wall} = 2Si(s) + 2H_2(g) + H(g)$	$\sigma_{Si_2H_5} = 0.1$	[1][2][3]
RS13	$Si_2H_5(g) + H\text{-wall} = Si_2H_6(g)$	$\rho_{Si_2H_5} = 0.16$	[1][2][3]
RS14	$Si_2H_6(g) + \text{wall} = 2Si(s) + 3H_2(g)$	$\sigma_{Si_2H_6} = 5.37 \cdot 10^{-1} \exp(-9400/(T_s))$	[6]
RS15	$SiH_3^+ + \text{wall} = Si(s) + H_2(g) + H(g)$	$\sigma_{SiH_3^+} = 1.0$	[1]
RS16	$SiH_2^+ + \text{wall} = Si(s) + H_2(g)$	$\sigma_{SiH_2^+} = 1.0$	[1]
RS17	$Si_2H_4^+ + \text{wall} = 2Si(s) + 2H_2(g)$	$\sigma_{Si_2H_4^+} = 1.0$	[1]

## References

- <sup>1</sup> E. Amanatides, D. Mataras, and D. E. Rapakoulias, Effect of Frequency in the Deposition of Microcrystalline Silicon from Silane Discharges, *J. Appl. Phys.*,90(11): 5799–5807,2001, <https://doi.org/10.1063/1.1413240>.
- <sup>2</sup> E. Amanatides, D. E. Rapakoulias, and D. Mataras, Electron-Impact Silane Dissociation and Deposition Rate Relationship in the PECVD of Microcrystalline Silicon Thin Films, *Le Journal de Physique IV*, 11(PR3):722,2001, <https://doi.org/10.1051/jp4:2001390>.
- <sup>3</sup> E. Amanatides, S. Stamou, and D. Mataras, Gas Phase and Surface Kinetics in Plasma Enhanced Chemical Vapor Deposition of Microcrystalline Silicon: The Combined Effect of Rf Power and Hydrogen Dilution, *J. Appl. Phys.*, 90(11): 5786–98,2001, <https://doi.org/10.1063/1.1413241>.
- <sup>4</sup> Leroy O., Gousset G., Alves L. L., Perrin J. and Jolly J., Two-dimensional modelling of radio-frequency discharges for a-Si: H deposition, *Plasma Sources Sci. Technol.* 7:348,1998, <https://doi.org/10.1088/0963-0252/7/3/013>.
- <sup>5</sup> Coltrin M. E., Kee R. J. and Miller J. A.,A Mathematical Model of Silicon Chemical Vapor Deposition: Further Refinements and the Effects of Thermal Diffusion *J. Electrochem. Soc.* 133:1206,1986, <https://doi.org/10.1149/1.2108820>.
- <sup>6</sup> Coltrin M., Kee R., Evans G. and Miller G., *Proceedings of the tenth international conference on chemical vapor deposition*, 1987, [https://inis.iaea.org/search/search.aspx?orig\\_q=RN:19105888](https://inis.iaea.org/search/search.aspx?orig_q=RN:19105888).

# ANNEX V:

## The effect of tailored voltage waveforms on silane-hydrogen plasmas

### Contents

#### ANNEX V: The effect of tailored voltage waveforms on silane-hydrogen plasmas

<b>Introduction.....</b>	<b>122</b>
<b>Simulation method.....</b>	<b>122</b>
<b>Results and Discussions.....</b>	<b>124</b>
<i>The effect of Valleys waveforms on silane/hydrogen plasmas .....</i>	<i>124</i>
<i>The effect of Sawtooth-like waveforms on silane/hydrogen plasmas .....</i>	<i>126</i>
<b>Conclusions and Perspectives .....</b>	<b>129</b>
<b>References .....</b>	<b>130</b>

## Introduction

In 2008, B. G. Heil discovered that the energies of ions arriving at each of the two electrodes in a geometrically symmetric radiofrequency (RF) capacitively-coupled plasma (CCP) reactor can be independently controlled by using non-sinusoidal waveforms, this is so-called electrical asymmetry effect (EAE)<sup>1</sup>. Initially, the waveform was composed of only two frequencies, a base frequency and its harmonic. The independent control of ion energies was achieved by varying the phase difference between these two frequency components<sup>1</sup>. Then, the waveforms containing multiple frequencies (tailored voltage waveforms) have been an intense research subject<sup>2,3</sup>. Research on tailored voltage waveforms (TVWs) has mainly concentrated on the amplitude-asymmetry effect in the waveforms<sup>4</sup> (i.e. different amplitude maxima and minima) and slope-asymmetry effect (i.e. different rise and fall times)<sup>2,3</sup>. The amplitude-asymmetry effect and the slope-asymmetry effect were investigated by particle-in-cell model for Ar, H<sub>2</sub>, and CF<sub>4</sub> gases, which is explained by the different dominant electron heating mechanisms and plasma chemistries<sup>5</sup>. However, the effect of electrical asymmetry effect (EAE) on SiH<sub>4</sub>-H<sub>2</sub> plasmas using tailored voltage waveforms in fluid model has received little attention. In this chapter, we plan to use 1-D fluid model to study the EAE on silane/hydrogen plasmas and aim to independently control the ions fluxes and ions energies arriving at the electrodes by using TVWs so as to optimize silicon thin film properties.

## Simulation method

The 1-D fluid model mentioned in the Chapter 2 will be used to study the effect of TVWs on silane/hydrogen plasmas. The TVWs in this study includes Sawtooth-like waveforms, Peaks and Valleys waveforms. The following waveforms can be sawtooth-like waveforms by adding the number of harmonics, which is written as follows:

---

<sup>1</sup> B. G. Heil et al., *J. Phys. D: Appl. Phys.*, 41(16): 165202, 2008.

<sup>2</sup> B. Bruneau et al., *Plasma Sources Sci. Technol.*, 23(6): 065010, 2014.

<sup>3</sup> B. Bruneau et al., *Plasma Sources Sci. Technol.*, 24(1): 015021, 2014.

<sup>4</sup> B. Bruneau et al., *J. Appl. Phys.*, 119(16): 163301, 2016.

<sup>5</sup> B. Bruneau et al., *Plasma Sources Sci. Technol.*, 25(1): 01LT02, 2015.

$$\varphi_{AP}(t) = \varphi_{RF} \sum_{k=1}^N \frac{1}{k} \sin(k\omega t) \quad (1)$$

Where  $\varphi_{AP}$  is the applied potential on the driven electrode,  $N$  denotes the number of harmonics,  $\omega = 2\pi f$ , where  $f = 13.56 \text{ MHz}$  is the base RF frequency.  $\varphi_{RF}$  is an amplitude perfector. Therefore, the amplitude at each frequency is written as:

$$\varphi_k = \frac{\varphi_{RF}}{k} \quad (2)$$

Figure 1 shows the sawtooth-like waveforms with the different number of harmonics.

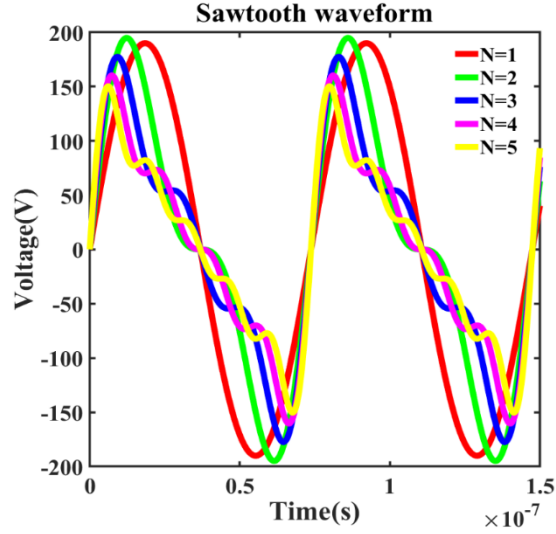


Fig.1 The Sawtooth-like waveforms for the number of harmonics  $N = 1$  to  $N = 5$ . In particular, for  $N = 1$ , the waveform is sine waveform.

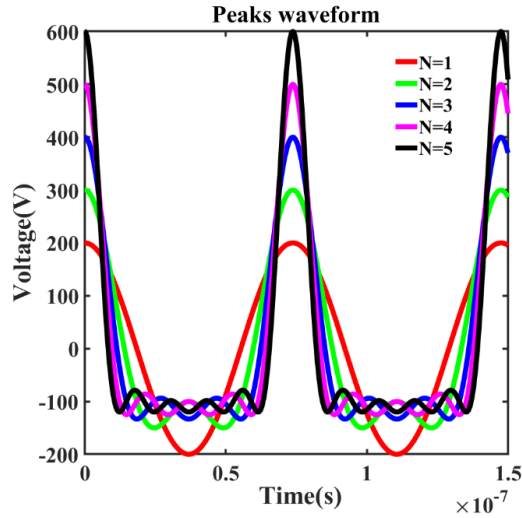


Fig.2 The Valleys waveforms for the number of harmonics  $N = 1$  to  $N = 5$ . In particular, for  $N=1$ , the waveform is sine waveform.  $\varphi_{RF} = 200\text{V}$ ,  $\theta=0$ .

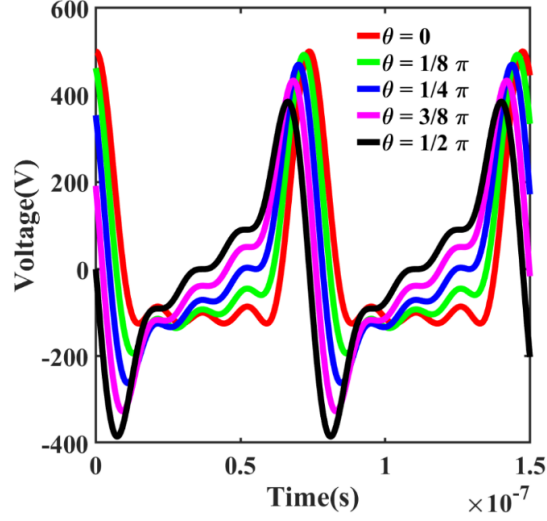


Fig.3 The sawtooth-up waveforms for the number of harmonics  $N = 4$ . In particular, for  $\theta = 0$ , the waveform is Peak waveform.

The valleys waveforms can be achieved by adding the number of harmonics in the following waveform formula:

$$\varphi_{AP}(t) = \varphi_{RF} \sum_{k=1}^N \frac{(N-k+1)}{N} \cos(k\omega t + \theta) \quad (3)$$

where  $\theta$  is the phase shift. Figure 2 shows the valleys waveforms with different number of harmonics. In particular, for  $N = 1$ , sine waveform is achieved. Here,  $\varphi_{RF} = 200\text{V}$ ,  $\theta = 0$  is applied. The sawtooth-like waveforms also can be achieved by adjusting the phase shift  $\theta$  in (3). Figure 3 shows the sawtooth-up waveforms by adjusting the phase shift  $\theta$  from 0 to  $\frac{\pi}{2}$  at  $N = 4$ . In particular, the peak waveforms is achieved when  $\theta = 0$ . The waveforms introduced above will be used to study silane/hydrogen plasmas.

## Results and Discussions

### *The effect of Valleys waveforms on silane/hydrogen plasmas*

In the following, we address the effect of valleys waveforms on the silane/hydrogen plasma properties, including electrical potential, ionization rate, ions fluxes and DC self-bias. The process conditions are defined as follows: the gas temperature is fixed at 448K, the pressure is 1.5 Torr,  $\varphi_{RF} = 200\text{V}$ , RF frequency  $f = 13.56\text{ MHz}$ , the inter-electrode

distance is equal to 1.6 cm, and the silane concentration ( $\text{SiH}_4/(\text{SiH}_4+\text{H}_2)$ ) is 1.4%. The grounded and powered electrodes are symmetric, so there is no DC self-bias when a sine waveform is applied. The Valleys waveforms in Figure 2 with different number of harmonics are applied to study its effect on silane/hydrogen plasmas. The  $V_{pp}$  is defined as peak-to-peak voltage,  $V_{pp} = \varphi_{max} - \varphi_{min}$ , where  $\varphi_{max}$  is the maximum value of the applied voltage, and  $\varphi_{min}$  is the minimum value of applied voltage. At constant  $\varphi_{RF}$ , we can deduce that the degree of amplitude asymmetry in the Valleys waveforms can be described as  $\frac{\varphi_{max}}{\varphi_{min}} = N$ , which means that the degree of amplitude asymmetry increases as  $N$  increases. Figure 4(a) shows that the  $V_{pp}$  (Peak-to-Peak voltage) as a function of number of harmonics. We can see that the  $V_{pp}$  increases as  $N$  increases. Figure 4(b) shows that the normalized DC self-bias increases as  $N$  increases. The inset figure shows that the values of DC self-bias increase with  $N$  and does not reach saturation even for  $N=5$ .

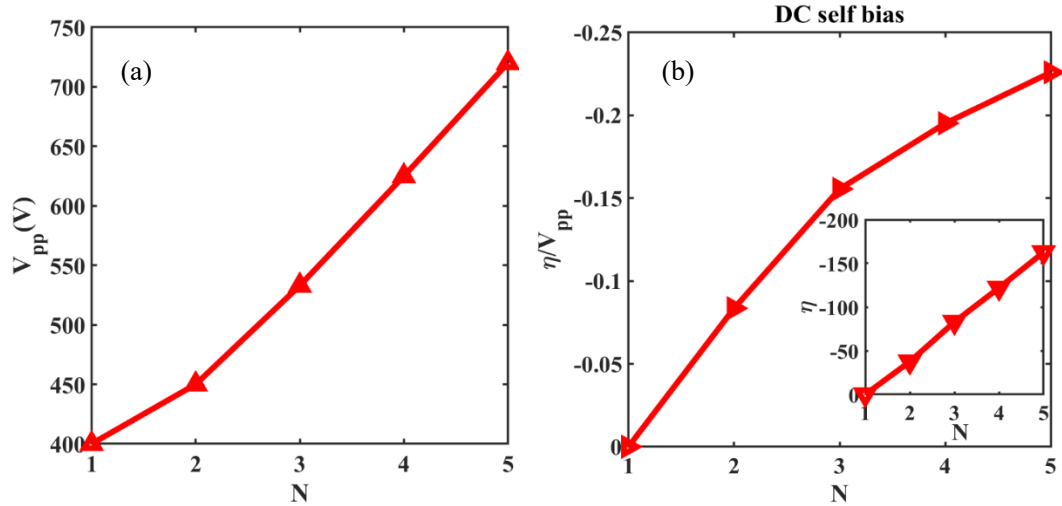


Fig.4 (a) The  $V_{pp}$  (peak-to-peak voltage) as a function of number of harmonics. The waveform applied is  $\varphi_{AP}(t) = \varphi_{RF} \sum_{k=1}^N \frac{(N-k+1)}{N} \cos(k\omega t + \theta)$ ,  $\varphi_{RF} = 200\text{V}$ ,  $\theta = 0$  and  $N$  varies from 1 to 5. (b) The normalized DC-self bias as a function of number of harmonics. The inset shows the values of DC self-bias with increasing the number of harmonics.

As Figure 5 shows, the flux ratio ( $\Gamma_{ip}/\Gamma_{ig}$ , where  $\Gamma_{ip}$  indicates the ions fluxes towards the powered electrode, and  $\Gamma_{ig}$  indicates the ions fluxes towards the grounded electrode) increases and goes to saturation as  $N$  increases. The normalized DC self bias ( $\eta/V_{pp}$ )

decreases and does not reach saturation as N increases.

The key point is that we can obtain the desired flux with lowest N, and at the same time the DC self-bias is controlled to minimum which means ion bombard energy can be controlled. In other words, TVWs allows to decouple ion flux from ion energy. For example, at N=4, if we have desired flux ratio, we donnot need to increase N to 5 which result in increased DC self-bias.

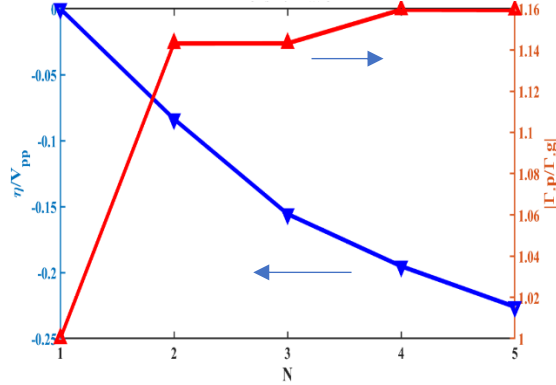


Fig.5 The normalized DC self-bias (blue line) and ion fluxes ratio (red line) as functions of the number of harmonics.

### ***The effect of Sawtooth-like waveforms on silane/hydrogen plasmas***

In the following, we address the effect of Sawtooth waveforms (Figure 1,  $\varphi_{AP}(t) = \varphi_{RF} \sum_{k=1}^N \frac{1}{k} \sin(kt)$ ) on the silane/hydrogen plasma properties, including electrical potential, ionization rate, ions fluxes and DC self-bias. The process conditions are defined as follows: the gas temperature is fixed at 448K, the pressure is 1.5 Torr, RF frequency  $f = 13.56 \text{ MHz}$ , the power is constant at 12 W for all number of harmonics, the inter-electrode distance is equal to 1.6 cm, and the silane concentration ( $\text{SiH}_4/(\text{SiH}_4+\text{H}_2)$ ) is 1.4%. The grounded and powered electrodes are symmetric, so there is no DC self-bias under condition of sine waveforms. In Figure 6, we can see that the normalized DC self-bias ( $\eta/V_{pp}$ ) increases to saturation as the number of harmonics increases. The inset shows the values of DC self-bias ( $\eta$ ) as a function of number of harmonics. We can see the DC self-bias dramatically increases to 30 V when N is equal to 2, then it goes to saturation, this is probably due to the constant power applied.

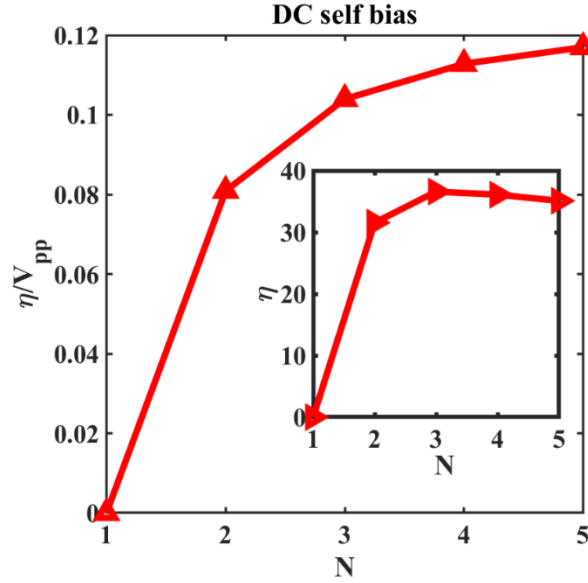


Fig.6 The normalized DC-self bias as a function of number of harmonics. The inset figure shows the values of DC self-bias with increasing the number of harmonics, the units is in V. The waveforms applied is  $\varphi_{AP}(t) = \varphi_{RF} \sum_{k=1}^N \frac{1}{k} \sin(kt)$ , the power is set at 12 W for all N, and N varies from 1 to 5.

As the Figure 7 (a) shows, the flux ratio ( $\Gamma_{ip}/\Gamma_{ig}$ , where  $\Gamma_{ip}$  indicates the ions fluxes towards the powered electrode, and  $\Gamma_{ig}$  indicates the ions fluxes towards the grounded electrode) increases and goes to saturation as N increases, which shows the asymmetric effect for the ion fluxes at grounded and powered electrode. The normalized DC self-bias ( $\eta/V_{pp}$ ) increases and goes to saturation as N increases. For Figure 7 (b), the  $H_3^+$  ion fluxes at both electrodes shows same trend, while  $H_3^+$  ion fluxes are higher at powered electrode than that at grounded electrode, which shows the asymmetry at the both electrodes.

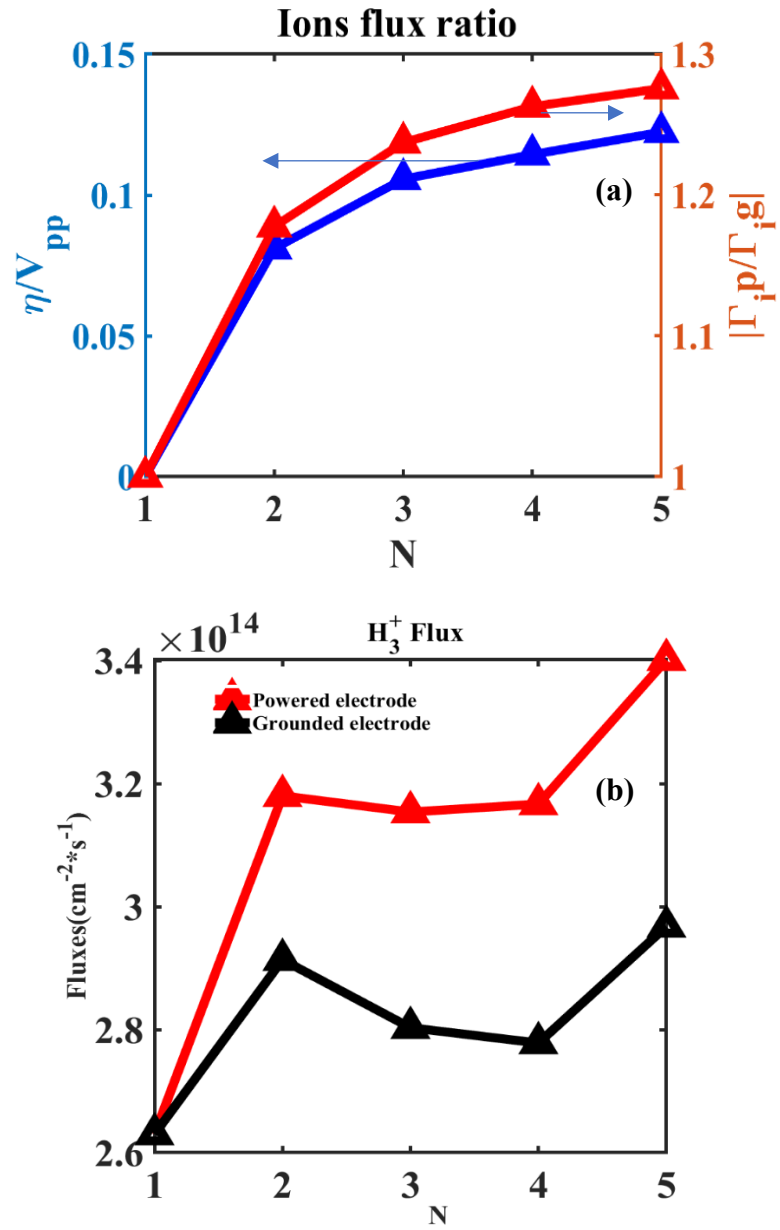


Fig.7 (a) The normalized DC self-bias (blue line) and ion fluxes ratio (red line) as a function of number of harmonics. (b) H<sub>3</sub><sup>+</sup> ions fluxes towards the powered electrode (red line) and grounded electrode (black line) as a function of number of harmonics.

## Conclusions and Perspectives

We have applied the fluid model in Chapter 2 to study the electrical asymmetry effect in silane/hydrogen plasmas when applying the tailored voltage waveforms (TVWs). The sawtooth-like waveforms ( $\varphi_{AP}(t) = \varphi_{RF} \sum_{k=1}^N \frac{1}{k} \sin(k\omega t)$ ) and valleys waveforms ( $\varphi_{AP}(t) = \varphi_{RF} \sum_{k=1}^N \frac{(N-k+1)}{N} \cos(k\omega t + \theta)$ ) are used to study the slope asymmetry and amplitude asymmetry effects. For the valley waveforms, the values of DC self-bias are negative when harmonics are added to the waveform. Also, the DC self-bias increases when the number of harmonics increases. In addition, the ion fluxes at powered electrode are larger than that at grounded electrode when increasing the number of harmonics, and the fluxes ratio ( $\Gamma_{ip}/\Gamma_{ig}$ ) increases to saturation when the number of harmonics is equal to 4. For the sawtooth-like waveforms, DC self-bias dramatically increases to 30 V when N is equal to 2, then it goes to saturation, this is probably due to the constant power applied. Also, the flux ratio increases and goes to saturation as N increases. In addition,  $H_3^+$  ion fluxes are much higher at powered electrode than that at grounded electrode after adding harmonics, which plays a main role in etching process during the deposition of silicon thin films.

For the perspectives, the modelling results should be compared to experiments in the future.

## References

- <sup>1</sup> B. G. Heil, U. Czarnetzki, R. P. Brinkmann and T. Mussenbrock, On the Possibility of Making a Geometrically Symmetric RF-CCP Discharge Electrically Asymmetric, *J. Phys. D: Appl. Phys.*, 41(16): 165202,2008, <https://doi.org/10.1088/0022-3727/41/16/165202>.
- <sup>2</sup> B. Bruneau, T. Novikova, T. Lafleur, J. P. Booth and E. V. Johnson, Ion Flux Asymmetry in Radiofrequency Capacitively-Coupled Plasmas Excited by Sawtooth-like Waveforms, *Plasma Sources Sci. Technol.*, 23(6):065010,2014,<https://doi.org/10.1088/0963-0252/23/6/065010>.
- <sup>3</sup> B. Bruneau, T. Novikova, T. Lafleur, J. P. Booth and E. V. Johnson, Control and Optimization of the Slope Asymmetry Effect in Tailored Voltage Waveforms for Capacitively Coupled Plasmas, *Plasma Sources Sci. Technol.*, 24(1):015021,2014 ,<https://doi.org/10.1088/0963-0252/24/1/015021>.
- <sup>4</sup> B. Bruneau, I. Korolov, T. Lafleur, T. Gans, D. O'Connell, A. Greb, A. Derzsi, Z. Donko, S. Brandt, E. Schungel, J. Schulze, E. Johnson, and J. P. Booth, Slope and Amplitude Asymmetry Effects on Low Frequency Capacitively Coupled Carbon Tetrafluoride Plasmas, *J. Appl. Phys.*, 119(16) : 163301,2016, <https://doi.org/10.1063/1.4947453>.
- <sup>5</sup> B. Bruneau, T. Lafleur, T. Gans, D. O'Connell, A. Greb, I. Korolov, A. Derzsi, Z. Donkó, S. Brandt, E Schüngel, J. Schulze, P. Diomedede, D. J. Economou, S. Longo, E. Johnson and J. P. Boothet, Effect of Gas Properties on the Dynamics of the Electrical Slope Asymmetry Effect in Capacitive Plasmas: Comparison of Ar, H<sub>2</sub> and CF<sub>4</sub>, *Plasma Sources Sci. Technol.*, 25(1): 01LT02, 2015, <https://doi.org/10.1088/0963-0252/25/1/01LT02>.



**Titre :** Études numériques et expérimentales de plasmas de Silane et Hydrogène utilisés pour la croissance épitaxiale de silicium

**Mots clés :** Modèle fluide 1D, décharges silane-hydrogène, modèle sectionnel, nanoparticules, vitesse de dépôt, vitesse de gravure, méthode de découpage temporel

**Résumé :** Sur la base du modèle fluide existant dans notre groupe, un modèle fluide 1D a été développé pour étudier les plasmas silane/hydrogène couplés capacitivement par radiofréquence (RF) et prendre en compte les processus de dépôt de couches minces de silicium. En particulier, la chimie de surface, y compris les réactions de recombinaison, de gravure et de dépôt, est couplée au modèle fluide via un ensemble de probabilités de réaction. Le modèle fluide 1-D a également été couplé à un modèle sectionnel et à des équations de transport pour tenir compte de la formation de nanoparticules dans le plasma et de l'évolution des distributions de taille et de charge des nanoparticules. Pour rendre le modèle fluide-sectionnel couplé 1-D efficace du point de vue informatique, une méthode de fractionnement du temps a été utilisée. Des études numériques et expérimentales des effets de la pression du gaz (1 à 3,5 Torr) et de

la concentration de silane (2 à 10 %) sur la vitesse de dépôt de films minces de silicium dans un réacteur standard de dépôt chimique en phase vapeur assisté par plasma (PECVD) ont démontré que le taux de dépôt tel que déterminé à partir de la modélisation optique des mesures ellipsométriques spectroscopiques UV-visible concorde bien avec les résultats de la modélisation. Les radicaux  $\text{SiH}_3$  s'avèrent être le principal contributeur aux taux de dépôt calculés, tandis que les ions  $\text{H}_3^+$  jouent le rôle principal dans le processus de gravure.

Le modèle fluide 1-D développé peut être utilisé pour les études des propriétés complexes des plasmas silane/hydrogène dans différentes conditions de procédé, et permet de prédire le comportement des espèces plasmatisées et des nanoparticules et des nanoparticules, ce qui n'est pas accessible avec les techniques de mesure directes in situ.

**Title :** Numerical and Experimental Studies of Pristine and Cluster containing Silane-Hydrogen Capacitively Coupled Plasmas Used for Silicon Epitaxial Growth

**Keywords :** 1D fluid model, silane-hydrogen discharges, sectional model, nanoparticles, deposition rate, etching rate, time-splitting method

**Abstract :** Based on an existing fluid model developed in our group, the code has been further developed to study radio-frequency (RF) capacitively-coupled silane/hydrogen plasmas and account for silicon thin film deposition processes. In particular, the surface chemistry including recombination, etching, and deposition reactions have been coupled to the fluid model via a set of reaction probabilities. The 1-D fluid model was also coupled with a sectional model and transport equations to account for the formation of nanoparticles within the plasma and the evolution of both size and charge distributions of the nanoparticles. To make the coupled 1-D fluid-sectional model computationally efficient, a time-splitting method was implemented.

Both numerical and experimental studies of the

effects of gas pressure (1 to 3.5 Torr) and silane concentration (2 to 10%) on the deposition rate of silicon thin films in a standard plasma enhanced chemical vapor deposition (PECVD) reactor demonstrated that the deposition rate as determined from the optical modelling of UV-visible spectroscopic ellipsometry measurements agrees well with the modeling results.  $\text{SiH}_3$  radicals are found to be the main contributor to the computed deposition rates, whereas  $\text{H}_3^+$  ions play the main role in the etching process.

The developed 1-D fluid model can be used for the studies of complex silane/hydrogen plasma properties under different process conditions, thus allowing to predict the behavior of plasma species and nanoparticles, which is not accessible with in-situ measurement techniques.